UNIVERSIDADE FEDERAL DE MINAS GERAIS
Instituto de Ciências Exatas
Programa de Pós-graduação em Física

Pedro Gonçalves de Oliveira

TOPOLOGICAL ASPECTS AND TRANSVERSE TRANSPORT IN MAGNONIC AND ELECTRONIC TWO-DIMENSIONAL LATTICES

Belo Horizonte
2025

Pedro Gonçalves de Oliveira

TOPOLOGICAL ASPECTS AND TRANSVERSE TRANSPORT IN MAGNONIC AND ELECTRONIC TWO-DIMENSIONAL LATTICES

Doctoral thesis presented to the Graduate Program in Physics at the Universidade Federal de Minas Gerais as a partial requirement for the degree of Doctor in Physics.

Supervisor: Antônio Sérgio Teixeira Pires

Belo Horizonte

2025

UNIVERSIDADE FEDERAL DE MINAS GERAIS

INSTITUTO DE CIÊNCIAS EXATAS

PROGRAMA DE PÓS-GRADUAÇÃO EM FÍSICA

FOLHA DE APROVAÇÃO

A presente tese, intitulada **"Topological aspects and transverse transport in magnonic and electronic two-dimensional lattices",** de autoria de **PEDRO GONÇALVES DE OLIVEIRA** submetida à Comissão Examinadora, abaixo-assinada, foi aprovada para obtenção do grau de **DOUTOR EM CIÊNCIAS, área de concentração Física,** em 26 de fevereiro de 2025.

Belo Horizonte, 26 de fevereiro de 2025.

Prof. Antônio Sérgio Teixeira Pires
Orientador do estudante
Departamento de Física /UFMG

Prof. Lucas Alvares da Silva Mól
Departamento de Física /UFMG

Prof. Emmanuel Araújo Pereira
Departamento de Física /UFMG

Prof. Ricardo Wagner Nunes
Departamento de Física /UFMG

Prof. Afrânio Rodrigues Pereira
Departamento de Física/UFV

Profa. Mariana Malard Sales Andrade
Instituto de Física/UNB

Acknowledgements

Resumo

Nas últimas décadas, a topologia desempenhou um papel crucial na física da matéria condensada, especialmente com a descoberta dos isolantes topológicos. Um isolante topológico é um sistema eletrônico cujo interior é isolante, mas estados condutores robustos estão localizados nas bordas ou superfícies. Esses sistemas são caracterizados por um índice topológico, como o número de Chern em isolantes topológicos de Chern.

O conceito de isolantes topológicos estende-se para bósons e, particularmente, para *magnons*. Embora sistemas bosônicos não sejam verdadeiros isolantes, um isolante topológico magnônico é definido como um sistema magnônico com um *gap* de energia e um índice topológico não-trivial. Eles apresentam transporte transversal (efeitos tipo-*Hall*), e, para bósons, isto pode ocorrer mesmo quando o índice topológico é zero (fase trivial).

Esta tese investiga diversas redes bidimensionais, com foco em sua classificação topológica e propriedades de transporte transversal. A ênfase está em redes magnônicas com diferentes ordenamentos de *spin*. Três geometrias são exploradas: a rede Lieb modificada, a rede Union Jack e a rede *brickwall*. Além disso, é estudado um modelo eletrônico *tight-binding* na rede *checkerboard* com Hamiltoniano não-Hermitiano, que pode descrever sistemas abertos, que trocam partículas e energia com o ambiente.

Os principais resultados incluem a descoberta de uma fase topológica na rede Lieb modificada ferromagnética, relacionada a uma anisotropia nas interações *exchange*. Nos sistemas antiferromagnéticos (redes Union Jack e *brickwall*), a curvatura de Berry e o transporte transversal foram analisados, elucidando os papéis da interação DMI e da geometria da rede. Na rede ferrimagnética Cu_2F_5, uma inversão na direção do transporte transversal em função da temperatura sugere potenciais aplicações em spintrônica de *magnons*. Por fim, o estudo da rede não-Hermitiana *checkerboard* revelou uma condutividade Hall não quantizada e pontos excepcionais, características únicas desse tipo de Hamiltoniano.

Unificados por sua dispersão com duas bandas de energia e formalismo matemático comum, esses sistemas fornecem *insights* sobre o papel da curvatura de Berry, topologia e transporte transversal em redes cristalinas. Os resultados sugerem aplicações em spintrônica de *magnons* e aprofundam o entendimento do transporte eletrônico em sistemas não-Hermitianos.

Palavras-chave: Efeito Hall, Magnons, Não-Hermitiano, Topologia.

Abstract

Over the past decades, topology has played a crucial role in condensed matter physics, particularly with the discovery of topological insulators. In the study of crystal lattices, a topological insulator is an electronic system where the bulk behaves as an insulator, while robust conducting states are localized at the edges or surfaces. These systems are characterized by a robust integer index, such as the Chern number in Chern topological insulators.

The concept of topological insulators extends to bosonic systems, particularly magnonic lattices. Although bosonic systems are not true insulators, a topological magnon insulator can be defined as a gapped magnonic system with a non-trivial topological index. These systems present transverse transport (Hall-like effects), and for bosons it can occur even when the topological index is zero (trivial phase).

This thesis investigates various two-dimensional lattices, focusing on their topological classification and transverse transport properties. The emphasis is on magnonic lattices with different spin orderings. Three geometries are explored: the modified Lieb lattice, Union Jack lattice, and brickwall lattice. Additionally, an electronic tight-binding model in the checkerboard lattice with a non-Hermitian Hamiltonian is studied, which can describe open systems that exchange particles and energy with its environment.

Key findings include the discovery of a topological Chern phase in the ferromagnetic modified Lieb lattice, related to an anisotropy in exchange interactions. For antiferromagnetic systems (Union Jack and brickwall lattices), Berry curvature and transverse transport were analyzed, elucidating the roles of DMI and lattice geometry. In the ferrimagnetic Cu_2F_5 lattice, temperature-dependent reversal of the direction of transverse transport suggests potential applications in magnon spintronics. Finally, the study of the non-Hermitian checkerboard lattice revealed non-quantized Hall conductivity and exceptional points, unique to such Hamiltonians.

Unified by their two-band dispersion and shared mathematical formalism, these systems provide insights into Berry curvature, topology, and transverse transport in crystal lattices. The findings highlight applications in magnon spintronics and deepen understanding of electronic transport in non-Hermitian systems.

Keywords: Hall effect, Magnons, Non-Hermitian, Topology.

Contents

APPENDIX 85

1 Introduction

Topological effects in condensed matter systems have been intensely studied since the discovery of the *quantum Hall effect* (QHE) by von Klitzing *et al* [1]. This phenomenon arises with the application of strong magnetic fields in a two-dimensional electron gas, breaking time-reversal symmetry and creating a transverse Hall current in the lattice. The Hall conductance is quantized and characterized by a topological invariant, known as the *Chern number* or *TKKN integer* [2,3]. *Topology* is the branch of mathematics that studies properties which remain invariant under continuous transformations of a system. For example, the *genus* is the "number of holes" on an oriented closed surface. The sphere has *genus* 0, and the torus has *genus* 1. The *genus* remain invariant under continuous deformations of the surface ("stretching"). The only way to change the *genus* is to "tear apart" or "glue together" pieces of surface, which are not continuous transformations. Hence, the genus is a topological invariant. Another example is the winding number of a closed oriented curve, which is the number of times this curve encircles the origin counterclockwise.

In condensed matter insulating systems, the Chern number is calculated from the bulk wave functions. When $C \neq 0$, the edge of the sample holds conducting modes which are robust against perturbations. This is the bulk-edge correspondence [4], and the system is called a *topological insulator* (TI). The system can present different Chern numbers for different theory parameters, making it possible to construct a topological phase diagram.

In a topological insulator in equilibrium, the bulk states are insulating but the the egde of the sample holds conducting states. This can be understood semiclassically as follows. When the Chern number is non-zero, the magnetic field creates cyclotron motion of the electronic wave packets inside the bulk. Different pieces of neighboring orbits overlap and the current in the bulk vanishes, but in the edges the skipping orbits create conducting edge states. In a strip geometry, electrons at the top edge move in a different direction than at the bottom edge: the current is chiral. These edge states are robust against perturbations due to their topological nature.

The same effect can happen in a two-dimensional lattice systems even in the absence of an external magnetic field. In this case, complex hopping induces magnetic fluxes which results in quantized Hall conductance and edge states, in what is called the *anomalous quantum Hall effect* (AQHE) [5,6]. A similar phenomenon is the *quantum spin Hall effect* (QSHE), when time-reversal symmetry is not broken [5, 7–12]. In this case, strong spin-orbit couplings act differently in spin up and down electrons, creating a transverse spin current without net electronic flow. In the equilibrium, that results in

helical edge modes, when at each edge of the sample electrons of opposite spins flow in opposite directions in separate conducting channels. In these systems the Chern number is zero, but a different topological integer ± 1 defines a $\mathbb{Z}_2$ topological insulator.

In light of that, we can introduce the notion of topological states of matter, characterized by topological indices [13, 14]. Within this approach, a topological insulator (TI) is an insulating system which has a non-trivial ($\neq 0$) topological index. The bulk-edge correspondence assures the existence of robust edge states in topological insulators. In the so-called Chern insulators, the Chern number is the topological index. It can be calculated through the integration of the *Berry curvature* over the Brillouin zone [15]. The Berry curvature is a local function of the crystal momentum which is assigned to each energy band. It is related to the Berry phase that an electronic state acquires when transported in a closed loop due to the Aharonov-Bohm effect [16]. The Chern number can be easily calculated from the eigenstates of the bulk Hamiltonian through the Berry curvature.

In ordered magnetic lattices, the spin carriers are magnons and not electrons. *Magnons* are spin-wave excitations of the ground state in systems of localized spins. They are bosonic quasiparticles which carry definte spin but are naturally chargeless. Because of that, they have the advantage of showing much lower dissipation in comparison to electron transport, being of great interest in spintronics [17]. Much like electrons, they can show topologically protected edge modes, robust against structural or magnetic disorder and that can form ideal waveguides for long-range magnon transport [18]. That allows one to make an analogy between topological electrons and magnons, and the formalism developed for electronic systems can be fully applied to magnonic systems. In fact, it was argued by Nakata *et al* that magnons in a ferromagnetic lattice behave as a complete analogue of the QHE, while antiferromagnetic magnons can be an analogue of the QSHE [19, 20]. These systems can be considered *topological magnon insulators* (TMIs), classified by topological indices. In this case, the term "insulator" is applied to gapped magnonic systems only as an analogy, as there is no Fermi level in bosonic systems.

Regarding the bulk transport properties of topological systems, electrons and magnons present Hall transport in response to electromagnetic fields. That can be seen as a result of the Aharonov-Bohm effect in the case of electrons, and the Aharonov-Casher effect in the case of magnons [21, 22]. For magnons, the spin Hall effect can happen even for non-topological systems, as long as the Berry curvature is not null [23–33]. Another important transport effect is related to thermal diffusion, when particles flow in a transverse direction to a thermal gradient. This *thermal Hall effect* has been studied mainly in magnetic systems. The thermal Hall coefficients depend on the Berry curvature, much like the Hall conductivity does [24, 27].

Concerning the experimental aspect, it is established that magnons can be generated and detected via spin Hall effect and charge-to-spin current conversion [34, 35]. The above-

mentioned Hall-like effects in magnons also have strong experimental evidence: the thermal Hall effect of magnons was firstly detected in ferromagnetic materials with pyrochlore geometry [25, 36], and after, in kagome lattices both in the ordered and disordered phase [37–39]. The magnonic spin Nernst effect has been reported for the $MnPS_3$, an antiferromagnetic insulator with honeycomb geometry [40], and other materials seem promising [41]. The experimental evidence, together with the patent advantages of magnon transport in spintronics, justifies the theoretical study of magnons and its topological features in different lattice geometries as an effort to lay ground for future experiments and applications.

Another interesting platform to study the connection between topology and transverse transport is in open systems, subjected to loss and gain of particles and energy. While topological effects in regular, energy-conserving Hamiltonians have robust theoretical and experimental evidence, this investigation in non-conservative open systems is still in progress. One way to model an open system is with a non-Hermitian Hamiltonian. The non-Hermitian formalism can be applied to a variety of quantum and classical systems [42–46]. A highly studied phenomenon related to those systems is the *non-Hermitian skin effect*, in which the majority of bulk states are localized at the edges of a sample with open-boundary conditions [47]. Experimental evidence of this effect can be found in many systems, including photonic crystals and acoustic topological insulators [45, 48, 49]. Another unique characteristic of non-Hermitian Hamiltonians are the *exceptional points* in the Brillouin zone, which are points where the Hamiltonian is defective. They have been experimentally observed in different systems, mainly in photonic crystals [42, 50–55].

Specifically for electronic insulators, it is known that Chern topology works differently in non-Hermitian systems compared to their Hermitian counterpart. The main difference is that the non-Hermiticity spoils the bulk-edge correspondence. As a consequence, the topological edge states are not related to the bulk Chern number, although possibly present. Also, the Hall conductivity is no longer quantized [56, 57]. Some efforts have been made to restore the bulk-edge correspondence, defining a non-Bloch Chern number which seems to be related to the presence of edge states [58–61].

This thesis reports investigations on the Chern topology and transverse transport in several two-dimensional lattices. In Chapter 2 we present the mathematical methodology that links the transverse transport to the the Berry curvature and Chern topology of the eigenstates. In Chapter 3, a modified version of the Lieb lattice is presented, and its magnonic structure is studied in a ferromagnetic ordering. In Chapter 4, the antiferromagnetic Union Jack lattice is investigated, and anharmonic contributions are included with a mean-field approach. The antiferromagnetic brickwall lattice is studied in Chapter 5. In Chapter 6, we present a ferrimagnetic model for the layered Cu_2F_5 crystal, which has the same geometry as the modified Lieb lattice in Chapter 3. In Chapter 7, the non-Hermitian

fermionic checkerboard lattice is presented, where very unique features arise due to its non-Hermiticity. The final remarks are made in Chapter 8.

2 Transverse transport - methodology

In this chapter the mathematical methods used to study the topology and Hall-like transport in two-dimensional lattices are presented. The linear response theory establishes a connection between the Berry curvature and the transport coefficients. The Berry curvature can give rise to topological phases in those systems.

2.1 Linear response theory

The assumption of the linear response theory is that equilibrium states can be perturbed by an external field, and for weak perturbations, the system's observables respond linearly. Without perturbation, the many-body Hamiltonian is H_0, and the time-independent Schrödinger equation read:

$$H_0 \left| n^0 \right\rangle = \epsilon_n^0 \left| n^0 \right\rangle. \tag{2.1}$$

When a perturbation $H'(t)$ is turned on in $t_0 = -\infty$, a time-dependent Hamiltonian $H(t) = H_0 + H'(t)$ is defined, which satisfies ($\hbar \equiv 1$):

$$H(t) \left| n(t) \right\rangle = i \frac{\partial}{\partial t} \left| n(t) \right\rangle. \tag{2.2}$$

Using the definitions

$$\begin{aligned} \left| n(t) \right\rangle &\equiv e^{-iH_0 t} \left| n_I(t) \right\rangle \\ H'(t) &\equiv e^{-iH_0 t} H'_I(t) e^{iH_0 t}, \end{aligned} \tag{2.3}$$

we can show that the Schrödinger equation in the interaction picture is:

$$H'_I(t) \left| n_I(t) \right\rangle = i \frac{\partial}{\partial t} \left| n_I(t) \right\rangle. \tag{2.4}$$

This equation has formal solution (using the Dyson series) up to linear order as

$$\left| n_I(t) \right\rangle \simeq \left| n^0 \right\rangle - i \int_{-\infty}^{t} dt'\, H'_I(t') \left| n^0 \right\rangle, \tag{2.5}$$

and with this, the evolved state $\left| n_I(t) \right\rangle$ is written in terms of the unperturbed state $\left| n^0 \right\rangle$ and the perturbation $H'_I(t)$.

Turning to a generic observable A, the thermal average of its expected value without perturbation is

$$\langle A \rangle_0 = \frac{1}{Z_0} \sum_n e^{-\beta \epsilon_n^0} \left\langle n^0 \right| A \left| n^0 \right\rangle. \tag{2.6}$$

When the perturbation is turned on, the states evolve to $|n(t)\rangle$, and the thermal average is

$$\langle A(t)\rangle = \frac{1}{Z_0} \sum_n e^{-\beta \epsilon_n^0} \langle n_I(t)| A_I(t) |n_I(t)\rangle = \langle A\rangle_0 + \delta\langle A(t)\rangle. \tag{2.7}$$

Note that the equilibrium thermal distribution $e^{-\beta \epsilon_n^0}$ is used. This is valid when the perturbation is fast enough compared to the time to reach the thermal equilibrium, so that the thermal distributions do not change. That is called *adiabatic response*. Using Eq. 2.5 to rewrite the equation above, we can show that:

$$\delta\langle A(t)\rangle = i \int_{-\infty}^{t} dt' \, \langle [A_I(t), H_I'(t')]\rangle_0. \tag{2.8}$$

We now assume spatial and temporal dependence ($x \equiv (\mathbf{r}, t)$). We also assume that the perturbation H' can be written as $H'(t') = \int d\mathbf{r}' B(\mathbf{r}', t') f(\mathbf{r}', t')$, where $B(\mathbf{r}, t)$ is an operator and $f(\mathbf{r}, t)$ is a scalar function, so that

$$\delta\langle A(x)\rangle = -i \int_{-\infty}^{\infty} dx' \, \theta(t - t') \langle [A_I(x), B_I(x')]\rangle_0 f(x'), \tag{2.9}$$

and defining a *response function* as

$$\chi_{AB}(x, x') = -i\theta(t - t') \langle [A_I(x), B_I(x')]\rangle_0, \tag{2.10}$$

we obtain the *Kubo formula*

$$\delta\langle A(x)\rangle = \int dx' \, \chi_{AB}(x, x') f(x'). \tag{2.11}$$

If the system is spatially homogeneous (which is assumed from now on), the convolution theorem can be used to write the Kubo formula in momentum space:

$$\delta\langle A(\mathbf{q}, \omega)\rangle = \chi_{AB}(\mathbf{q}, \omega) f(\mathbf{q}, \omega). \tag{2.12}$$

2.2 Current response

One wants to know how the electric current $\langle \mathbf{J}\rangle$ reacts to an electromagnetic field. Applying the linear-response formalism to an electronic system in an external vector potential $\mathbf{A}$ (do not confuse with the observable A in the last section). The unperturbed Hamiltonian is

$$H_0 = \int d\mathbf{r}\psi^\dagger \left(\frac{p^2}{2m} + V\right)\psi, \tag{2.13}$$

and the perturbed Hamiltonian is found making the substitution $\mathbf{p} \to \mathbf{p} + \frac{e}{c}\mathbf{A}$, getting:

$$H = H_0 + H' = H_0 + \frac{e}{c} \int d\mathbf{r}\, \mathbf{J} \cdot \mathbf{A}, \tag{2.14}$$

where the current $\mathbf{J}$ is defined as

$$\mathbf{J} \equiv \frac{e}{mc}\mathbf{A}\psi^\dagger\psi - i\frac{1}{2m}\left[\psi^\dagger\nabla\psi - \left(\nabla\psi^\dagger\right)\psi\right]. \tag{2.15}$$

The first and second terms are called diamagnetic ($\mathbf{J}^D$) and paramagnetic current ($\mathbf{J}^P$), respectively. The paramagnetic term can be rewritten using the Kubo formula (Eq. 2.11) making the substitutions:

$$A \to J_\mu$$
$$B \to J_\nu$$
$$f \to A_\nu. \tag{2.16}$$

Supposing the equilibrium current is zero, the Kubo formula for the conductivity is:

$$\langle J_\mu(x)\rangle = \frac{e}{c}\int dx'\,\chi_{\mu\nu}(x,x')\,A_\nu(x'), \tag{2.17}$$

with a current-current response function defined as ($m \equiv 1$):

$$\chi_{\mu\nu}(x,x') = \delta_{\mu\nu}\delta(x-x')\,\rho(x) - i\theta(t-t')\left\langle\left[J_\mu^P(x), J_\nu^P(x')\right]\right\rangle$$
$$= \chi_{\mu\nu}^D(x,x') + \chi_{\mu\nu}^P(x,x'). \tag{2.18}$$

The diamagnetic response (first term) is zero when $\mu \neq \nu$, which is the case of the transverse response.

In the space of the frequencies, one has

$$\chi_{\mu\nu}(\mathbf{r},\mathbf{r}',\omega) = \chi_{\mu\nu}^D(\mathbf{r},\mathbf{r}',\omega) + \chi_{\mu\nu}^P(\mathbf{r},\mathbf{r}',\omega) \tag{2.19}$$

with

$$\chi_{\mu\nu}^P(\mathbf{r},\mathbf{r}',\omega) = -i\int_0^\infty dt\,e^{i\omega t}\left\langle\left[J_\mu^P(\mathbf{r},t), J_\nu^P(\mathbf{r}',0)\right]\right\rangle. \tag{2.20}$$

We now have to compute the thermal average. Remembering that the operators are written in the interaction picture, so $J_\mu^P(\mathbf{r},t) = e^{iH_0 t}J_\mu^P(\mathbf{r},0)e^{-iH_0 t}$, we get

$$\left\langle\left[J_\mu^P(\mathbf{r},t) J_\nu^P(\mathbf{r}',0)\right]\right\rangle = \sum_n \frac{e^{-\beta\epsilon_n}}{Z}\langle n|J_\mu^P(\mathbf{r},t)J_\nu^P(\mathbf{r}',0)|n\rangle$$
$$= \sum_{mn}\frac{e^{-\beta\epsilon_n}}{Z}e^{i(\epsilon_n - \epsilon_m)t}\langle n|J_\mu^P(\mathbf{r},0)|m\rangle\langle m|J_\nu^P(\mathbf{r}',0)|n\rangle. \tag{2.21}$$

In the second quantization formalism, the many-body operator $J_\mu^P(\mathbf{r},0)$ can be written in terms of the creation and annihilation operator and the single particle operator $j_\mu(\mathbf{r})$:

$$J_\mu^P(\mathbf{r},0) = \sum_{ij}\langle i|j_\mu(\mathbf{r})|j\rangle a_i^\dagger a_j. \tag{2.22}$$

Substituting that in Eq. 2.21, we get terms of the form $\langle n| a_i^\dagger a_j |m\rangle \langle m| a_k^\dagger a_l |n\rangle$. Making the assumption that the fermions do not interact with each other (free fermions), from Wick's theorem the only non-zero terms of that form are:

$$\sum_n \frac{e^{-\beta\epsilon_n}}{Z} \langle n| a_i^\dagger a_i |m\rangle \langle m| a_j^\dagger a_j |n\rangle = f_i f_j$$

$$\sum_n \frac{e^{-\beta\epsilon_n}}{Z} \langle n| a_i^\dagger a_j |m\rangle \langle m| a_j^\dagger a_i |n\rangle = f_i \left(1 - f_j\right), \tag{2.23}$$

where f_i is the Fermi-Dirac distribution $f_i = \left(e^{\beta\epsilon_i} + 1\right)^{-1}$. With these results, $\chi_{\mu\nu}^P$ in Eq. 2.20 can be written as

$$\chi_{\mu\nu}^P \left(\mathbf{r}, \mathbf{r}', \omega\right) = -i \sum_{ij} \int_0^\infty dt\, e^{i\omega t} e^{i(\epsilon_i - \epsilon_j)t} \langle i| j_\mu(\mathbf{r}) |j\rangle \langle j| j_\nu(\mathbf{r}') |i\rangle \left(f_i - f_j\right)$$

$$= \sum_{ij} \left(f_i - f_j\right) \frac{\langle i| j_\mu(\mathbf{r}) |j\rangle \langle j| j_\nu(\mathbf{r}') |i\rangle}{\omega + \epsilon_i - \epsilon_j}. \tag{2.24}$$

In the momentum space:

$$\chi_{\mu\nu}^P \left(\mathbf{q}, \omega\right) = \frac{1}{V} \sum_{ij} \left(f_i - f_j\right) \frac{\langle i| j_\mu(\mathbf{q}) |j\rangle \langle j| j_\nu(-\mathbf{q}) |i\rangle}{\omega + \epsilon_{ij}}, \tag{2.25}$$

where $\epsilon_{ij} \equiv \epsilon_i - \epsilon_j$. Bringing back the diamagnetic part, the full current-current response function is:

$$\chi_{\mu\nu} \left(\mathbf{q}, \omega\right) = \delta_{\mu\nu} \rho_0 + \frac{1}{V} \sum_{ij} \left(f_i - f_j\right) \frac{\langle i| j_\mu(\mathbf{q}) |j\rangle \langle j| j_\nu(-\mathbf{q}) |i\rangle}{\omega + \epsilon_{ij}}. \tag{2.26}$$

Recall that the response function gives the current response to an external electric potential:

$$\langle J_\mu(\mathbf{q}, \omega)\rangle = \frac{e}{c} \chi_{\mu\nu}(\mathbf{q}, \omega) A_\nu(\mathbf{q}, \omega). \tag{2.27}$$

From the relation between electric field and potential, $\mathbf{E}(\omega) = i\frac{\omega}{c}\mathbf{A}(\omega)$, and using the definition of the *electrical conductivity*

$$\sigma_{\mu\nu}(\mathbf{q}, \omega) \equiv i\frac{e^2}{\omega} \chi_{\mu\nu}(\mathbf{q}, \omega), \tag{2.28}$$

we rewrite 2.27 as:

$$\langle -e J_\mu(\mathbf{q}, \omega)\rangle = \sigma_{\mu\nu}(\mathbf{q}, \omega) E_\nu(\omega). \tag{2.29}$$

The equation above shows the dependence of the expected value of the electrical current $-e J_\mu$ as a response to the electrical field $\mathbf{E}$. One can show that the conductivity $\sigma_{\mu\nu}$, for uniform and static fields ($\mathbf{q} = \omega = 0$), can be written as

$$\sigma_{\mu\nu} = -i\frac{e^2}{\hbar V} \sum_{ij} f_i \frac{\langle i| p_\mu |j\rangle \langle j| p_\nu |i\rangle - \langle i| p_\nu |j\rangle \langle j| p_\mu |i\rangle}{\epsilon_{ij}^2}. \tag{2.30}$$

2.3 Integer quantum Hall effect

Let us now establish that the system described here is a two-dimensional lattice, where $\mu, \nu = x, y$ and the Bloch states are $|n, \mathbf{k}\rangle$. We also assume it is a two-band insulating system, and that the Fermi level is located within the gap. We focus on the Hall conductivity, when $\mu \neq \nu$, and the current response is transverse to the field direction. Noting that $p_\mu = \frac{\partial H}{\partial k_\mu}$, Eq. 2.30 can be written as

$$\sigma_{xy} = -\frac{e^2}{h} \sum_n \int \frac{d^2 k}{4\pi} f_n(\mathbf{k}) i \left[\left\langle \frac{\partial u_{nk}}{\partial k_x} \middle| \frac{\partial u_{nk}}{\partial k_y} \right\rangle - \left\langle \frac{\partial u_{nk}}{\partial k_y} \middle| \frac{\partial u_{nk}}{\partial k_x} \right\rangle \right], \tag{2.31}$$

where u_{nk} is the periodic part of the Bloch eigenfunction, and the continuum limit is assumed, so the summation becomes an integral.

The term inside squared brackets is called the *Berry curvature* $\Omega_{xy}^n(\mathbf{k})$, and the Hall conductivity is written as

$$\sigma_{xy} = -\frac{e^2}{h} \sum_n \int \frac{d^2 k}{4\pi} f_n(\mathbf{k}) \Omega_{xy}^n(\mathbf{k}). \tag{2.32}$$

That is the fundamental expression for Hall conductivity used in this work. For fermions at zero temperature, $f_n(\mathbf{k}) = 1$ for the occupied band, so that

$$\sigma_{xy} = -\frac{e^2}{h} \int \frac{d^2 k}{4\pi} \Omega_{xy}^{val}(\mathbf{k}) \equiv -\frac{e^2}{h} C. \tag{2.33}$$

C is an integer: the Chern number of the valence band. The equation above describes the *integer Hall effect*, which was first described for a 2D electron gas [1]. The Hall conductivity is quantized according to the Chern number, also known as the TKNN integer [2, 3]. The Chern number defines a topological class, and in the case of a two-band insulator, it has a natural geometrical interpretation. As $\mathbf{k}$ spreads over the Brillouin torus, a parameter vector $\mathbf{d}$ describes a surface. The Chern number represents the number of times this surface wraps around the origin (the winding number of the surface).

Systems with $C \neq 0$ must break time-reversal symmetry. This can happen with an external magnetic field or a clever arrangement of magnetic fluxes inside the unit cell of condensed-matter systems [6]. These systems are Chern topological insulators. In the interface of a topological insulator with a trivial insulator, the energy gap closes. The consequence is the emergence of one or more conducting states at the interface - the so-called edge states. Because the vacuum (or the air) can be considered a trivial insulator, the surface of a sample of a TI holds one or more conducting edge states, in spite of the the bulk being an insulator. The bulk-edge correspondence dictates that the edge states are robust against perturbation. Beyond the discovery of Chern insulators, the topological approach was fruitful in numerous models, like magnetic, photonic, acoustic, and superconducting systems [62–67].

2.4   Magnon Hall transport

As mentioned before, magnons are quantized spin-waves in a system of localized spins. They carry spin, but are chargeless. When a magnonic system is perturbed by a magnetic field gradient $\nabla \mathbf{B}$, a spin current is generated in what we call the *spin Hall effect of magnons*. In the linear response limit, we have

$$\left\langle J_x^S \right\rangle = \sigma_{xy}^S \left(-\partial_y B \right), \tag{2.34}$$

where σ_{xy}^S is the *spin Hall conductivity* given by (the integration is over the Brillouin zone)

$$\sigma_{xy}^S = -\frac{(g\mu_B)^2}{\hbar} \sum_\lambda \int \frac{d^2k}{V_{BZ}} \, n_\lambda \left(\mathbf{k} \right) \Omega_{xy}^\lambda \left(\mathbf{k} \right). \tag{2.35}$$

The thermal population $n_\lambda \left(\mathbf{k} \right)$ is given by the Bose–Einstein distribution $n_\lambda \left(\mathbf{k} \right) = (e^{\beta \epsilon_\lambda (\mathbf{k})} - 1)^{-1}$. As magnons are bosons, there is no Fermi level, and both bands are always populated. The conductivity is no longer quantized. Nevertheless, the bands are characterized by a Chern number defined as

$$C_\lambda = \int \frac{d^2k}{4\pi} \Omega_{xy}^\lambda \left(\mathbf{k} \right). \tag{2.36}$$

The sum of the Chern numbers of all bands must be zero [16]. Hence, for a two-band system, the Chern numbers appear in pairs $\pm C$. The Berry curvature $\Omega_{xy}^\lambda \left(\mathbf{k} \right)$ of the λ magnon band is defined as in the electronic case.

$$\Omega_{xy}^\lambda \left(\mathbf{k} \right) = i \left[\left\langle \frac{\partial u_{\lambda k}}{\partial k_x} \middle| \frac{\partial u_{\lambda k}}{\partial k_y} \right\rangle - \left\langle \frac{\partial u_{\lambda k}}{\partial k_y} \middle| \frac{\partial u_{\lambda k}}{\partial k_x} \right\rangle \right], \tag{2.37}$$

where $u_{\lambda k}$ are the magnonic eigenfunctions. When the system is gapped and the Chern number is non-trivial, the system is a topological magnon insulator (TMI). It is worth mentioning that, as there is no Fermi level for bosonic systems, the term "insulator" can be applied only as an analogy: for bosons in finite temperature, all bands are always occupied, and there is no filled or empty bands. Nevertheless, magnonic topological insulators, much like electronic insulators, present topologically protected edge modes, robust against structural or magnetic disorder and that can form ideal waveguides for long-range magnon transport [18].

Another important transport phenomenon is the magnon current that emerges as a consequence of a temperature gradient. Temperature is not a dynamical force, but a "statistical force" that affects the particles through the distribution function [68]. To construct the linear response theory, one must use a fictitious gravitational potential to fit temperature variations into the linear response formalism. That field perturbs the system (like the electromagnetic field does) generating a transverse spin current (*spin Nernst effect*

of magnons) and energy current (*thermal Hall effect of magnons*) [24, 69–71]. These effects rely on the orbital angular momentum of the magnon states [27]. In the linear response regime, the spin and energy currents due to a thermal gradient are written as

$$\left\langle J_x^S \right\rangle = \alpha_{xy} \left(-\partial_y T\right) \tag{2.38}$$

$$\left\langle J_x^E \right\rangle = \kappa_{xy} \left(-\partial_y T\right). \tag{2.39}$$

α_{xy} is called *spin Nernst coefficient*, and κ_{xy} is the *thermal Hall conductivity*. Together with the spin Hall conductivity σ_{xy}, those transverse transport coefficients are the focus of the studies presented on this thesis, and were calculated for various two-dimensional systems. The expressions for each of those are [27, 28, 71–73]

$$\sigma_{xy} = -\frac{1}{\hbar} \left(g\mu_B\right)^2 \sum_\lambda \int \frac{d^2k}{V_{BZ}} \, n_\lambda\left(\mathbf{k}\right) \Omega_{xy}^\lambda\left(\mathbf{k}\right) \tag{2.40}$$

$$\alpha_{xy} = -\frac{k_B}{\hbar} g\mu_B \sum_\lambda \int \frac{d^2k}{V_{BZ}} \, c_1\left[n_\lambda\left(\mathbf{k}\right)\right] \Omega_{xy}^\lambda\left(\mathbf{k}\right) \tag{2.41}$$

$$\kappa_{xy} = -\frac{k_B^2 T}{\hbar} \sum_\lambda \int \frac{d^2k}{V_{BZ}} \, c_2\left[n_\lambda\left(\mathbf{k}\right)\right] \Omega_{xy}^\lambda\left(\mathbf{k}.\right) \tag{2.42}$$

The functions c_1 and c_2 are defined as

$$c_1\left(x\right) = \left(1+x\right)log\left(1+x\right) - x\,log\,x$$

$$c_2\left(x\right) = \left(1+x\right)\left(ln\frac{1+x}{x}\right)^2 - \left(ln\,x\right)^2 - 2Li_2\left(-x\right), \tag{2.43}$$

and $Li_2\left(x\right)$ is Spence's dilogarithm function. We stress that for bosons, the transverse transport coefficients (2.40)-(2.42) are not quantized, even thought the Chern number is. Also, even for a zero Chern number the coefficients can be non-zero.

3 Ferromagnetic modified Lieb lattice

In this chapter, the topology and Hall transport of magnons in a modified Lieb lattice is studied. This study was published in Ref. [74]. Magnons are spin wave excitations of the ground state in a lattice of localized spins. When magnon bands have non-null Berry curvature, Hall-like transport effects can arise. Since magnons are bosons, magnonic systems are intrinsically different from electronic ones, which motivates their study. A notable fact is that magnons favor dissipationless transport because of their uncharged nature. While topological effects in magnon systems were first discovered in a three-dimensional material with the geometry of the pyrochlore lattice [25], the main theoretical interest nowadays falls on two-dimensional lattices, where the most studied geometries are the honeycomb [75–77] and the kagome lattices [24, 31, 78–80]. Other lattices that were predicted to hold topological magnon effects are the Shastry-Sutherland [81, 82], square [83], checkerboard [84–89] and Lieb [90] lattices.
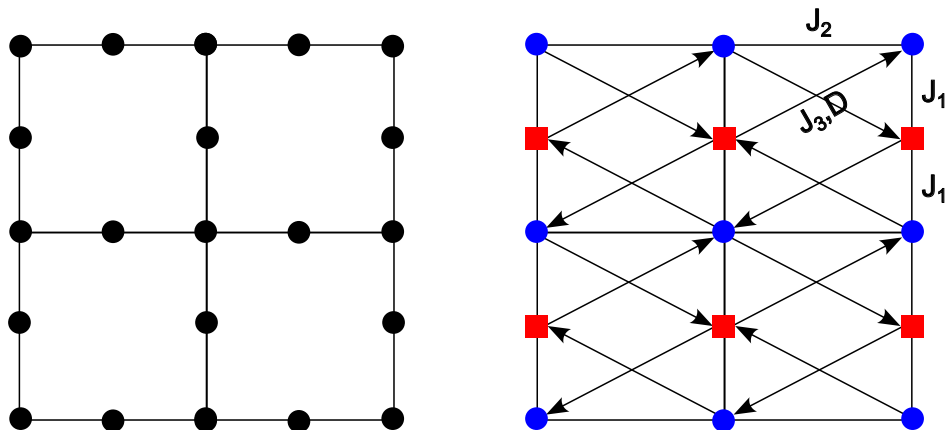
Figure 1 – The original Lieb lattice (left) and modified Lieb lattice studied in this chapter (right). Circles represent the A sites, and squares represent the B sites. The horizontal and vertical lines are ferromagnetic exchange bonds (J_1 between A and B; J_2 between two A sites). The diagonal lines represent both J_3 and Dzyaloshinskii-Moriya interaction. The latter has $\nu_{ij} = +1$ along the arrows, and -1 against them.

The Lieb lattice is particularly interesting because it is the geometry that CuO_2 planes assume in high-T_c cuprate superconductors [91]. It has also been identified in some organic compounds as a "hidden lattice" [92]. Magnonic systems in the Lieb lattice have been intensely investigated in the context of the Heisenberg model. In Ref. [90] it was shown that a complex hopping between next-near-neighbours can induce topological insulating phases.

In this chapter we report the investigation of a modified version of the ferromagnetic Lieb lattice, where one of the lattice sites was removed. This lattice has two inequivalent sites (A and B) in each square unit cell (whose side was taken as equal to one, Fig. 1). The spin ordering is off-plane ferromagnetic, and the system is described by a Heisenberg model with exchange interactions between the three first neighbors. Transverse transport effects are induced by a Dzyaloshinskii-Moriya interaction (DMI) between the next-next-near neighbors. The Hamiltonian is:

$$H = - J_1 \sum_{\langle i,j \rangle} \left[\mathbf{S}_i \cdot \mathbf{S}_j + (\lambda - 1) S_i^z S_j^z \right] - J_2 \sum_{\langle\langle i,j \rangle\rangle \in A} \left[\mathbf{S}_i \cdot \mathbf{S}_j + (\lambda - 1) S_i^z S_j^z \right]$$
$$- J_3 \sum_{\langle\langle\langle i,j \rangle\rangle\rangle} \left[\mathbf{S}_i \cdot \mathbf{S}_j + (\lambda - 1) S_i^z S_j^z \right] - D \sum_{\langle\langle\langle i,j \rangle\rangle\rangle} \nu_{ij} \hat{\mathbf{z}} \cdot \mathbf{S}_i \times \mathbf{S}_j - B \sum_i S_i^z. \tag{3.1}$$

There are ferromagnetic exchange interactions between near-neighbors A and B (strength J_1, vertical lines in Fig. 1) and next-near-neighbors A (strength J_2, horizontal lines). In all exchange interactions there is an anisotropy λ on the z terms. When $\lambda > 1$, the exchange term is minimized for spins in the z direction [93, 94]. On the diagonals between A and B, there are a J_3 exchange interaction and a Dzyaloshinskii-Moriya interaction of the form $-\mathbf{D}_{ij} \cdot (\mathbf{S}_i \times \mathbf{S}_j)$. The latter is also called antisymmetric exchange and has its physical origin in the spin-orbit coupling of the material. This interaction is responsible for the finite Berry curvature and Hall-like transport effects. The vector $\mathbf{D}_{ij}$ is antisymmetric by exchange $i \leftrightarrow j$, so the bond is oriented. We take this DM vector as $\mathbf{D}_{ij} = D\nu_{ij}\hat{\mathbf{z}}$ (perpendicular to the lattice plane), with $\nu_{ij} = \pm 1$ following or against the arrows.

The DMI tends to orient two interacting spins in a perpendicular orientation, and for sufficiently large D (comparable to J_1) the ground state is no longer a collinear ferromagnet but a spin spiral: the magnetic sublattices tilt away from their parallel alignment. Therefore, only small values of D are considered, in order to preserve the collinear state. High values of the off-plane magnetic field $\mathbf{B} = B\hat{\mathbf{z}}$ ensure the off-plane ordering via Zeeman interaction (last term in Eq. 3.1). The same effect could be achieved with a single-ion anisotropy.

3.1 Ferromagnetic magnons - formalism

Supposing a bidimensional spin system with a ferromagnetic ground state, where all the spins are ordered in the off-plane direction, we rewrite the spin operators using the

Holstein-Primakoff (HP) transformation [95]:

$$S^+ (\mathbf{r}) = \sqrt{2S}\sqrt{1 - \frac{a^\dagger (\mathbf{r}) a (\mathbf{r})}{2S}} a (\mathbf{r})$$

$$S^- (\mathbf{r}) = \sqrt{2S} a^\dagger (\mathbf{r}) \sqrt{1 - \frac{a^\dagger (\mathbf{r}) a (\mathbf{r})}{2S}}$$

$$S^z (\mathbf{r}) = S - a^\dagger (\mathbf{r}) a (\mathbf{r}) . \tag{3.2}$$

We stress that this transformation is only appliable to spins ordered in an off-plane configuration (in our case, the z direction). That off-plane ground state should be ensured even at non-zero temperature. To achieve this it is important to add some kind of anisotropy in the Hamiltonian, otherwise the system would have no long-range order according to the Mermim-Wagner theorem [96]. The operators $a^{(\dagger)} (\mathbf{r})$ are the bosonic creation and anihilation operators at the $\mathbf{r}$ point. We assume a periodic lattice with N inequivalent sites in the basis, and introduce N inequivalent operators $a_1^{(\dagger)}, a_2^{(\dagger)}, ..., a_N^{(\dagger)}$. These operators obey the bosonic commutation relation:

$$\left[a_m (\mathbf{r}) , a_n^\dagger (\mathbf{r}') \right] = \delta_{mn} \delta_{\mathbf{rr}'} . \tag{3.3}$$

In systems with two inequivalent sites per unit cell, like the modified Lieb lattice, two magnon operators are used: $a^{(\dagger)}$ and $b^{(\dagger)}$. Assuming the magnons do not interact with each other, the square root in the HP transformation is expanded to zeroth order (otherwise, non-harmonic terms would be generated in the Hamiltonian, indicating magnon interaction):

$$\begin{array}{cccc} S_i^+ = \sqrt{2S}\, a_i, & S_i^- = \sqrt{2S}\, a_i^\dagger, & S_i^z = S - a_i^\dagger a_i, & i \in A \\ S_i^+ = \sqrt{2S}\, b_i, & S_i^- = \sqrt{2S}\, b_i^\dagger, & S_i^z = S - b_i^\dagger b_i, & i \in B \end{array} \tag{3.4}$$

This is the so called *linear spin wave* (LSW) regime. The subscript i indexes the quantized position in the lattice. Any ferromagnetic spin Hamiltonian in the ordered phase can be described within this approach. After performing the HP transformation, the terms with order higher than two in the magnon operators are ignored, together with the constant terms, which represent the classic vacuum energy. Fourier transforming, we get a harmonic Hamiltonian

$$H = \sum_k \psi_k^\dagger \left(h_0(\mathbf{k}) I_2 + h_x(\mathbf{k}) \sigma_x + h_y(\mathbf{k}) \sigma_y + h_z(\mathbf{k}) \sigma_z \right) \psi_k$$

$$\equiv \sum_k \psi_k^\dagger H_k \psi_k, \tag{3.5}$$

where $\psi_k^\dagger = \begin{pmatrix} a_k^\dagger & b_k^\dagger \end{pmatrix}$, σ_i are the Pauli matrices and I_2 is the 2x2 identity matrix. The Hamiltonian matrix H_k is written explicitly as

$$H_k = \begin{pmatrix} h_0 + h_z & h_x - ih_y \\ h_x + ih_y & h_0 - h_z \end{pmatrix} \tag{3.6}$$

The parameter vector $\mathbf{h}$ is defined as $\mathbf{h}(\mathbf{k}) \equiv (h_x(\mathbf{k}), h_y(\mathbf{k}), h_z(\mathbf{k}))$. The diagonalization of the Hamiltonian matrix H_k leads to a two-band model with eigenvalues written as:

$$\epsilon_\pm(\mathbf{k}) = h_0(\mathbf{k}) \pm h(\mathbf{k}). \tag{3.7}$$

Here, $h(\mathbf{k}) \equiv |\mathbf{h}(\mathbf{k})| = \sqrt{h_x^2(\mathbf{k}) + h_y^2(\mathbf{k}) + h_z^2(\mathbf{k})}$. The explicit form of the eigenvectors $\varphi_k^\pm$ in the ψ_k basis is:

$$\varphi_k^+ = \begin{pmatrix} p_1 e^{-i\theta} \\ p_2 \end{pmatrix} ; \quad \varphi_k^- = \begin{pmatrix} p_2 e^{-i\theta} \\ -p_1 \end{pmatrix}, \tag{3.8}$$

where (the $\mathbf{k}$ dependence is implicit):

$$p_1 = \sqrt{\frac{h + h_z}{2h}}, \quad p_2 = \sqrt{\frac{h - h_z}{2h}}, \quad tan\,\theta = \frac{h_y}{h_x}.$$

Both states carry spin -1 (opposite to the ferromagnetic order). The linear spin wave formalism is general and the results above can be applied for any FM two-band system, i. e., lattice systems with two inequivalent sites per unit cell. To obtain the magnon bands one should merely find the parameters h_0, h_x, h_y and h_z for the specific system and apply them to Eq. 3.7.

3.2 Magnon bands

For the model studied here (Eq. 3.1), the Hamiltonian parameters are:

$$h_0(\mathbf{k}) = SJ_2(\lambda - cos\,k_x) + 2S\lambda(J_1 + 2J_3) + B$$
$$h_x(\mathbf{k}) = -2S\,cos\,\frac{k_y}{2}(J_1 + 2J_3\,cos\,k_x)$$
$$h_y(\mathbf{k}) = 4SDm_k$$
$$h_z(\mathbf{k}) = SJ_2(\lambda - cos\,k_x), \tag{3.9}$$

where $m_k \equiv -sin\,k_x\,cos\,\frac{k_y}{2}$ is a structure factor. All the calculations in this study were made for a lattice with an infinite number of sites with periodic boundary conditions, so the wave vectors $\mathbf{k}$ continuously cover the Brillouin zone ($k_x = [-\pi, \pi]$, $k_y = [-\pi, \pi]$). The explicit dispersion relation is

$$\epsilon_\pm(\mathbf{k}) = SJ_2(\lambda - cos\,k_x) + 2S\lambda(J_1 + 2J_3) + B$$
$$\pm S\sqrt{4\,cos^2\,\frac{k_y}{2}(J_1 + 2J_3\,cos\,k_x)^2 + J_2^2(\lambda - cos\,k_x)^2 + 16D^2 m_k^2}. \tag{3.10}$$
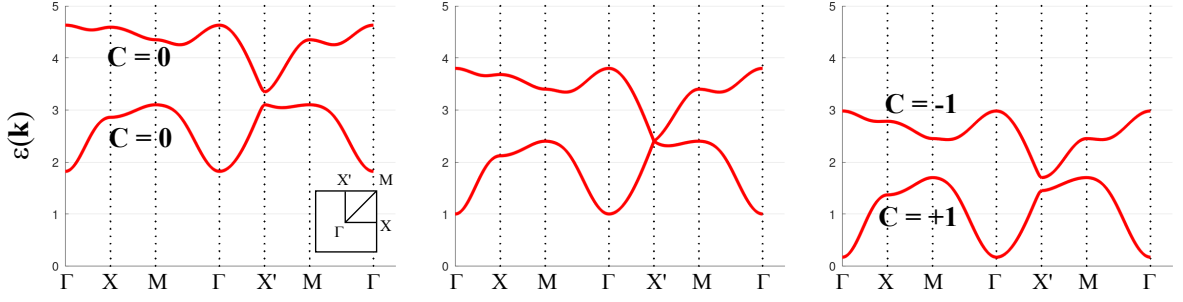
Figure 2 – Band structure of the modified Lieb lattice. The parameters are $S = 1/2$, $B = 1.0$, $J_1 = 1.0$, $J_2 = 0.5$, $J_3 = 0.2$, and $D = 0.1$. There is a topological phase transition from a trivial insulating phase (Chern number $C = 0$), when $\lambda > 1$ ($\lambda = 1.5$ in the left panel) to a topological insulating phase ($C = \pm 1$), when $\lambda < 1$ ($\lambda = 0.5$ in the right panel). In the transition (middle panel, $\lambda = 1$) the gap is closed, the Berry curvature diverges and the Chern number is not defined.
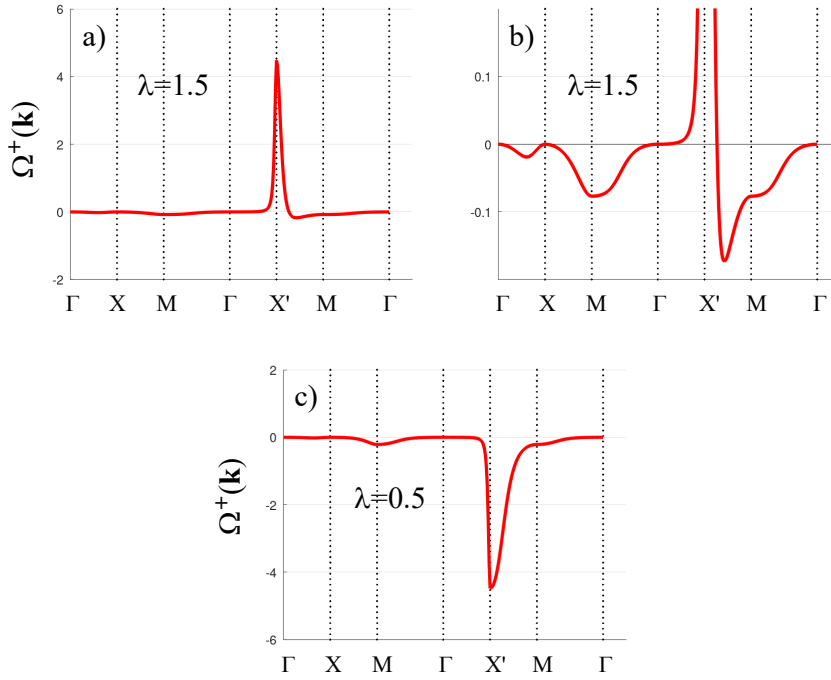
Figure 3 – Berry curvature of the upper band for $S = 1/2$, $B = 1.0$, $J_1 = 1$, $J_2 = 0.5$, $J_3 = 0.2$ and $D = 0.1$. In the trivial phase ((a) and (b), where in (b) the y-axis is stretched around $y = 0$ for better visualization), regions of negative Berry curvature cancel out the positive peak (X' point) in the integral that defines the Chern number. That does not occur in the topological phase (c).

The system's band structure is plotted in Fig. 2. There is a gap of $2SJ_2 |\lambda - 1|$ at the high-symmetry point $X' = (0, \pm\pi)$. The gap vanishes into a Dirac point in the isotropic limit ($\lambda = 1$) independently of the value of other parameters. Therefore, the anisotropy is responsible for the gap. This is in contrast with with other magnon insulating systems,

when the DMI creates the gap [77, 87, 90, 97]. There is a topological phase transition in $\lambda = 1$: for $\lambda > 1$ the system is a trivial magnon insulator ($C^{\pm} = 0$, where the Chern number $C^{\pm}$ is defined in Eq. 2.36), and for $\lambda < 1$, the system is a topological magnon insulator ($C^{\pm} = \mp 1$). In this lattice, the topological phase is problematic, because for $\lambda < 1$ the exchange term is minimized for an in-plane spin configuration, competing with the Zeeman term. Nevertheless, we assume that the Zeeman term is strong enough to assure the off-plane (z direction) ground state.
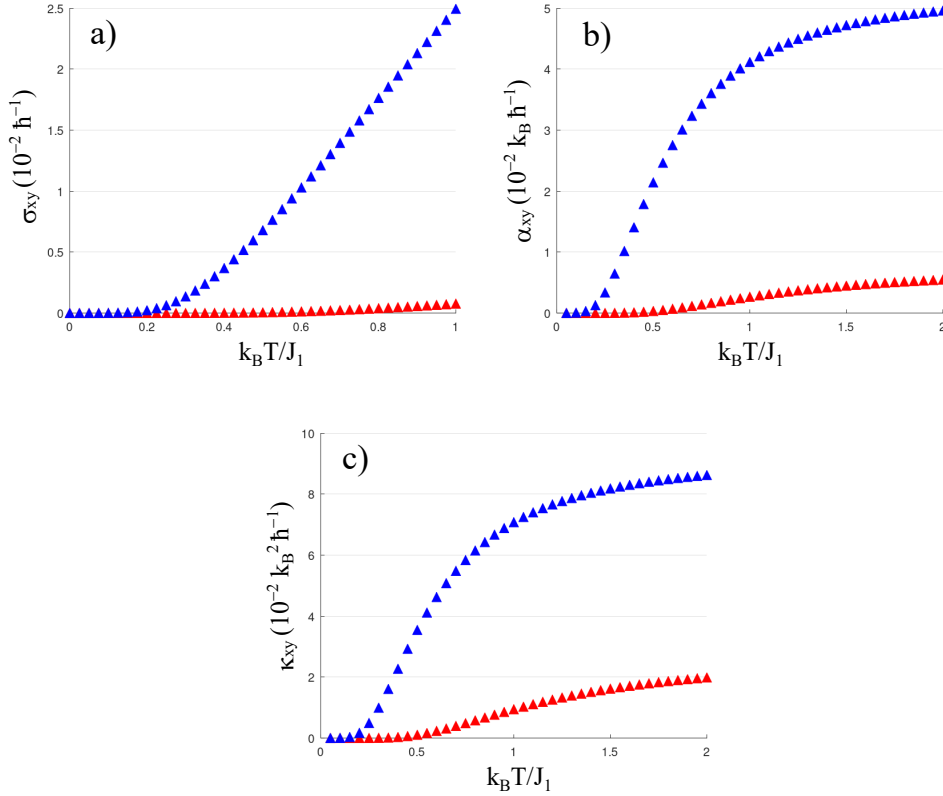
Figure 4 – Transport coefficients in the topological (blue) and trivial (red) phases. The parameters are the same as in Fig. 3.

The Chern number is calculated from the Berry curvature (Eq. 2.36). For a two-band FM system, the Berry curvature of the upper and lower bands have opposite sign and can be written as [15, 77]

$$\Omega_{xy}^{\pm}(\mathbf{k}) = \mp\hat{\mathbf{h}} \cdot \left(\frac{\partial\hat{\mathbf{h}}}{\partial k_x} \times \frac{\partial\hat{\mathbf{h}}}{\partial k_y} \right), \tag{3.11}$$

where $\hat{\mathbf{h}} = \mathbf{h}/h$. The Berry curvatures of the trivial and topological phase are represented in Fig. 3. $\Omega_{xy}^{\pm}$ is peaked around the point in the Brillouin zone where the energy gap vanished when $\lambda = 1$. In the trivial phase, the positive peak is cancelled out

by regions of negative values, so its integral is null. The Berry curvature is itself null when the DMI parameter is $D = 0$.
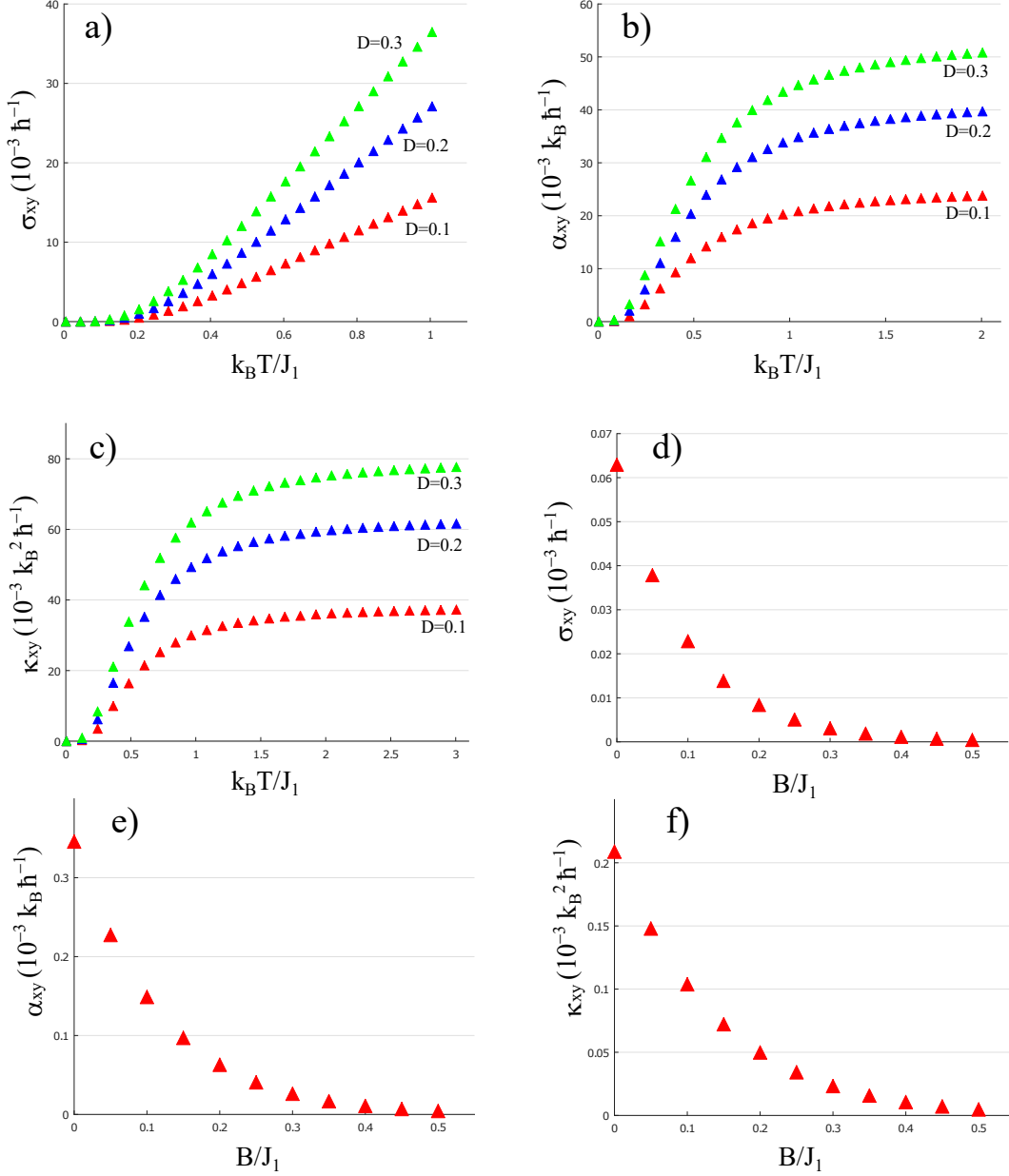
Figure 5 – (a-c) Transport coefficients versus temperature ($S = 1/2$, $B = 0$, $J_1 = 1$, $J_2 = 0.5$, $J_3 = 0$, $\lambda = 1.2$) for different values of D. (d-f) Same coefficients versus applied magnetic field ($S = 1/2$, $T = 0.1$, $J_1 = 1$, $J_2 = 0.5$, $J_3 = 0$, $\lambda = 1.2$, $D = 0.2$).

3.3 Transverse transport coefficients

The transverse transport coefficients defined in Section 2 (spin Hall conductivity σ_{xy}, spin Nernst coefficient α_{xy} and thermal Hall conductivity κ_{xy}, Eqs. (2.40)-(2.42) were calculated numerically for the trivial and topological phases, using several combinations of theory parameters. The first thing to note, in Fig. 4, is that these coefficients are higher in the topological phase. Also, the plots shows a monotonically rising behavior with T, similar to what is observed in several magnetic lattices [76, 79, 80, 86–88]. At zero temperature, the conductivities are zero due to the absence of magnon excitations. That is a consequence of the fact that boson numbers are not conserved and vanish in the zero temperature limit. Magnons are thermally excited as the temperature increases from zero. At low temperatures, the lower band dominates. It can be seen that σ_{xy} rises linearly with T, while α_{xy} and κ_{xy} have asymptotic behavior. That is because $c_1(x)$ and $c_2(x)$ (Eqs. 2.43) decreases with x, leading to the flattening of the curves at high temperatures. In fact, it is possible to calculate analytically the high-T limit, which corroborates the numerical results:

$$\sigma_{xy}(T \to \infty) = -\frac{k_B T}{\hbar^2} \int \frac{d^2k}{(2\pi)^2} \left(\frac{1}{\epsilon_k^+} - \frac{1}{\epsilon_k^-} \right) \Omega_k^+$$

$$\alpha_{xy}(T \to \infty) = \frac{k_B}{\hbar} \int \frac{d^2k}{(2\pi)^2} \left(ln\,\epsilon_k^+ - ln\,\epsilon_k^- \right) \Omega_k^+$$

$$\kappa_{xy}(T \to \infty) = k_B \int \frac{d^2k}{(2\pi)^2} \left(\epsilon_k^+ - \epsilon_k^- \right) \Omega_k^+. \tag{3.12}$$

Fig. 5 shows the transport coefficients' dependence with T (above) and the external magnetic field B (below). The coefficients are intensified for high Dzyaloshinskii-Moriya interaction D. Also, they are suppressed for high magnetic field B. That is explained as follows. The magnetic field does not affect the Berry curvature, but raises both energy bands. For a given T, a smaller number of magnons are excited in both bands, leading to a suppression of σ_{xy}, α_{xy} and κ_{xy}. In an intuitive picture, a high magnetic field inforces the magnetic order, diminishing the density of excited states (magnons).

In Fig. 6, one can see the dependence of the transport coefficients on the relative exchange parameters J_2/J_1 and J_3/J_1. An increase in J_3 leads to a decrease in the coefficients. On the other hand, all coefficients show a peak for a definite J_2/J_1 value. The exact value and peak height depend on the other parameters of the theory.

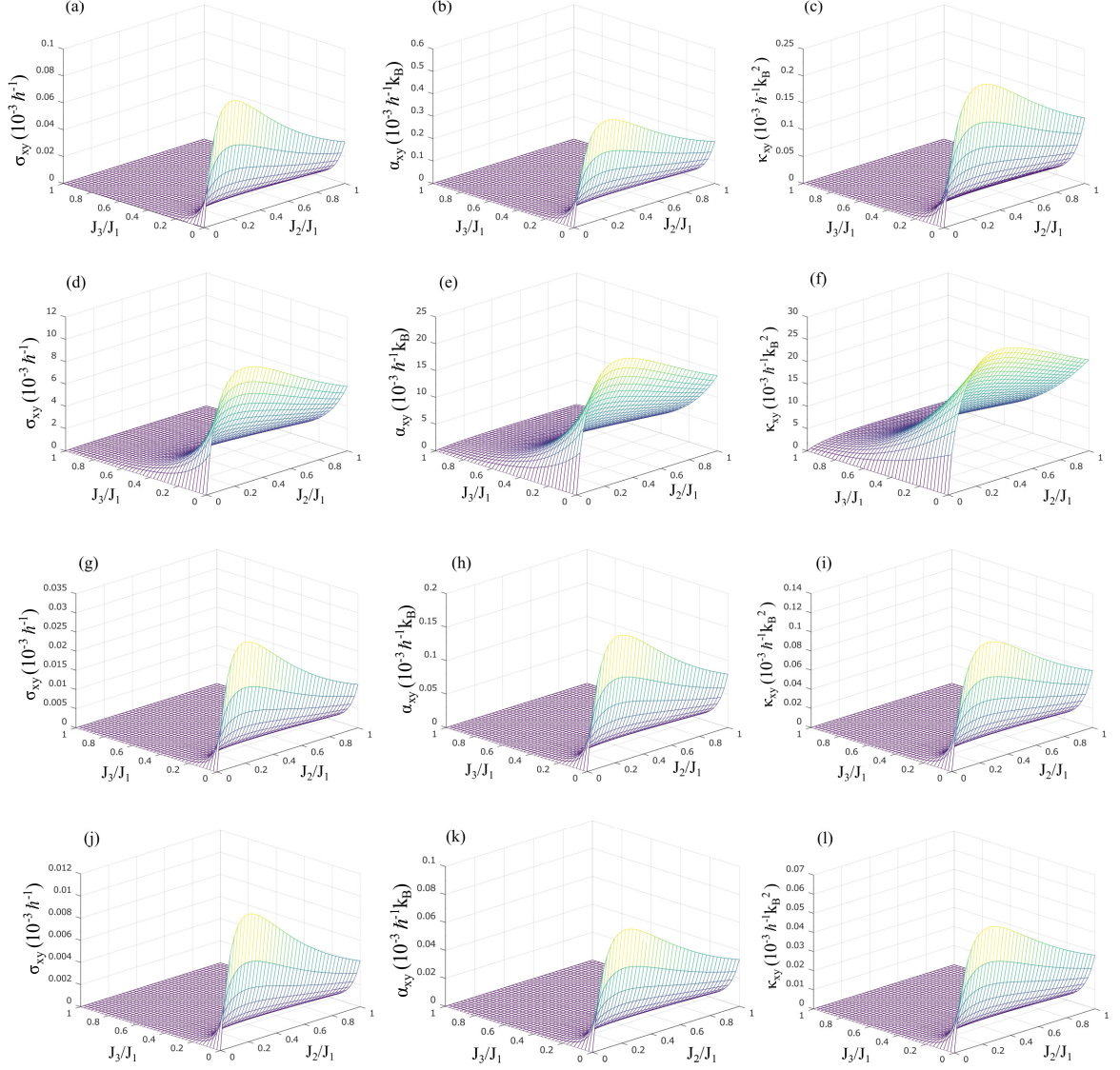Figure 6 – All three transport coefficients as functions of the relative parameters J_2/J_1 and J_3/J_1 for different temperatures and applied magnetic fields: (a)-(c) $B/J_1 = 0$ and $k_BT/J_1 = 0.1$. (d)-(f) $B/J_1 = 0$ and $k_BT/J_1 = 0.5$. (g)-(i) $B/J_1 = 0.1$ and $k_BT/J_1 = 0.1$. (j)-(l) $B/J_1 = 0.2$ and $k_BT/J_1 = 0.1$. The other parameters are $J_1 = 1.0$, $S = 1/2$, $D = 0.1$ and $\lambda = 1.2$.

4 Antiferromagnetic Union Jack lattice

Magnons can mediate Hall-like transport phenomena in both ferromagnets and antiferromagnets. Antiferromagnets exhibit ultrafast dynamics and are robust against reasonably large external fields [98–100]. They are a competitive alternative to ferromagnets to store and manipulate information, as topological ferromagnets present drawbacks such as strong magnetic disturbances and low mobility due to high magnetization. Topological transport in magnets with AFM exchange interaction has been investigated in several contexts, such as in the paramagnetic phase [101], non-collinear and non-coplanar ordering [82, 102, 103] and dimer states [104–106]. In this scenario, it is essential to study antiferromagnetic topological insulators in all kinds of lattices and investigate their thermomagnetic properties.

In this chapter, we investigate the energy bands and transverse transport of magnons in a Néel state antiferromagnet with the geometry of the Union Jack lattice, represented in Fig. 7. This investigation was published in Ref. [107]. The Union Jack lattice is obtained by adding alternate diagonals to the square lattice. The Hamiltonian of the model is:

$$
\begin{aligned}
H = & J_1 \sum_{\langle i,j \rangle} \mathbf{S}_i \cdot \mathbf{S}_j + \sum_{\langle\langle i,j \rangle\rangle \in A} J_{2,ij} \left(\mathbf{S}_i \cdot \mathbf{S}_j + (\lambda - 1) S_i^z S_{i'}^z \right) \\
& + D \sum_{\langle i,j \rangle} \nu_{ij} \hat{\mathbf{z}} \cdot \mathbf{S}_i \times \mathbf{S}_j - A \sum_i \left(S_i^z \right)^2 .
\end{aligned}
\tag{4.1}
$$

The lattice is divided into A and B sublattices. The NNN exchange interaction carries two kinds of anisotropy: an off-plane $\lambda > 1$ anisotropy (like in the case of the modified Lieb lattice) which favors the alignment of the spins in the z direction; and an in-plane anisotropy in the form of different exchange constants $J_{2,ij}$ for different in-plane directions (x and y). From now on we define $J_2 \equiv J_{2,x}$ and $\alpha J_2 \equiv J_{2,y}$, and the system is plane-isotropic when $\alpha = 1$. The third term of the Hamiltonian is the spin-orbit induced Dzyaloshinskii-Moriya interaction between NN sites A and B. The last term is a single ion easy-axis anisotropy (SIA) which favors spin alignment in the z direction.

From the Hamiltonian above, we are able to find the magnon energy bands (in the linear spin wave regime) and Berry curvature, and from those calculate the transverse transport coefficients. In order do preserve the bosonic commutation relations, the diagonalization of the bosonic antiferromagnetic Hamiltonian requires a different treatment than the FM case, which is presented below.
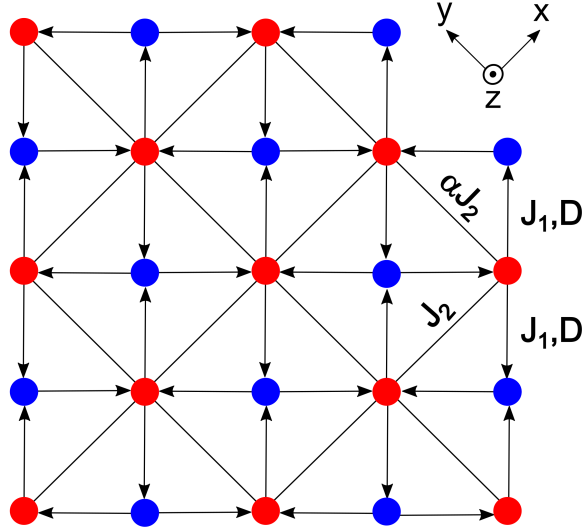
Figure 7 – The Union Jack lattice in the Néel state. The red sites are sublattice A, with spins pointing in the $+z$ direction. The blue sites are sublattice B, $-z$ direction. J_1 and J_2 are exchange interactions, while α is an in-plane anisotropy. D is a Dzyaloshinskii-Moriya interaction, with $\nu_{ij} = +1$ along the arrows, and -1 against them.

4.1   Antiferromagnetic magnons - formalism

For the analysis of the bosonic antiferromagnetic Hamiltonian, some ordered ground state needs to be established, which is chosen to be the off-plane Néel state. The system has two inequivalent sites, so the lattice is broken in two sublattices, A and B. This procedure is similar to what was done in the ferromagnetic modified Lieb lattice in the previous chapter, but with the crucial difference that each sublattice has internal ferromagnetic order with opposite spin orientation. We take the Néel order perpendicular to the lattice plane, i. e., spins on the A and B sublattices satisfy $\mathbf{S}_A = -\mathbf{S}_B = S\hat{z}$ in the ground state. Like in the FM case, we take the Holstein-Primakoff transformation, which for AFM systems in the Néel order is [95, 108]:

$$S_i^+ = \sqrt{2S}\sqrt{1 - \frac{a_i^\dagger a_i}{2S}}\, a_i, \qquad S_i^- = \sqrt{2S}\, a_i^\dagger \sqrt{1 - \frac{a_i^\dagger a_i}{2S}}, \qquad S_i^z = S - a_i^\dagger a_i, \qquad i \in A$$

$$S_i^+ = \sqrt{2S}\, b_i^\dagger \sqrt{1 - \frac{b_i^\dagger b_i}{2S}}, \qquad S_i^- = \sqrt{2S}\sqrt{1 - \frac{b_i^\dagger b_i}{2S}}\, b_i, \qquad S_i^z = -S + b_i^\dagger b_i, \qquad i \in B.$$

$$(4.2)$$

The AFM Holstein-Primakoff transformation is different from its FM counterpart in order to preserve the commutation relations between different spin operators. In the

linear spin wave regime, the square roots are expanded to zeroth order:

$$S_i^+ = \sqrt{2S}\, a_i, \qquad S_i^- = \sqrt{2S}\, a_i^\dagger, \qquad S_i^z = S - a_i^\dagger a_i, \qquad i \in A$$
$$S_i^+ = \sqrt{2S}\, b_i^\dagger, \qquad S_i^- = \sqrt{2S}\, b_i, \qquad S_i^z = -S + b_i^\dagger b_i, \qquad i \in B. \tag{4.3}$$

After Fourier transforming, we ignore terms with order higher than two (anharmonic terms) in the magnon operators, assuming a free-boson, linear spin wave regime. It is possible to write the Hamiltonian as

$$H = \sum_k \psi_k^\dagger H_k \psi_k \tag{4.4}$$

with

$$\psi_k^\dagger = \left(a_{1,k}^\dagger, ..., a_{N,k}^\dagger, a_{1,-k}, ..., a_{N,-k} \right), \tag{4.5}$$

where the system is generalized from two to N sublattices. We note that terms of the form $a_{1,k}^\dagger a_{2,-k}^\dagger$ appear naturally with the application of Eq. (4.3) to the Hamiltonian (4.1). So a Nambu spinor (4.5) must be used, and the Hilbert space is doubled: the Hamiltonian matrix H_k has dimension $2N$, and satisfies the bosonic particle-hole symmetry [28]:

$$H_k = \rho H_{-k}^T \rho, \qquad \rho = \begin{pmatrix} 0 & I_N \\ I_N & 0 \end{pmatrix}, \tag{4.6}$$

where I_N is the identity matrix. To diagonalize the Hamiltonian H_k and find the magnon spectrum, we must perform a *generalized Bogoliubov transformation* from $a_{nk}^{(\dagger)}$ to $\alpha_{nk}^{(\dagger)}$. That procedure is general and do not require a specific lattice order or number of inequivalent sites [109, 110]. We find a transformation matrix T_k from the old basis to a new basis, $\psi_k = T_k \varphi_k$. Let $\alpha_{nk}^{(\dagger)}$ be the magnon creation and annihilation operators:

$$\varphi_k^\dagger = \left(\alpha_{1,k}^\dagger, ..., \alpha_{N,k}^\dagger, \alpha_{1,-k}, ..., \alpha_{N,-k} \right). \tag{4.7}$$

After the transformation, the components of φ_k must satisfy the same bosonic commutation relation as ψ_k:

$$\left[\varphi_{ik}, \varphi_{jk}^\dagger \right] = \left[\psi_{ik}, \psi_{jk}^\dagger \right] = \eta_{ij}, \tag{4.8}$$

where η is a "metric matrix":

$$\eta = \begin{pmatrix} I_N & 0 \\ 0 & -I_N \end{pmatrix}. \tag{4.9}$$

The matrix T_k is such that the Hamiltonian can be written as

$$H = \sum_k \left(T_k \varphi_k \right)^\dagger H_k \left(T_k \varphi_k \right) = \sum_k \varphi_k^\dagger \tilde{H}_k \varphi_k, \tag{4.10}$$

where $\tilde{H}_k$ is diagonal: $\tilde{H}_k = T_k^\dagger H_k T_k = diag\left(\epsilon_1, \epsilon_2, ..., \epsilon_n, \epsilon_1, \epsilon_2, ... \epsilon_n\right)$. To ensure that the new operators α_{nk} satisfy the bosonic algebra, the matrix T_k must fulfil the condition

$$T_k^\dagger = \eta T_k^{-1} \eta^{-1}. \tag{4.11}$$

A matrix T_k satisfying condition above is called as pseudo-unitary (or para-unitary) [111]. The eigenvalues of H_k are obtained indirectly by the diagonalization of $K_k \equiv \eta H_k$. The operator K_k is not Hermitian, but satisfy the property

$$K_k^\dagger = \eta K_k \eta^{-1}, \tag{4.12}$$

being called pseudo-Hermitian and having real eigenvalues [112, 113]: its diagonalization leads to $\tilde{K}_k = diag\left(\epsilon_1, \epsilon_2, ..., \epsilon_n, -\epsilon_1, -\epsilon_2, ... - \epsilon_n\right)$. Its right eigenvectors $v_i\left(\mathbf{k}\right)$ are the columns of the pseudo-unitary matrix T_k. Therefore, when diagonalizing K_k we obtain the eigenvalues and the T_k matrix automatically. The eigenvectors are orthogonal and normalized as:

$$v_i^\dagger\left(\mathbf{k}\right) \eta v_j\left(\mathbf{k}\right) = \pm 1, \tag{4.13}$$

where $+1$ is used for particle states and -1 for hole states. The inner product is modified by the pseudo-Hermiticity: $\langle a | b \rangle \equiv a^\dagger \eta b$.

The procedure shown above establishes a specific order for the $a_i^\dagger$ operators in $\psi_k^\dagger$ (see Eq. 4.5). Nevertheless, sometimes it is convenient to establish a different order. The matrix η is most generically $\eta = diag\left(\sigma_1, \sigma_2, ..., \sigma_{2N}\right)$, with $\sigma_i = +1$ if the correspondent operator in $\psi_k^\dagger$ is $b_k^\dagger$, and $\sigma_i = -1$ if it is b_{-k}. That shuffles the particle/hole eigenvectors in T_k, but it can be useful if the corresponding matrix H_k is block-diagonal in this basis.

At this point we retrieve the restriction that the system is a two band magnon system, and choose a specific order for the vectors $\psi_k^\dagger$ and $\varphi_k^\dagger$:

$$\psi_k^\dagger = \left(\begin{array}{cccc} a_k^\dagger & b_{-k} & a_{-k} & b_k^\dagger \end{array}\right)$$
$$\varphi_k^\dagger = \left(\begin{array}{cccc} \alpha_k^\dagger & \beta_{-k} & \alpha_{-k} & \beta_k^\dagger \end{array}\right). \tag{4.14}$$

For this choice of basis, the metric matrix is $\eta = diag(1, -1, -1, 1)$.

The most general form of a bosonic 4x4 Hamiltonian with particle-hole symmetry is known as the *bosonic Bogoliubov-de Gennes* (BdG) Hamiltonian and is written as [109]:

$$H_{BdG} = \left(\begin{array}{cc} M_k & \xi_k \\ \xi_{-k}^* & M_{-k}^* \end{array}\right), \tag{4.15}$$

where M_k and ξ_k are 2x2 matrices. In the Union Jack lattice, the basis in Eq. 4.14 leads to a representation where $\xi_k = 0$, so the Hamiltonian is block diagonal and M_k can be written as

$$M_k = \left(\begin{array}{cc} r_1 & f^* \\ f & r_2 \end{array}\right) = h_0 I + h_x \sigma_x + h_y \sigma_y + h_z \sigma_z. \tag{4.16}$$

We will assume that $M_k = M_{-k}$, which is a result obtained for the AFM Union Jack lattice. The advantage of working with a block-diagonal Hamiltonian is evident when K_k is written as (by block multiplication):

$$K_k = \eta H_k = \begin{pmatrix} \sigma_z M_k & 0 \\ 0 & -\sigma_z M_k \end{pmatrix}. \tag{4.17}$$

Hence, the sectors of K_k can be diagonalized separately. The first block, which is called α sector, has eigenvectors

$$\varphi_\alpha^+ = \begin{pmatrix} u^* \\ -v^* \end{pmatrix}, \qquad \varphi_\alpha^- = \begin{pmatrix} -v \\ u \end{pmatrix}, \tag{4.18}$$

with functions u and v are defined as

$$u \equiv \frac{f}{|f|} \left(\frac{r+w}{2w} \right)^{1/2}, \qquad v \equiv \left(\frac{r-w}{2w} \right)^{1/2}. \tag{4.19}$$

The corresponding eigenvalues are

$$\epsilon_\alpha^+ = \Delta + w, \qquad \epsilon_\alpha^- = \Delta - w, \tag{4.20}$$

with

$$r \equiv \frac{r_1 + r_2}{2}, \quad \Delta \equiv \frac{r_1 - r_2}{2}, \quad w \equiv \sqrt{r^2 - |f|^2}, \quad f \equiv h_x + i h_y. \tag{4.21}$$

The eigenvectors of the β sector (second block of H_k) are the complex conjugate of the α sector with a change of sign for the eigenvalues, so the eigenvalues of K_k show up in pairs $\pm \epsilon$. As the bosonic Bogoliubov transformation duplicates the Hilbert space, we have redundant solutions, so only the φ_α^+ and φ_β^+ solutions are kept [114], which correspond to the the particle states. The matrix T_k, which diagonalizes K_k and carries all four eigenvectors is, then:

$$T_k = \begin{pmatrix} T_\alpha & 0 \\ 0 & T_\beta \end{pmatrix} = \begin{pmatrix} u^* & -v & 0 & 0 \\ -v^* & u & 0 & 0 \\ 0 & 0 & u & -v^* \\ 0 & 0 & -v & u^* \end{pmatrix} = \left(\varphi_\alpha^+, \varphi_\alpha^-, \varphi_\beta^-, \varphi_\beta^+ \right). \tag{4.22}$$

The diagonalized $\tilde{K}_k$, which carries the eigenvalues, is:

$$\tilde{K}_k = \begin{pmatrix} \epsilon_\alpha & 0 & 0 & 0 \\ 0 & -\epsilon_\beta & 0 & 0 \\ 0 & 0 & -\epsilon_\alpha & 0 \\ 0 & 0 & 0 & \epsilon_\beta \end{pmatrix}. \tag{4.23}$$

The particle states correspond to the first and fourth column of T_k. The physical eigenvalues are:

$$\epsilon_{\alpha,\beta}\left(\mathbf{k}\right) = w\left(\mathbf{k}\right) \pm \Delta\left(\mathbf{k}\right).\tag{4.24}$$

We can show that [115]

$$S^z = \sum_{i\in A}\sum_{j\in B}\left(S_i^z + S_j^z\right) = \sum_k\left(-\alpha_k^\dagger\alpha_k + \beta_k^\dagger\beta_k\right).\tag{4.25}$$

Hence $\langle 0|\,\alpha_k S^z \alpha_k^\dagger\,|0\rangle = -1$ and $\langle 0|\,\beta_k S^z \beta_k^\dagger\,|0\rangle = +1$, where$|0\rangle$ is the magnon vacuum. This means that α magnons carry spin -1 and β magnons carry spin $+1$ (along the z direction).
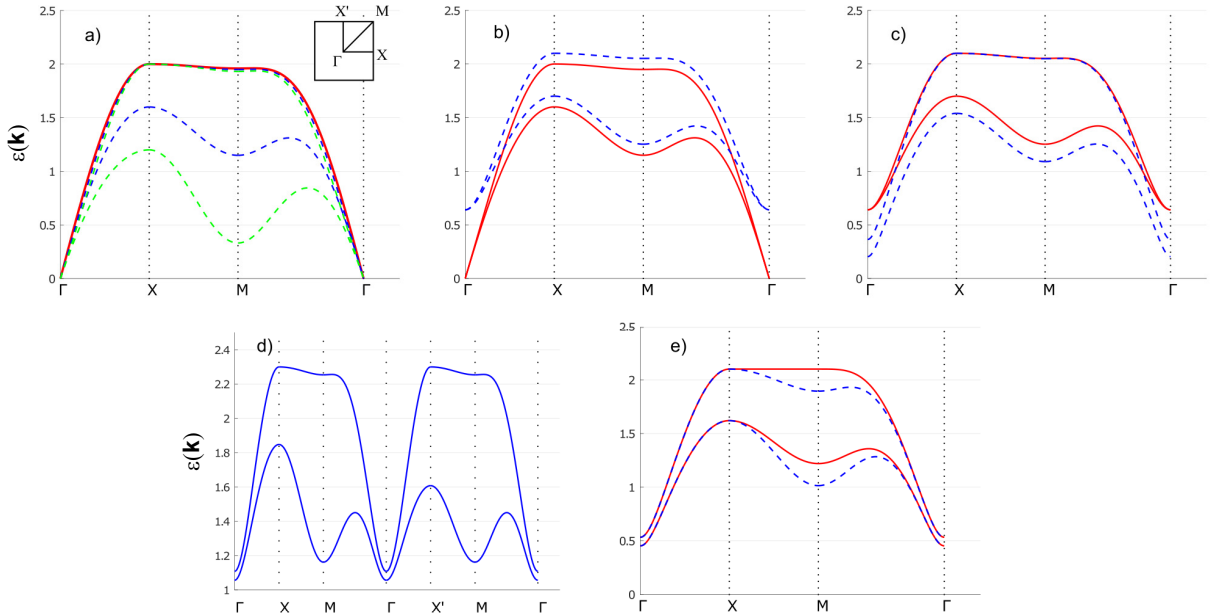
Figure 8 – Magnon energy bands of the antiferromagnetic Union Jack lattice. (a) $S = J_1 = \lambda = \alpha = 1.0$, $A = 0$, $D = 0.2$ and three values of J_2: 0 (solid red, both bands are totally degenerate), 0.2 (dashed blue) and 0.4 (dashed green). (b) $S = J_1 = \lambda = \alpha = 1.0$, $J_2 = D = 0.2$ and two values of single-ion anisotropy: $A = 0$ (solid red) and $A = 0.2$ (dashed blue). (c) $S = J_1 = \alpha = 1.0$, $J_2 = A = D = 0.2$ and two values of off-plane exchange anisotropy: $\lambda = 1$ (solid red) and $\lambda = 1.4.$ (dashed blue). (d) $S = J_1 = 1.0$, $J_2 = D = 0.2$, $A = 0.6$, $\lambda = 1.1$, $\alpha = 1.6$. (e) $S = J_1 = \alpha = 1.0$, $J_2 = A = 0.2$, $\lambda = 1.2$ and two values of Dzyaloshinskii-Moriya interaction: $D = 0$ (solid red) and $D = 0.4$.

4.2 Magnon bands

After performing the linear Holstein-Primakoff transformation and following the formalism described above, the Hamiltonian 4.26, a bosonic Bogoliubov-de Gennes Hamiltonian is obtained (in this specific case, a block-diagonal matrix):

$$H_k = \begin{pmatrix} M_k & 0 \\ 0 & M_{-k}^* \end{pmatrix}, \qquad M_k = rI + \Delta\sigma_z + h_x\sigma_x + h_y\sigma_y, \tag{4.26}$$

with

$$r = 2SJ_1 + A\left(\frac{2S-1}{2}\right) + SJ_2\left(\eta_k - \lambda\frac{\alpha+1}{2}\right)$$
$$\Delta = SJ_2\left(\eta_k - \lambda\frac{\alpha+1}{2}\right)$$
$$h_x = 2SJ_1\gamma_k$$
$$h_y = 2SDm_k. \tag{4.27}$$

The structure factors are

$$\gamma_k = \cos\frac{k_x}{2}\cos\frac{k_y}{2}, \qquad \eta_k = \frac{1}{2}\left(\cos k_x + \alpha\,\cos k_y\right), \qquad m_k = -\sin\frac{k_x}{2}\sin\frac{k_y}{2}. \tag{4.28}$$

Those are even functions of $\mathbf{k}$. Hence, $M_k = M_{-k}$. The diagonalization of H_k gives the antiferromagnetic band structure from Eq. 4.24 (see also the definitions Eqs. 4.21)

$$\epsilon_{\alpha,\beta}\left(\mathbf{k}\right) = w\left(\mathbf{k}\right) \pm \Delta\left(\mathbf{k}\right). \tag{4.29}$$

If $J_2 = 0$ the term $\Delta\left(\mathbf{k}\right)$ vanishes, the magnon bands are totally degenerate and the system is reduced to the AFM square lattice [20]. Higher values of J_2 lower the β band, while the α band remains almost unchanged (Fig. 8a). For small enough values of J_2/J_1, A/J_1 and D/J_1, both bands have a minimum at $k_x = k_y = 0$ (point Γ). The single-ion anisotropy A makes the minimum value non-zero (Fig. 8b). In Fig. 8c, one can see how the exchange anisotropy $\lambda > 1$ splits the bands at point Γ.

The effect of the in-plane anisotropy α is to create an energetic inequivalence between points X and X' in the Brillouin zone (Fig. 8d). That energetic imbalance is necessary for transverse transport effects. We also note that the DMI itself does not open a gap, but changes the character of the dispersion by lowering the energy at the point M (Fig. 8e).

4.3   Modified spin waves

All results above apply to free bosons, in the linear spin wave regime (LSW). It is possible to include the lowest order anharmonic contributions of the Hamiltonian via a mean-field treatment that we call here *modified spin wave* (MSW) approach. Expanding

the square root in the HP transformations (Eq 4.3) up to first order, we get:

$$S_i^+ = \sqrt{2S}\left(a_i - \frac{a_i^\dagger a_i a_i}{4S}\right), \qquad S_i^- = \sqrt{2S}\left(a_i^\dagger - \frac{a_i^\dagger a_i^\dagger a_i}{4S}\right), \qquad S_i^z = S - a_i^\dagger a_i, \qquad i \in A$$

$$S_i^+ = \sqrt{2S}\left(b_i^\dagger - \frac{b_i^\dagger b_i^\dagger b_i}{4S}\right), \qquad S_i^- = \sqrt{2S}\left(b_i - \frac{b_i^\dagger b_i b_i}{4S}\right), \qquad S_i^z = -S + b_i^\dagger b_i, \qquad i \in B.$$

$$(4.30)$$

One must apply the transformation above to the Hamiltonian and ignore the terms of order higher than four on the operators, which would represent interaction between more than two magnons, and have a lower contribution to the perturbative series. The harmonic (quadratic) terms reproduce the LSW results. The terms of fourth order represent interaction between two magnons. Those terms are rewritten using a mean-field approach:

$$ABCD \approx \langle AB\rangle\, CD + \langle CD\rangle\, AB + \langle AC\rangle\, BD + \langle BD\rangle\, AC + \langle AD\rangle\, BC + \langle BC\rangle\, AD.$$

$$(4.31)$$

where A, B, C and D can be $a_i^{(\dagger)}$ or $b_{i'}^{(\dagger)}$, and $\langle ...\rangle$ are thermal averages, which we call *MSW coefficients* Γ_j. This procedures decouples the magnons, generating an effective harmonic Hamiltonian. The MSW coefficients are ultimately written in terms of the magnon occupation numbers $\left\langle \alpha_k^\dagger \alpha_k \right\rangle$ and $\left\langle \beta_k^\dagger \beta_k \right\rangle$, which are defined thermodynamically as the thermal population (Bose-Einstein distribution $n_k^{\alpha,\beta}(T)$):

$$\Gamma_j = \Gamma_j\left(n_k^\alpha(T), n_k^\beta(T)\right). \tag{4.32}$$

The effective Hamiltonian (and energy bands) is renormalized by the mean-field coefficients $\Gamma_j(T)$ and is implicitly temperature-dependent. For each temperature, the coefficients are found with a numerical self-consistent calculation which follows the algorithm in Fig. 9.
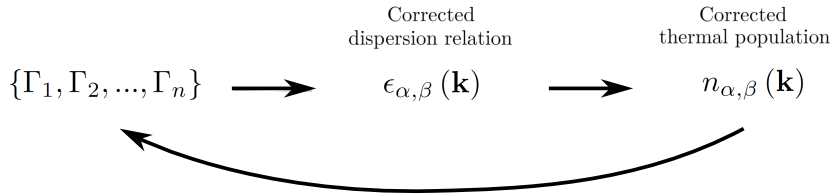

Figure 9 – Algorithm for the self-consistent calculation of the MSW coefficients.

As long as the numerical result of the self-consistent algorithm converges, one can find the lowest order correction to linear spin waves by finding the temperature-dependent coefficients $\Gamma_j(T)$ and solving the effective Hamiltonian for each temperature.
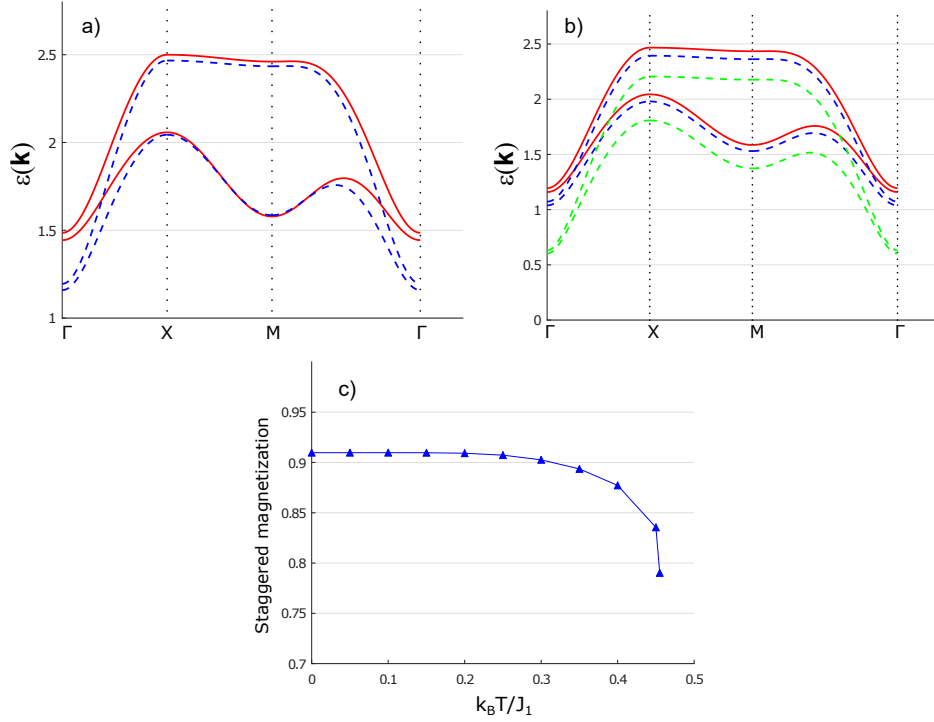
Figure 10 – Effect of the modified spin wave (MSW) approach in the AFM Union Jack lattice. The parameters are $S = J_1 = A = 1.0$, $J_2 = D = 0.2$, $\lambda = \alpha = 1.1$. (a) Linear spin wave dispersion relation (LSW, solid red line) compared to the MSW case (dashed blue line) for zero temperature. (b) MSW dispersion for $k_B T = 0$ (solid red), $k_B T = 0.4$ (dashed blue) and $k_B T = 0.456$ (dashed green). The energy at Γ-point falls abruptly to zero as we approach the transition temperature $k_B T_N \approx 0.456$. (c) Staggered magnetization, signalling a phase transition at T_N.

When this procedure is applied in the AFM Union Jack lattice, a total of 7 MSW coefficients is found. A complete description and the results of the MSW approach for the Union Jack lattice can be found in Appendix A. The energy bands are modified as shown in Fig. 10. Even at zero temperature, the anharmonic contributions affect the dispersion, lowering the bands' minimum energy (Fig. 10a). As the temperature rises, the bands remain almost unchanged until we get close to a definite temperature T_N, when the bands lower abruptly (Fig. 10b). T_N is interpreted as the Néel temperature that signals a phase transition. At that temperature, the Néel order is unstable: the lower band reaches zero energy at point Γ and the staggered magnetization vanishes (Fig. 10c). The temperature T_N tends to be higher for high values os A or S.
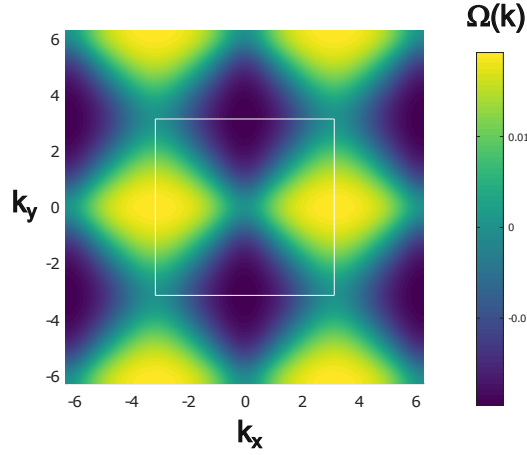
Figure 11 – Berry curvature of the antiferromagnetic Union Jack lattice in the linear spin wave regime. Both bands have the same Berry curvature. The parameters are $S = J_1 = A = 1.0$, $J_2 = D = 0.2$, $\lambda = \alpha = 1.1$.

4.4 Transverse transport coefficients

The Berry curvature of a system described by a two-band block diagonal Bogoliubov-de Gennes Hamiltonian has the form (see Appendix B):

$$\Omega_\alpha \left(\mathbf{k} \right) = -\frac{1}{2} sinh \, \theta_k \left(\frac{\partial \phi_k}{\partial k_x} \frac{\partial \theta_k}{\partial k_y} - \frac{\partial \phi_k}{\partial k_y} \frac{\partial \theta_k}{\partial k_x} \right)$$
$$\Omega_\beta \left(\mathbf{k} \right) = -\frac{1}{2} sinh \, \theta_{-k} \left(\frac{\partial \phi_{-k}}{\partial k_x} \frac{\partial \theta_{-k}}{\partial k_y} - \frac{\partial \phi_{-k}}{\partial k_y} \frac{\partial \theta_{-k}}{\partial k_x} \right) \tag{4.33}$$

where θ_k and ϕ_k are defined as

$$tan \, \phi_k = \frac{h_y}{h_x}, \qquad cosh \, \theta_k = \frac{r}{w}. \tag{4.34}$$

Expression (4.33) can be applied for both LSW or MSW regime, since in the MSW regime all the parameters (including θ_k and ϕ_k) are still defined, although renormalized. There is a fundamental relation between the Berry curvatures of both bands: $\Omega_\alpha \left(\mathbf{k} \right) = \Omega_\beta \left(-\mathbf{k} \right)$. In the AFM Union Jack lattice in the LSW regime, those are even functions: $\Omega_i \left(\mathbf{k} \right) = \Omega_i \left(-\mathbf{k} \right)$. Those two properties result in identical Berry curvatures ($\Omega_\alpha \left(\mathbf{k} \right) = \Omega_\beta \left(\mathbf{k} \right)$), represented in Fig. 11. The Berry curvature is not well-behaved in zero-energy states, so we need $A \neq 0$ and $S \neq 1/2$. In Appendix B, it is shown that an imaginary term in the Hamiltonian ($h_y \neq 0$) is necessary for the Berry curvature to be non-zero. In the Union Jack case, that means D must be non-zero, so the Dzyaloshinskii-Moriya interaction is the responsible for the non-null Berry curvature. The Chern number is proportional to the integral of the Berry curvature over the Brilloiun zone. In this case it is null, as it can be seen from the Berry curvature's symmetry. Hence, the system has trivial Chern
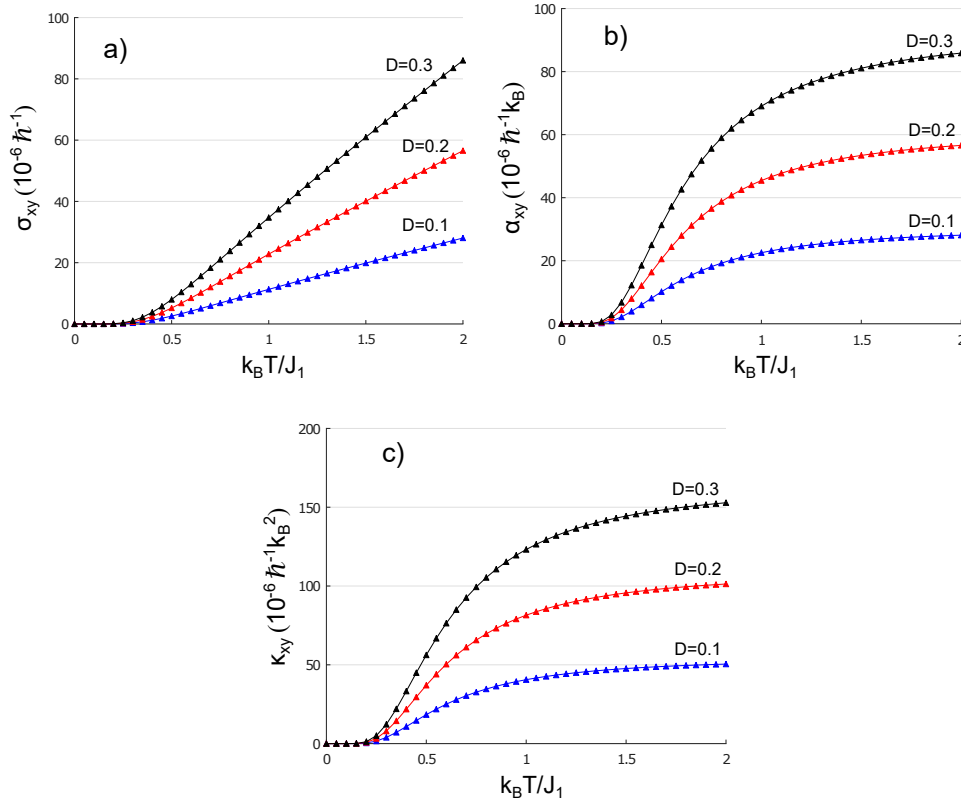
Figure 12 – Transport coefficients of the antiferromagnetic Union Jack lattice. $S = J_1 = A = 1.0$, $J_2 = 0.2$, $\lambda = \alpha = 1.1$.

topology. That happens for every combination of Hamiltonian parameters, both in the LSW and MSW regimes.

The transport coefficients for a two-band antiferromagnet in the Néel state are given by [32, 73, 116]:

$$\sigma_{xy} = -\frac{1}{\hbar} \int \frac{d^2 k}{(2\pi)^2} \left[n_k^\alpha \, \Omega_k^\alpha + n_k^\beta \, \Omega_k^\beta \right]$$

$$\alpha_{xy} = -\frac{k_B}{\hbar} \int \frac{d^2 k}{(2\pi)^2} \left[c_1 \left(n_k^\alpha \right) \Omega_k^\alpha - c_1 (n_k^\beta) \Omega_k^\beta \right]$$

$$\kappa_{xy} = -\frac{k_B^2 T}{\hbar} \int \frac{d^2 k}{(2\pi)^2} \left[c_2 \left(n_k^\alpha \right) \Omega_k^\alpha + c_2(n_k^\beta) \Omega_k^\beta \right], \tag{4.35}$$

where $c_i(x)$ are the functions defined in Eqs. (2.43), and $n_k^{\alpha,\beta}$ are the Bose-Einstein distributions (thermal population) of each band. Non-null Berry curvature is a necessary (but not sufficient) condition for non-null transport coefficients. Another necessary condition is that the system has in-plane anisotropy $\alpha \neq 1$, which generates an energetic imbalance between bands (see Fig. 8d), and the integrals above are non-null.

The numerical results for the transport coefficients are shown in Fig. 12. As usual,
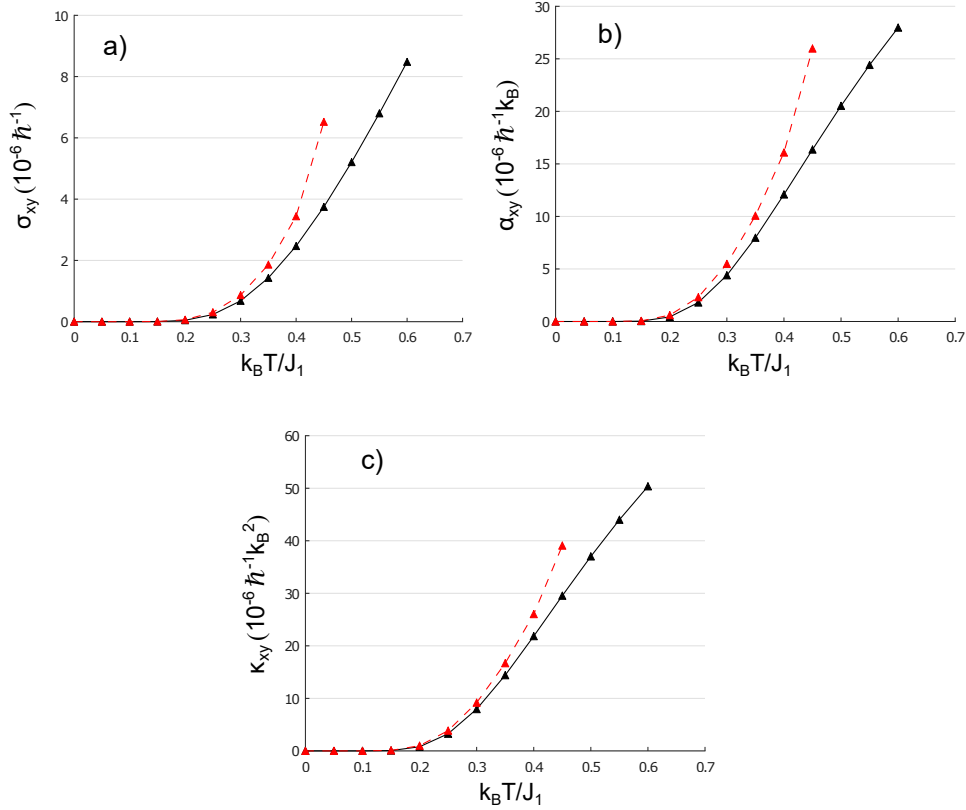
Figure 13 – Effect of the modified spin wave (MSW) approach in the antiferromagnetic Union Jack lattice transport coefficients. The black curve is the linear spin waves, while the dashed red curve is the MSWs. The theory parameters are $S = J_1 = A = 1.0$, $J_2 = D = 0.2$, $\lambda = \alpha = 1.1$.

all transport coefficients increase with D. The effect of the off-plane exchange anisotropy λ is only quantitative: transverse transport exists even when $\lambda = 1$. Also, we can see that the high-temperature behavior of the coefficients is in accordance to the analytical results:

$$\sigma_{xy}(T \to \infty) = -\frac{k_B T}{\hbar^2} \int \frac{d^2 k}{(2\pi)^2} \left(\frac{1}{\epsilon_k^\alpha} \pm \frac{1}{\epsilon_k^\beta} \right) \Omega_k^\alpha$$

$$\alpha_{xy}(T \to \infty) = \frac{k_B}{\hbar} \int \frac{d^2 k}{(2\pi)^2} \left(ln\, \epsilon_k^\alpha \mp ln\, \epsilon_k^\beta \right) \Omega_k^\alpha$$

$$\kappa_{xy}(T \to \infty) = k_B \int \frac{d^2 k}{(2\pi)^2} \left(\epsilon_k^\alpha \pm \epsilon_k^\beta \right) \Omega_k^\alpha. \tag{4.36}$$

The coefficients α_{xy} and κ_{xy} have asymptotic behavior, while σ_{xy} is linear with T. This is similar to 3.12, but adapted to the AFM case where magnons have opposite spins and respond differently to perturbation. Inside the integrand, the upper sign is used when

$\Omega_k^\alpha = \Omega_k^\beta$ (as it is the case of the AFM Union Jack lattice here), and the lower sign is used when $\Omega_k^\alpha = -\Omega_k^\beta$.

We also consider the effect of anharmonic contributions using the modified spin wave approach. In the linear spin wave treatment, the temperature dependence of the transport coefficients comes only from the Bose–Einstein distribution $n_k^{\alpha,\beta}$. The energy bands and Berry curvature are independent of temperature (as it is the Hamiltonian). In the self-consistent MSW theory, we partly include the effects of finite T in the Hamiltonian bands with a mean-field approach. The corrections make the energy dispersion and Berry curvature temperature-dependent, correcting the transport coefficients for each temperature. In Fig. 13 we present the results for MSW. The self-consistent corrections lower the energy bands (see Fig. 10), raising the magnon population for a given temperature and increasing all transport coefficients. That happens until we reach a temperature T_N ($k_B T_N/J_1 \approx 0.456$ for the chosen parameters), where no self-consistent solution is found (the solution does not converge).

5 Antiferromagnetic brick-wall lattice

In the Union Jack lattice shown in the last chapter, both spin Nernst and thermal Hall coefficients are non-null: spin transport is followed by a net magnon transport (heat current). In some systems, (effective) time-reversal symmetry results in spin transport without net magnon transport, which can be seen as magnonic equivalent of the QSHE. That phenomenon happens in the AFM brickwall lattice, which is presented in this chapter and published in Ref. [107]. In this geometry, consider the following Hamiltonian:

$$H = J_1 \sum_{\langle i,j \rangle} \mathbf{S}_i \cdot \mathbf{S}_j + J_2 \sum_{\langle i,j \rangle} \mathbf{S}_i \cdot \mathbf{S}_j + D \sum_{\langle\langle i,j \rangle\rangle} \nu_{ij} \hat{\mathbf{z}} \cdot \mathbf{S}_i \times \mathbf{S}_j - A_1 \sum_{i \in A} \left(S_i^z \right)^2 - A_2 \sum_{i \in B} \left(S_i^z \right)^2 . \quad (5.1)$$

There are exchange interactions J_1 and J_2 between sites A (red sites) and B (blue sites) in a "wall of bricks" pattern, as seen in Fig. 14. The arrows show the Dzyaloshinskii–Moriya interaction between sites AA and BB. The model is extended to account for different on-site anisotropies A_1 and A_2.
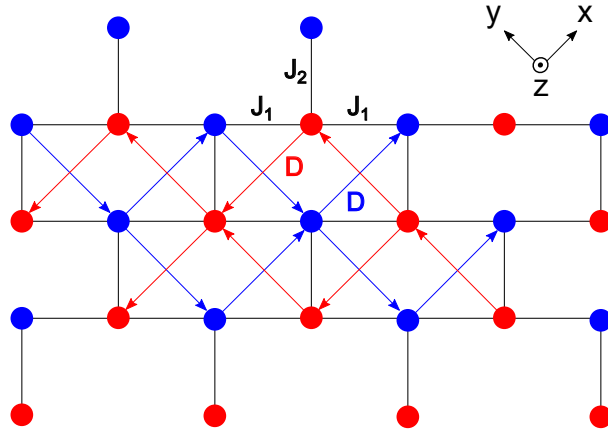

Figure 14 – The antiferromagnetic brick-wall lattice. The red sites are sublattice A, with spins pointing in the $+z$ direction. The blue sites are sublattice B, $-z$ direction. The Dzyaloshinskii-Moriya interaction has $\nu_{ij} = +1$ along the arrows, and -1 against them.

Following the same procedure as in the case of the Union Jack lattice, one gets a

Bogoliubov-de Gennes Hamiltonian (see Eq. 4.26) with parameters:

$$r = \frac{2 + \alpha}{2} J_1 S + \frac{A_1 + A_2}{2} \left(\frac{2S - 1}{2} \right)$$

$$\Delta = 2SD m_k + \frac{A_1 - A_2}{2} \left(\frac{2S - 1}{2} \right)$$

$$h_x = \frac{3}{2} J_1 S \, \delta_k$$

$$h_y = -\frac{3}{2} J_1 S \, \varepsilon_k, \tag{5.2}$$

where $\alpha \equiv J_2 / J_1$ and the structure factors are

$$\delta_k = \frac{1}{12} \left[(2 + \alpha) \cos\left(\frac{k_x}{2} \right) \cos\left(\frac{k_y}{2} \right) + \alpha \sin\left(\frac{k_x}{2} \right) \sin\left(\frac{k_y}{2} \right) \right]$$

$$\varepsilon_k = -\frac{1}{12} \left[(2 - \alpha) \cos\left(\frac{k_x}{2} \right) \sin\left(\frac{k_y}{2} \right) + \alpha \sin\left(\frac{k_x}{2} \right) \cos\left(\frac{k_y}{2} \right) \right]$$

$$m_k = \frac{1}{2} \left(\sin k_x - \sin k_y \right). \tag{5.3}$$

The imaginary part of the Bogoliubov-de Gennes Hamiltonian is contained in h_y. From the equations above, we see that $h_y \propto \varepsilon_k$, which is the complex part of the exchange interaction structure factor $\gamma_k \equiv \delta_k + i\varepsilon_k$. In Appendix B, it is shown that $h_y \neq 0$ is necessary for the Berry curvature to be non-zero. Hence, the complex lattice structure factor γ_k is responsible for the non-zero Berry curvature in this system. In the brick-wall case, the system has non-null Berry curvature even for $D = 0$. This is opposite to the AFM Union Jack lattice, there the DMI is responsible for the Berry curvature.

The structure factors are odd functions of $\mathbf{k}$. In this case, the diagonalization of the BdG Hamiltonian leads to:

$$\epsilon_\alpha (\mathbf{k}) = w (\mathbf{k}) + \Delta (\mathbf{k})$$

$$\epsilon_\beta (\mathbf{k}) = w (\mathbf{k}) - \Delta (-\mathbf{k}), \tag{5.4}$$

with w and Δ defined in 4.21 Let us first consider the case $A_1 = A_2$, which makes $\Delta (\mathbf{k}) = 2SD m_k$. As m_k is an odd function of $\mathbf{k}$, the bands are totally degenerate (Fig. 15). This degeneracy comes from an effective time-reversal symmetry, which is also responsible for a pure spin Nernst effect of magnons, when a thermal gradient generates a transverse spin current without a net heat flow. This will be shown below.

5.1   Pure spin Nernst effect of magnons

Crystal structures can be classified by the symmetries they present. An ideal crystal is a periodically repeating pattern. Since all lattice points of a periodic lattice are
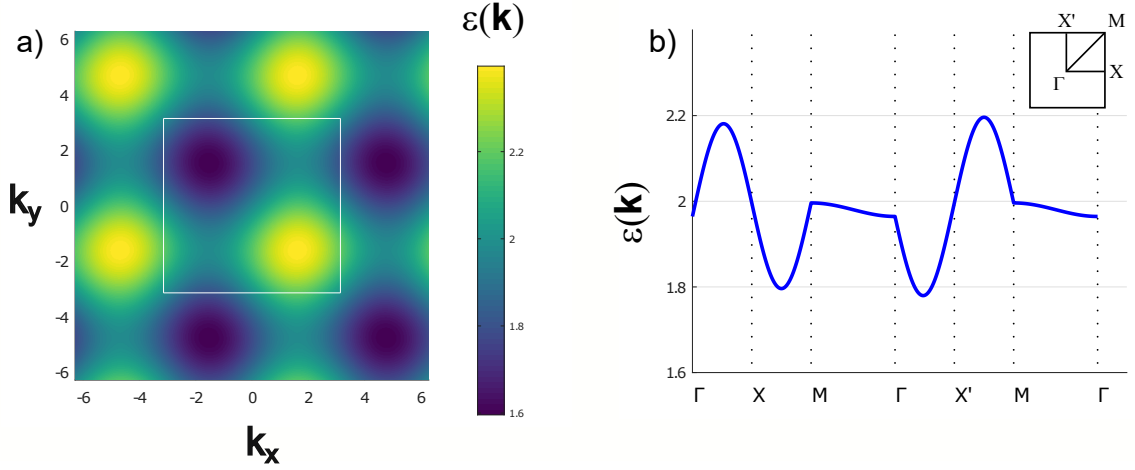
Figure 15 – Degenerate energy bands of the antiferromagnetic brick-wall lattice (a) through the Brillouin zone (white square) and (b) between the high symmetry points. The theory parameters are $S = J_1 = A_1 = A_2 = \alpha = 1$ and $D = 0.2$.

equivalent, every point has the same neighborhood as the other points. The lattice itself can be characterized by listing the symmetry operations that keep each of them fixed. When there is magnetic ordering, the crystallographic symmetries can be extended to describe magnetic crystals, observing that the magnetic lattice can be different from the crystal lattice.
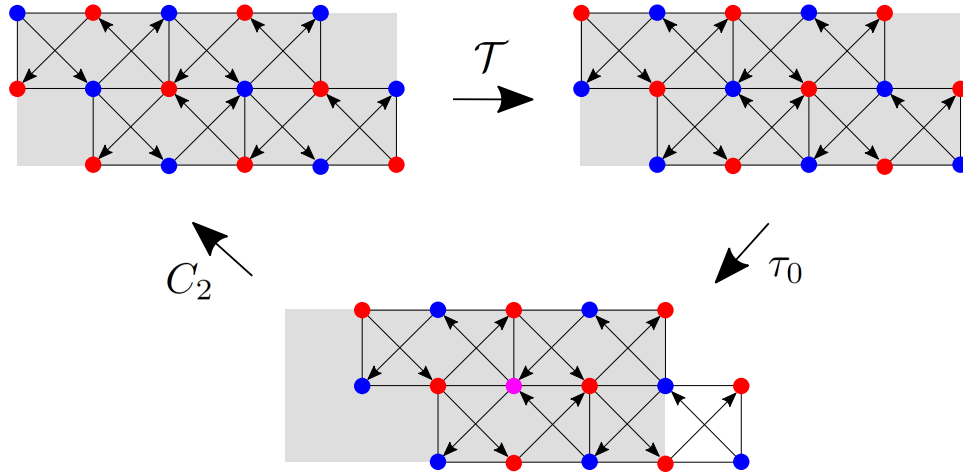
Figure 16 – Effective time-reversal symmetry $\mathcal{T}\tau_0 C_2$ of the brick-wall lattice. $\mathcal{T}$ is the time-reversal transformation, which flips the spins. τ_0 is a sublattice translation, and C_2 is a rotation of π taken around the magenta lattice site.

Space inversion and time-reversal symmetry (TRS) play a fundamental role in topological systems. Two-dimensional space inversion makes $(x, y) \to (-x, -y)$, and the time-inversion ($\mathcal{T}$) flips the spins. As a general result, the presence of those symmetries

determine the parity of the Berry curvature. Time-reversal symmetry yields $\Omega_i(\mathbf{k}) = -\Omega_i(-\mathbf{k})$ (odd function), and space inversion symmetry yields $\Omega_i(\mathbf{k}) = \Omega_i(-\mathbf{k})$ (even function, like the AFM Union Jack lattice) [16]. If both symmetries are present, $\Omega_i(\mathbf{k}) = 0$. Retrieving the well-known electronic topological systems, a Chern topological insulator must break TRS, the bulk presents the *anomalous quantum Hall effect* (AQHE) and the edge states are chiral [6]. On the other hand, a $\mathbb{Z}_2$ topological insulator does not break TRS. There is no net transverse electron transport, but as electrons with different spins flow in different directions, there is transverse spin current: the *quantum spin Hall effect* (QSHE) [10, 11].
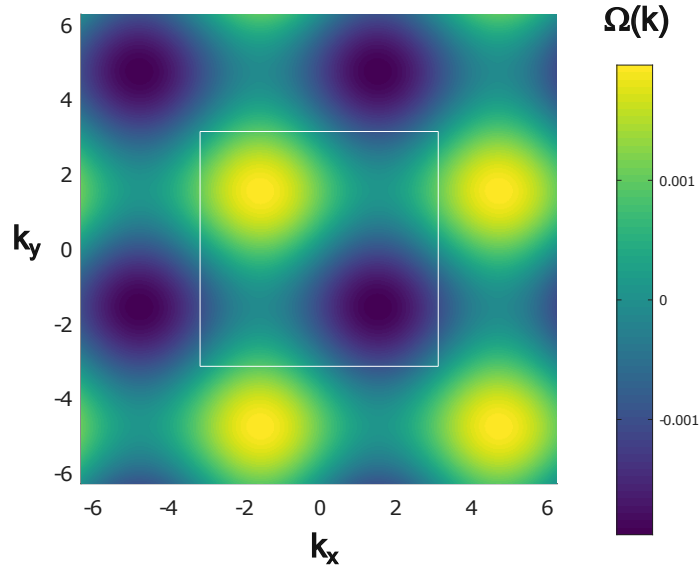
Figure 17 – Berry curvature of band α for the antiferromagnetic brick-wall lattice (same parameters as in Fig. 15). The band β has Berry curvature of opposite sign.

For magnonic systems, analogues of the effects described above can be found. An analogue of the AQHE happens when a transverse flow of magnons exists due to a thermal gradient (*thermal Hall effect* of magnons). Also, the analogue of the QSHE can happen in antiferromagnets, when magnons of opposite spin flow in opposite directions with exactly the same intensity, cancelling the energy flow but reassuring the spin current, in what is called here *pure spin Nernst effect* of magnons [115, 117]. Of course the thermal Hall effect can still happen in antiferromagnets, provided that the opposite currents do not cancel each other. That happens in the situation of a broken symmetry, analogously to the TRS in electronic systems. If this symmetry is present, the pure spin Nernst effect occur.

The mentioned symmetry cannot be the TRS itself, which is trivially broken in an antiferromagnet with Néel order: flipping all the spins swaps A and B sublattices, changing the sign of the staggered magnetization [100]. But an effective time-reversal symmetry (ETRS) can still be defined. That symmetry happens when the system is invariant under
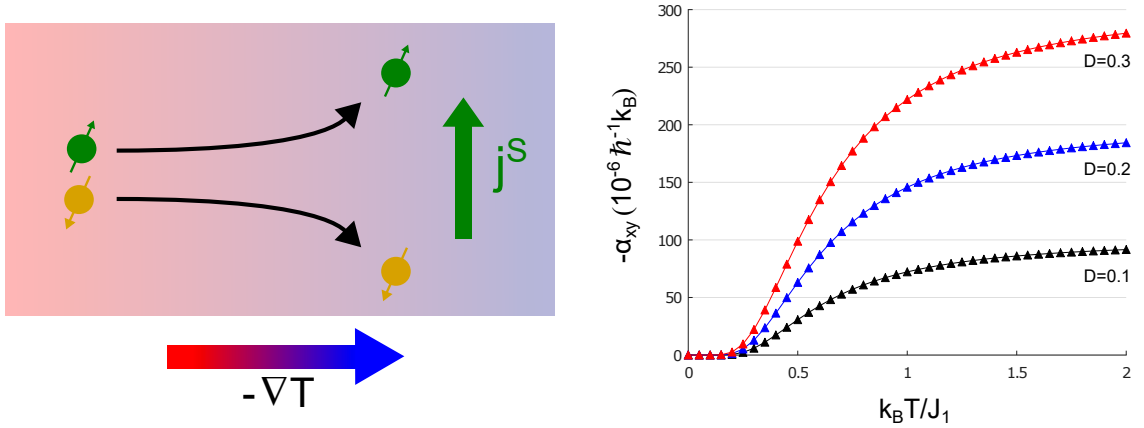
Figure 18 – The pure spin Nernst effect of magnons in the antiferromagnetic brick-wall lattice with $A_1 = A_2$. The magnons are driven in opposite directions with the same intensity, resulting in a spin current without net heat current (left). The spin Nernst coefficient α_{xy} as a function of temperature is shown on the right. The other theory parameters are the same as in Fig. 15.

the combination of the time-reversal $\mathcal{T}$ and other (or others) transformation of the system. In the brick-wall lattice with $A_1 = A_2$, that symmetry is present, identified as a combination of $\mathcal{T}$, a "sublattice translation" τ_0, and a rotation C_2 around an arbitrary lattice site (Fig. 16).

Whereas the spin Hall and thermal Hall conductivities rely on ETRS breaking, the spin Nernst effect does not [118], and can exist even when the symmetry is present. Suppose the system shows ETRS. As we have seen, that implies $\Omega_i(\mathbf{k}) = -\Omega_i(-\mathbf{k})$. That is the case of the brick-wall lattice, as it can be seen in the Berry curvature plotted in Fig. 17. In Appendix B, we show that $\Omega_\beta(\mathbf{k}) = \Omega_\alpha(-\mathbf{k})$. Those two properties yield $\Omega_\beta(\mathbf{k}) = -\Omega_\alpha(\mathbf{k})$, i.e., the bands have Berry curvatures of opposite sign. Degenerate bands with opposite Berry curvatures were also predicted for the honeycomb AFM lattice [115,117]. Considering the band degeneracy, the integrals σ_{xy} and κ_{xy} (Eq. 4.35) are zero. The same does not occur for α_{xy}, as there is a subtraction in the integrand instead of a sum. Phenomenologically, the thermal gradient $\partial_x T$ drives the two magnon modes in opposite transverse directions with the same intensity, making $\kappa_{xy} = 0$ and $\alpha_{xy} \neq 0$. That is a magnonic equivalent of the QSHE of electrons: the pure spin Nernst effect of magnons, when a temperature gradient generates a spin current without heat flow (Fig. 18). A field gradient $\partial_x B$, on the other hand, drives the two magnon modes in the same direction with the same intensity, so the spin current vanishes, $\sigma_{xy} = 0$, while a heat current is present.

In the less strict case $A_1 \neq A_2$, the bands are not degenerate, but differ by a constant factor $K \equiv (A_1 - A_2)\left(\frac{2S-1}{2}\right)$. The ETRS is broken because the sublattices are not equivalent, and all three transport coefficients are non-null (Fig. 19). When subjected to
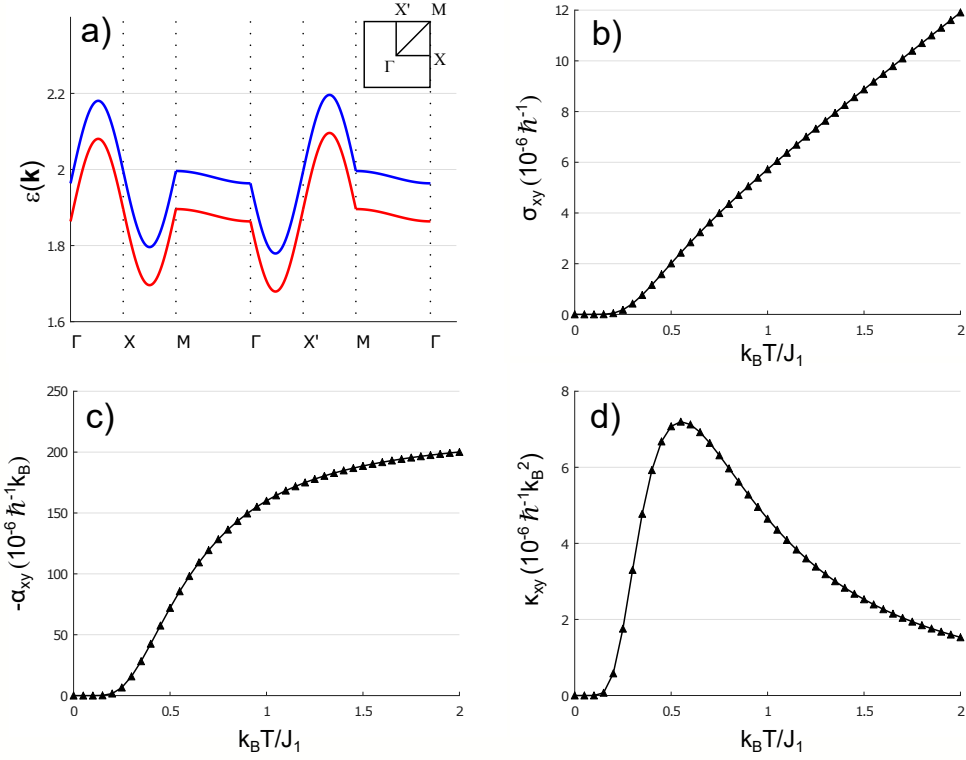
Figure 19 – (a) Energy bands and (b-d) transport coefficients of the antiferromagnetic brick-wall lattice when $A_1 \neq A_2$. The parameters are $S = J_1 = \alpha = A_1 = 1$, $A_2 = 0.8$ and $D = 0.2$. All three coefficients are non-null.

a thermal gradient, up/down magnons are driven in opposite directions but with different intensities. The system shows non-null thermal and spin currents. The same can be said about the response to a magnetic field gradient, except now the magnons flow in the same direction. One interesting fact is that, in the high-temperature limit, the thermal Hall conductivity tends to zero. This can be seen from Eq. 4.36. In the brick-wall lattice, the lower sign in the integrand is used, as $\Omega_k^\alpha = -\Omega_k^\beta$. Because the difference between energies is a constant K, we get:

$$\kappa_{xy}(T \to \infty) = k_B \int \frac{d^2k}{(2\pi)^2} \left(\epsilon_k^\alpha - \epsilon_k^\beta \right) \Omega_k^\alpha = k_B K \int \frac{d^2k}{(2\pi)^2} \Omega_k^\alpha = 0 \tag{5.5}$$

The result is naturally zero because Ω_k^α is an odd function of $\mathbf{k}$, as it can be seen in Fig. 17. The integral $\int \frac{d^2k}{(2\pi)^2} \Omega_k^{\alpha,\beta}$ is the Chern number of the bands, which is zero in either case (A_1 equal or different than A_2). This is expected from antiferromagnets in the off-plane Néel configuration [119].

6 Ferrimagnetic Cu_2F_5 monolayer

Although widely studied in FM and AFM systems, the Hall transport of magnons has not been well investigated in ferrimagnetic (FiM) lattices [33, 73]. With that in mind, in this chapter we study the magnon Hall transport in 2D layers of the proposed copper fluoride complex Cu_2F_5, which stability was predicted by first principle methods [120–122]. Our results ware published in Ref. [123].
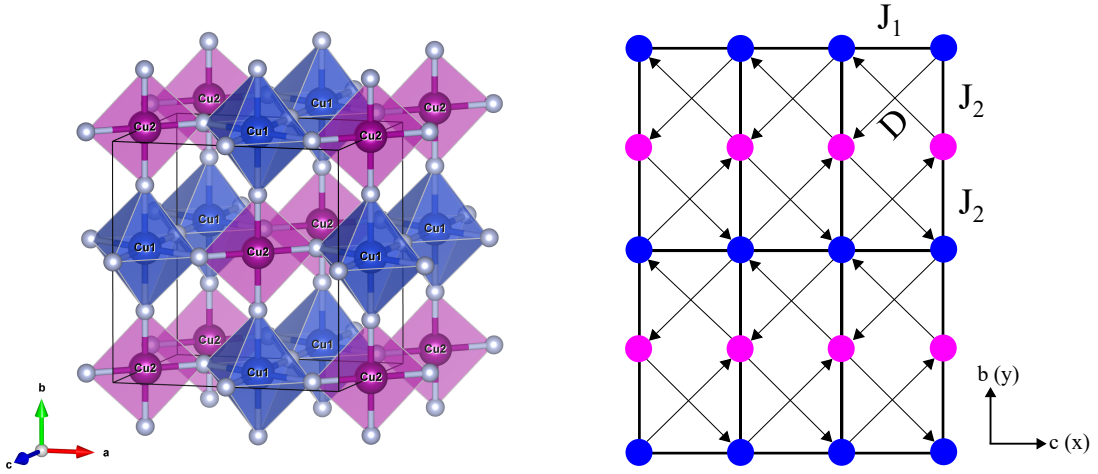
Figure 20 – The crystal structure of the Cu_2F_5 lattice (left, reproduced with permission from Ref. [121]), and the 2D model for a layer in the b-c plane of the crystal structure (right). Blue sites have spin $S = 1$, and magenta sites, $s = 1/2$.

That proposed Cu_2F_5 crystal is composed of CuF_6 distorted octahedra and CuF_4 plaquettes, as shown in Fig. 20. The inequivalent Cu ions form a magnetic crystal. We call $Cu1$ the $S = 1$ ions in the center of the octahedra, and $Cu2$ the $s = 1/2$ ions in the center of the plaquette. The most energetically favorable configuration is a G-type ferrimagnet, and DFT+U calculations show that the 3D crystal can be seen as a layered structure with the interlayer exchange parameter five times smaller than the intralayer one [121]. That inspires us to study the 2D layers from a spin wave point of view. A ferrimagnetic off-plane spin configuration is chosen, with the $S = 1$ spins pointing in the $+z$ direction and the $s = 1/2$ in the $-z$ direction. The stacked layers form a ferrimagnetic C-type configuration, and the magnetic lattice has two inequivalent sites. That is not the most stable configuration, but it is much simpler than the aforementioned G-type FiM, which has four inequivalent sites.

The exchange model which stabilizes the layer's spin order comprises a FM exchange bond between $Cu1$ sites and an AFM exchange bond between $Cu1 - Cu2$ sites. A Dzyaloshinskii–Moriya interaction is added between NNN sites. That interaction is not

present in the original proposed lattice by Korotin *et al*, but is an addition made here to explore the topology and transverse transport in the lattice. A single-ion anisotropy (SIA) in the z direction stabilizes the off-plane configuration. The Hamiltonian of the model is:

$$H = -J_1 \sum_{\langle i,j \rangle} \mathbf{S}_i \cdot \mathbf{S}_j + J_2 \sum_{\langle i,j \rangle} \mathbf{S}_i \cdot \mathbf{S}_j + D \sum_{\langle\langle i,j \rangle\rangle} \nu_{ij} \hat{\mathbf{z}} \cdot \mathbf{S}_i \times \mathbf{s}_j$$
$$- A \sum_i \left[(S_i^z)^2 + (s_i^z)^2 \right]. \tag{6.1}$$

The upper (lower) case S_1 (s_i) operator denotes the spin operators for $S = 1$ ($s = 1/2$) sites. The first term (with $J_1 > 0$) represents the FM exchange between $S = 1$ ($Cu1$) sites, and the second term (with $J_2 > 0$) represents the AFM exchange between $S = 1$ and $s = 1/2$ ($Cu1 - Cu2$) sites. Both interactions happen between near-neighbors. The third term is the DMI between NNN sites, where $\nu_{ij} = \pm 1$, following the arrow convention in Fig. 20. The last term is the single-ion anisotropy. The SIA between $1/2$ spins is ineffective, so only the first term inside the square brackets needs to be considered. From Fig. 20, it is easy to see that the lattice's geometry is the same as the modified Lieb lattice in Chapter 3, but with a "compressed" unit cell. The lattice parameter is taken as $1/2$ in the x direction, and 1 in the y direction.

A linearized Holstein-Primakoff representation for up/down spins is used:

$$S_i^+ = \sqrt{2S}\, a_i, \qquad S_i^- = \sqrt{2S}\, a_i^\dagger, \qquad S_i^z = S - a_i^\dagger a_i$$
$$s_i^+ = \sqrt{2s}\, b_i^\dagger, \qquad s_i^- = \sqrt{2s}\, b_i, \qquad s_i^z = -s + b_i^\dagger b_i. \tag{6.2}$$

That is the same representation used in the collinear AFM lattice presented in Chapter 4, but with different spin values S and s. Fourier transforming, we obtain a block-diagonal BdG Hamiltonian in the momentum space (see Eq. 4.26) with parameters:

$$r = \frac{1}{2} \left[A \left(\tilde{S} + \tilde{s} \right) + J_1 S \left(1 - \gamma_k \right) + J_2 \left(S + s \right) \right]$$
$$\Delta = \frac{1}{2} \left[A \left(\tilde{S} - \tilde{s} \right) + J_1 S \left(1 - \gamma_k \right) - J_2 \left(S - s \right) \right]$$
$$h_x = \sqrt{Ss}\, J_2 \eta_k$$
$$h_y = 2\sqrt{Ss}\, D m_k, \tag{6.3}$$

where $\tilde{S} \equiv \frac{2S-1}{2}$ and $\tilde{s} \equiv \frac{2s-1}{2}$ (in the system studied here, $\tilde{S} = 1/2$ and $\tilde{s} = 0$). The structure factors are

$$\gamma_k = \cos\frac{k_x}{2}, \qquad \eta_k = \cos\frac{k_y}{2}, \qquad m_k = -\sin\frac{k_x}{2}\sin\frac{k_y}{2}. \tag{6.4}$$

Using generalized Bogoliubov-de Gennes transformation, the physical magnon spectrum is (see 4.21):

$$\epsilon_{\alpha,\beta}(\mathbf{k}) = w(\mathbf{k}) \pm \Delta(\mathbf{k}). \tag{6.5}$$
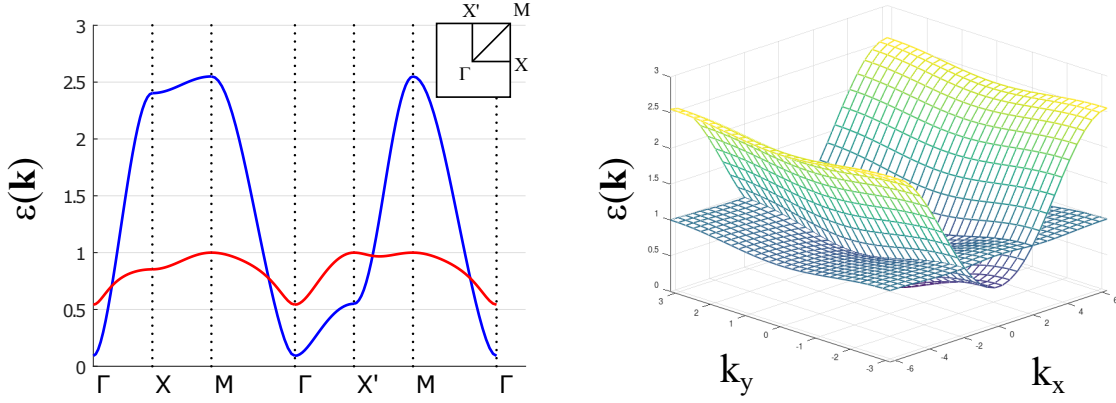
Figure 21 – Band structure of the system when $J_1 = J_2 = 1.0$, $A = 0.1$, and $D = 0.2$. On the left, band structure between high symmetry point. The blue (red) line corresponds to the α (β) magnons. On the right, the band structure in the whole Brillouin zone.

The system's band structure can be seen in Fig. 21. For values of $A < J_2$, the bands cross in two separate paths in the Brillouin zone. The α and β magnons carry magnetic dipole momentum $\sigma g_\sigma \mu_B$ with $\sigma = \mp 1$. For FM and AFM systems, the g-factor g_σ is the same for all magnon modes, so it is usually absorbed into another constant (in fact, this was done implicitly in the previous chapters). For ferrimagnets, however, usually $g_\alpha \neq g_\beta$ due to the inequivalence of the spins in the sublattices [73].

The Berry curvature of the FiM Hamiltonian is written identically to the AFM case:

$$\Omega_{\alpha,\beta}\left(\mathbf{k}\right) = -\frac{1}{2}sinh\theta_k \left(\frac{\partial \phi_k}{\partial k_x}\frac{\partial \theta_k}{\partial k_y} - \frac{\partial \phi_k}{\partial k_y}\frac{\partial \theta_k}{\partial k_x}\right), \tag{6.6}$$

with θ_k and ϕ_k defined in Eq. B.12. A plot of the Berry curvature can be seen in Fig. 22. We note that the Berry curvature is an even function, which justifies the fact that Ω_α and Ω_β have the same sign (see Appendix B). The integration of Ω_α over the Brillouin zone is zero, so the system is not a Chern insulator ($C = 0$).

6.1 Transverse transport coefficients

The transverse transport coefficients are written similarly to the AFM case, but here the bands have a different g-factors. For each band, the coefficients are:
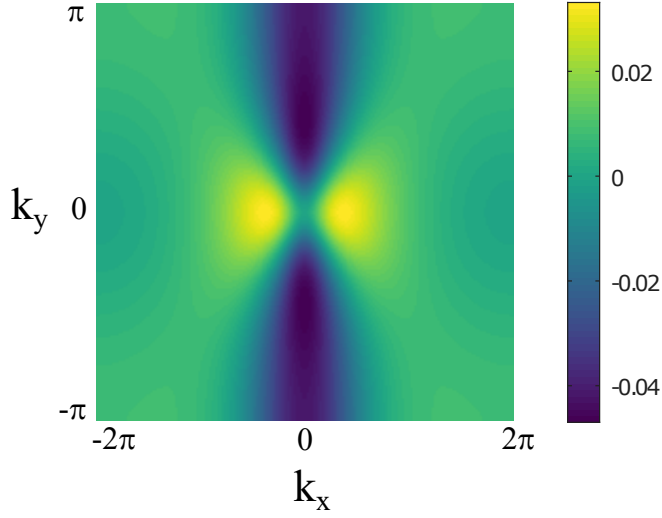
Figure 22 – Berry curvature of both bands in the Brillouin zone. Same parameters as in Fig. 21.

$$\sigma_{xy}^{\sigma} = -\frac{(g_{\sigma}\mu_B)^2}{\hbar} \int \frac{d^2k}{(2\pi)^2} n_k^{\sigma} \Omega_k^{\sigma}$$

$$\alpha_{xy}^{\sigma} = -\frac{(g_{\sigma}\mu_B) k_B}{\hbar} \int \frac{d^2k}{(2\pi)^2} c_1(n_k^{\sigma}) \Omega_k^{\sigma}$$

$$\kappa_{xy}^{\sigma} = -\frac{k_B^2 T}{\hbar} \int \frac{d^2k}{(2\pi)^2} c_2(n_k^{\sigma}) \Omega_k^{\sigma}, \tag{6.7}$$

and the combination of the transverse currents of both magnons generates the total conductivities of the system:

$$\sigma_{xy} = \sigma_{xy}^{\alpha} + \sigma_{xy}^{\beta}$$

$$\alpha_{xy} = \alpha_{xy}^{\alpha} - \alpha_{xy}^{\beta}$$

$$\kappa_{xy} = \kappa_{xy}^{\alpha} + \kappa_{xy}^{\beta}. \tag{6.8}$$

The transport coefficients of each band have different signs, so the total σ_{xy} and κ_{xy} become subtractive, while α_{xy} becomes additive. If the bands were degenerate, the subtractive coefficients would cancel out as it happens in the brick-wall lattice in the last chapter, but this is not the case here. The transport coefficients versus temperature are plotted in Fig. 23. We see the well-known asymptotic behavior of $\alpha_{xy}(T)$ and $\kappa_{xy}(T)$. The coefficients increase with D, and vanish when $D = 0$ (as well as the Berry curvature).

For $A \geq J_2$ it is possible to observe an interesting behavior of σ_{xy} and κ_{xy}: the curves are non-monotonic and present a sign change, while that does not occur α_{xy} (Fig. 24). That can be explained as follows. When $A \geq J_2$, the narrower β-band does not cross
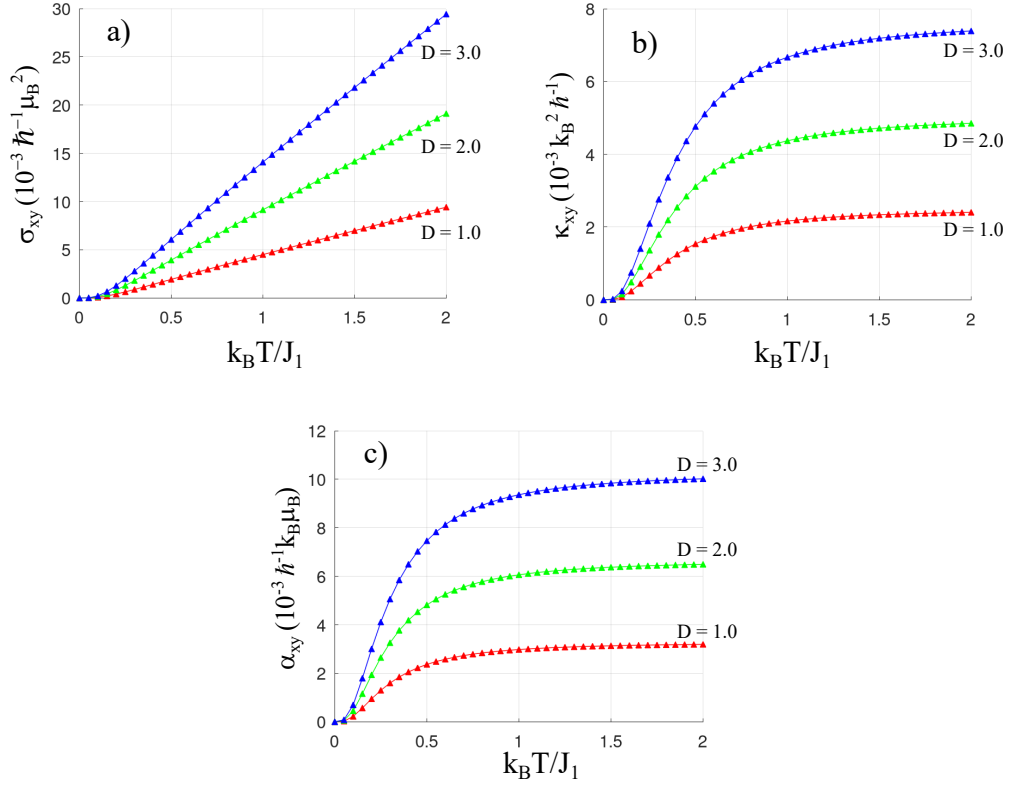
Figure 23 – (a) Spin Hall conductivity, (b) thermal Hall conductivity and (c) spin Nernst coefficient as functions of $k_B T/J_1$. The parameters are $J_1 = J_2 = 1.0$, $A = 0.1$, $g_\alpha = 1.2$, $g_\beta = 1.0$ and three values of D.

the wider α-band (Fig. 23d). In low temperatures, the lower band dominates, so in this case, the narrower band (which has negative σ^{β}_{xy} and κ^{β}_{xy}) is more populated, resulting in negative total transport coefficients. As the temperature rises, the population in the wider band surpasses the narrower one, and the total σ^{β}_{xy} and κ^{β}_{xy} become positive. This competition does not occur for α_{xy}, which is additive. That behavior of σ^{β}_{xy} and κ^{β}_{xy} does not occur for $A < J_2$, as the wider band reaches lower values, and its population dominates in all temperatures.

The non-monotonic character of the curves does not change with the inclusion of NN exchange between the $s = 1/2$ sites. However, the valley becomes rapidly less pronounced and closer to $T = 0$ with the rise of the exchange parameter. We also investigated the role of different spins in the lattice, and the conclusion was that the curves can be non-monotonic independently of spin value for both sites, provided that at least one spin is different from $1/2$. That occurs even for $S = s$ (the AFM case, when the bands touch but do not cross), for all values of A. In summary, the necessary conditions for the non-monotonic behavior are: (1) The SIA exists and is effective ($A \neq 0$ and at least one spin is different from $1/2$), and (2) the bands do not cross. This behavior seems to be an intrinsic feature of
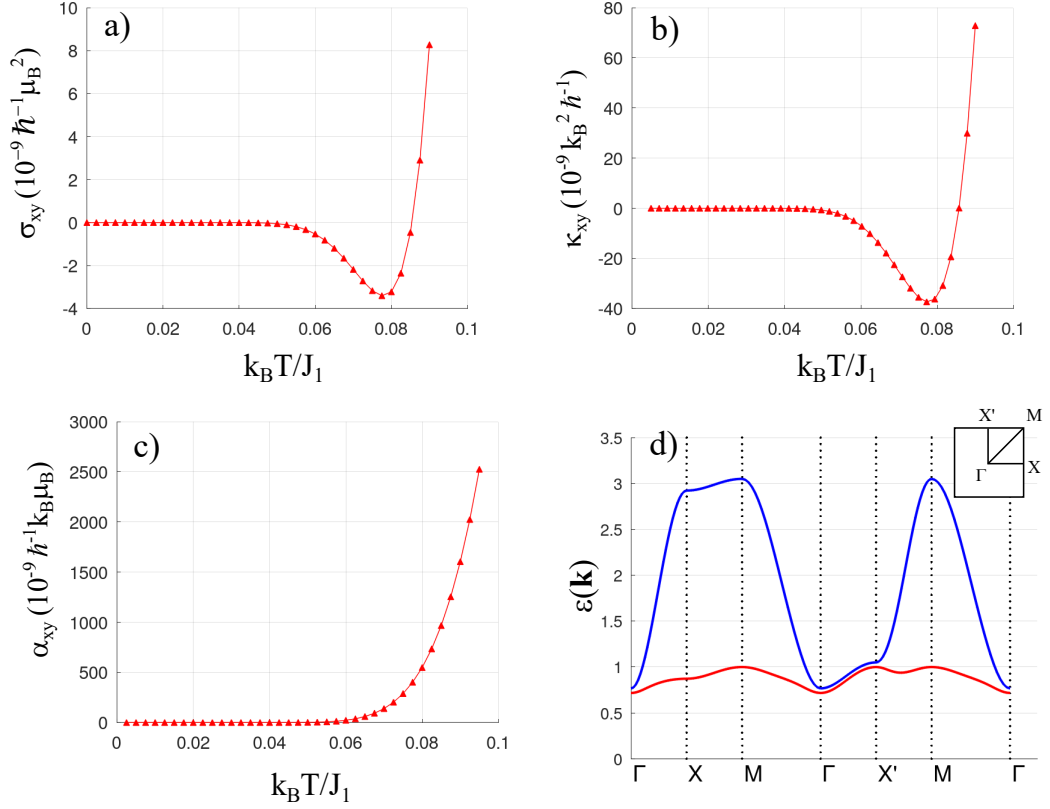
Figure 24 – Transverse transport coefficients (a-c) and band structure (d) for the system when $A \geq J_2$. The parameters are $J_1 = J_2 = 1.0$, $D = 0.3$, $A = 1.1$, $g_\alpha = 1.2$ and $g_\beta = 1.0$.

the system's geometry and spin ordering studied here. The change of sign that follows the non-monotonic transport coefficients, which also happens in other magnon systems, opens the exciting possibility of controlling the direction of transverse magnon flow with the change of temperature.

7 Non-Hermitian fermionic checkerboard lattice

As mentioned in the Introduction, non-Hermitian Hamiltonians can describe systems subjected to gain and loss of particles and/or energy. The interplay between non-Hermiticity and topological effects has recently become an active field of study. In this chapter, we study a fermionic non-Hermitian Hamiltonian in the checkerboard lattice, which is known to hold non-trivial topology. Our results are presented as a preprint in [124].

The checkerboard lattice is a two-dimensional lattice structure with square geometry, which can be seen as a planar version of the pyrochlore lattice [84, 86, 87, 89, 125–136]. The experimental realization is challenging, but the structure has already been discovered in some compounds [137–139]. The checkerboard lattice has some interesting properties. For instance, it is a member of a set of structures known as line-graph lattices, which can show flat bands and spatially localized states [132, 133]. It has also been shown that it can hold a variety of topological states [84, 86, 87, 89, 126, 129–132, 134–136]. Using a tight-binding approach, one can construct a non-Hermitian fermionic Hamiltonian in the checkerboard geometry, in order to study its topology and transverse transport.

7.1 Non-Hermitian Hamiltonian for open systems

One widely recognized way to describing open quantum systems involves the use of non-Hermitian Hamiltonians. These open systems account for many physical processes, for instance, the interaction with a surrounding environment or an experimental apparatus of continuous measurements [42]. Regarding the interaction of a two-band quantum system with its surroundings, one way to describe it is to locally couple the system to a series of baths, representing the environment [140]. That formalism accounts for a lossy system, where quasiparticles have a finite lifetime due to dissipation. Integrating out the baths' degrees of freedom, one obtains a Green function of the form $G\left(\mathbf{k}, \epsilon\right) = \left(\epsilon - H\left(\mathbf{k}\right) - \Sigma\left(\mathbf{k}, \epsilon\right)\right)^{-1}$. The term $\Sigma\left(\mathbf{k}, \epsilon\right)$ is the self-energy and contains information about the bath modes. The effective Hamiltonian $H_{eff}\left(\mathbf{k}\right)$ includes a dissipation term $H_{diss} = i\left(\gamma_j \sigma_j\right), j = (0, x, y, z)$, which makes it non-Hermitian.

Non-Hermitian Hamiltonians have complex eigenvalues and distinct right and left eigenstates, demanding a biorthogonal algebra [141, 142]. In the formalism of coupled baths described above, the physical requirement that the system's density of states is non-negative results in a constraint to the complex eigenvalues: their imaginary part has to be non-positive [140].

Regarding the transport properties of quasiparticles, it is established that the Hall conductivity for a two-dimensional fermionic system can be obtained from the Matsubara Green function G as [57, 143–145]:

$$\sigma_{xy} = \frac{e^2}{h} \frac{\varepsilon_{\mu\nu\rho}}{24\pi^2} \int d^3p \, Tr \left[G \frac{\partial G}{\partial p_\mu} G \frac{\partial G}{\partial p_\nu} G \frac{\partial G}{\partial p_\rho} \right], \tag{7.1}$$

where we assume $T = 0 \, K$ so the sum over Matsubara frequencies becomes an integral. The expression above works for Hermitian and non-Hermitian Hamiltonians, provided that the Green function is known. For a Hermitian Hamiltonian, this Hall conductivity is quantized and gives rise to the integer Hall effect, as a consequence of the non-trivial topology of the Hamiltonian. The system is a topological insulator due to the bulk-edge correspondence. Evaluating expression 7.1 is an alternative approach to the linear response theory presented in Chapter 2, but yields the same results for free fermions [142], if the free particle Green functions are used. The non-Hermitian linear response theory is still a field in development [146–149], and its evaluation for specific systems is a complicated procedure, which justifies this alternative approach.

For a non-Hermitian system, the self-energy $\Sigma(\mathbf{k}, \epsilon)$ spoils the quantization of the Hall conductivity even if the system is a Chern insulator [37,57,145]. The reason is that the non-Hermitian Green functions are not continuous functions of the Mastsubara frequency $i\omega$, but have a discontinuity in $i\omega = 0$. That discontinuity creates extra terms in Eq. 7.1, which breaks down the quantization observed in Hermitian systems.

7.2   Hermitian checkerboard lattice

We begin by presenting some results for the Hermitian checkerboard lattice before advancing to the non-Hermitian case. The checkerboard lattice is represented in Fig. 25, with tight-binding Hamiltonian written as:

$$H^H = -t \sum_{\langle i,j \rangle} e^{i\phi_{ij}} \left(c_i^\dagger c_j + h.c. \right) - \sum_{\langle\langle i,j \rangle\rangle} t'_{ij} \left(c_i^\dagger c_j + h.c. \right). \tag{7.2}$$

Here, $c_i^\dagger$ (c_i) is the fermion creation (annihilation) operator at site i. The pairs $\langle i, j \rangle$ and $\langle\langle i, j \rangle\rangle$ represent NN and NNN sites, respectively. There are two inequivalent sites in the primitive cell. The NN hopping is complex, carrying a phase factor $\phi_{ij} = \pm\phi$ with the sign determined by the arrows' directions in Fig. 25. That term breaks the time-reversal symmetry for $\phi \neq n\pi$ ($n \in \mathbb{Z}$) and allows non-trivial topology [131]. The NNN hopping $t'_{ij} = t'_1$ (t'_2) is represented by solid (dashed) lines. As a minimal model, we take $t'_2 = 0$ and define $t' \equiv t'_1$. In the momentum space, the general Hermitian Hamiltonian is:
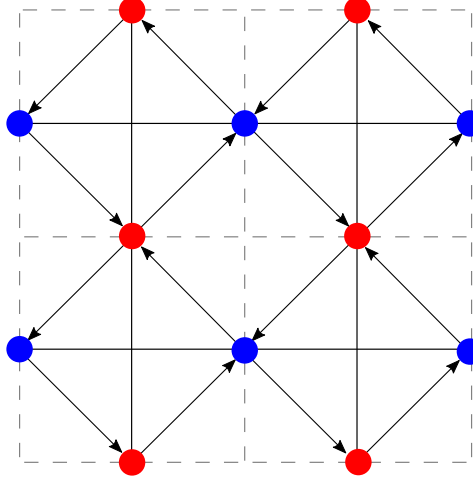
Figure 25 – The checkerboard lattice. The inequivalent sites are represented in blue and red. The near-neighbor hopping is complex, with a phase of $+\phi$ in the direction of the arrows and $-\phi$ against it. The solid vertical and horizontal lines represent next-near-neighbor hopping

$$H^H = \sum_k \psi_k^\dagger H_k^H \psi_k, \tag{7.3}$$

with $\psi^\dagger = \begin{pmatrix} a_k^\dagger & b_k^\dagger \end{pmatrix}$. The checkerboard Hamiltonian matrix takes the form

$$H_k^H = d_0 I + d_x \sigma_x + d_y \sigma_y + d_z \sigma_z \tag{7.4}$$

with

$$d_0 = -t' \left(\cos k_x + \cos k_y \right)$$
$$d_x = -4t \cos\phi \left(\cos\frac{k_x}{2} \cos\frac{k_y}{2} \right)$$
$$d_y = -4t \sin\phi \left(\sin\frac{k_x}{2} \sin\frac{k_y}{2} \right)$$
$$d_z = -t' \left(\cos k_x - \cos k_y \right). \tag{7.5}$$

We note that Hamiltonian 7.4 is formally identical to the magnonic FM Hamiltonian presented in Section 3. The Hamiltonian's eigenvalues are:

$$\epsilon_\pm = d_0 \pm d, \qquad d \equiv \sqrt{d_x^2 + d_y^2 + d_z^2}, \tag{7.6}$$

and the spectrum is gapped for $\phi \neq m\pi$ $(m \in \mathbb{Z}/2)$.

The bands' Berry curvatures are also formally identical to the expression presented in Section 3. For the valence band, it is written as

$$\Omega_{xy}\left(\mathbf{k}\right) = \hat{\mathbf{d}} \cdot \left(\frac{\partial \hat{\mathbf{d}}}{\partial k_x} \times \frac{\partial \hat{\mathbf{d}}}{\partial k_y}\right) \tag{7.7}$$

with $\hat{\mathbf{d}} = \mathbf{d}/d$, $\mathbf{d} = (d_x, d_y, d_z)$. From the linear response theory, the Hall conductivity is given by:

$$\sigma_{xy} = -\frac{e^2}{h} \int \frac{d^2k}{4\pi} \Omega_{xy}\left(\mathbf{k}\right) = -\frac{e^2}{h}C. \tag{7.8}$$

That is the expression for the integer quantum Hall effect presented in Section 2.3. It differs from the magnonic case, as in the fermionic case at $T = 0$ the valence band is occupied with $n_{FM} = 1$ and the conduction band in unoccupied. Here, $C \equiv \int \frac{d^2k}{4\pi} \Omega_{xy}\left(\mathbf{k}\right)$ is the Chern number. In the case of a two-band insulator, the Chern number has a natural geometrical interpretation. As $\mathbf{k}$ spreads over the Brillouin torus, the parameter vector $\mathbf{d}$ describes a surface. The Chern number represents the number of times this surface wraps around the origin (the winding number).

In Hermitian systems, a non-trivial Chern number is related to robust conducting edge states via bulk-boundary correspondence, making the system a topological insulator. In the gapped checkerboard lattice, the Chern number of the valence band is $C = -1$ if ϕ lies in the first and third quadrants, and $C = +1$ for ϕ in the second and fourth quadrants. For $\phi = n\pi/2$, the system is ungapped. The bands touch quadratically at the corners of the Brillouin zone for even n, and in the center for odd n.

7.3 The Non-Hermitian case

One way of obtaining a non-Hermitian Hamiltonian is to include an anti-Hermitian diagonal term in the momentum-space Hamiltonian:

$$H^{AH} = \sum_k \psi_k^\dagger H_k^{AH} \psi_k, \tag{7.9}$$

where

$$H_k^{AH} = i \begin{pmatrix} \gamma_a & 0 \\ 0 & -\gamma_b \end{pmatrix} = i \begin{pmatrix} \gamma_0 + \gamma_z & 0 \\ 0 & \gamma_0 - \gamma_z \end{pmatrix}$$

$$= i\left(\gamma_0 I + \gamma_z \sigma_z\right). \tag{7.10}$$

Here, we define $\gamma_0 \equiv \frac{(\gamma_a - \gamma_b)}{2}$ and $\gamma_z \equiv \frac{(\gamma_a + \gamma_b)}{2}$.
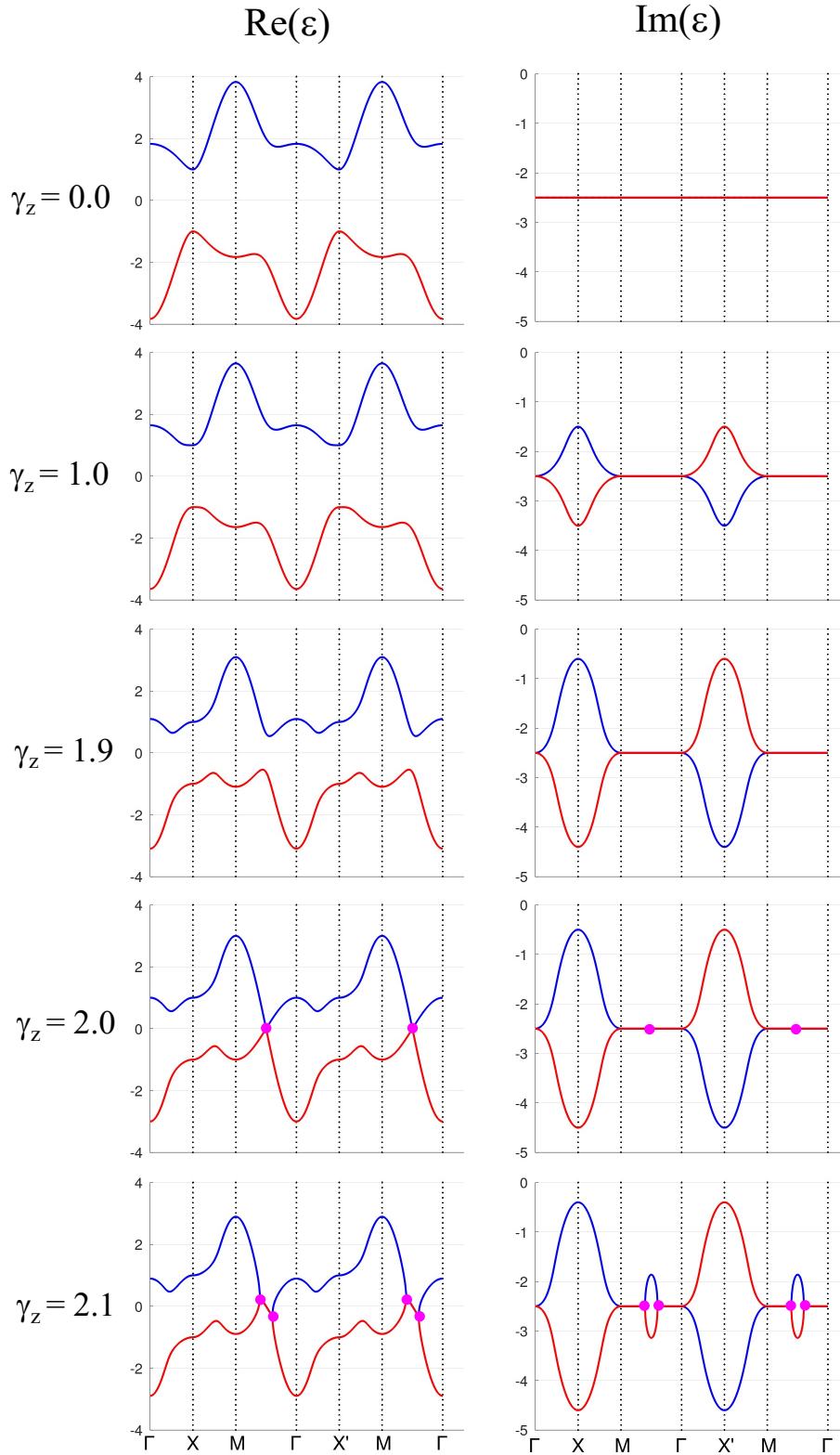
Figure 26 – Energy spectrum (real and imaginary parts) of the system for different values of γ_z. The points of high symmetry are $\Gamma(0,0)$, $X(\pi,0)$, $X'(0,\pi)$, $M(\pi,\pi)$. For $\gamma_z = 2$, a hybrid exceptional point (in magenta) is generated in the center of the $\Gamma - M$ line, which splits into two ordinary exceptional points for $\gamma_z > 2$. The other parameters of the model are $t = 1.0$, $t' = 0.5$, $\phi = \pi/4$, $\gamma_0 = -2.5$.

The total non-Hermitian Hamiltonian $H_k^{NH} = H_k^H + H_k^{AH}$ can be written with complex parameters $h_i \equiv d_i + i\gamma_i$ as

$$H_k = h_0 I + h_x \sigma_x + h_y \sigma_y + h_z \sigma_z. \tag{7.11}$$

That is a general form. In our system, the only non-real parameters (which carry the non-Hermiticity) are $h_0 = d_0 + i\gamma_0$ and $h_z = d_z + i\gamma_z$. Diagonalizing the Hamiltonian, we obtain the eigenvalues:

$$\epsilon_\pm = h_0 \pm h, \tag{7.12}$$

with

$$h = \sqrt{h_x^2 + h_y^2 + h_z^2} = \sqrt{d_x^2 + d_y^2 + (d_z + i\gamma_z)^2}$$
$$= h^R + ih^I. \tag{7.13}$$

The eigenvalues are complex, with:

$$Re\,\epsilon_\pm = d_0 \pm h^R$$
$$Im\,\epsilon_\pm = \gamma_0 \pm h^I. \tag{7.14}$$

Within the interpretation of system-environment coupling derived in Ref. [140], $Im\,\epsilon_\pm$ must be negative, ensuring the density of states is non-negative. To fulfil this property it is sufficient to assume $\gamma_0 < 0$ and $|\gamma_0| > \gamma_z$. The spectrum is shown in Fig. 26 for different values of γ_z.

For high values of γ_z the gap closes in exceptional points (EPs). Exceptional points are a unique and interesting characteristic of non-Hermitian systems. On an EP, in addition to the gap closing $\epsilon_+ = \epsilon_-$, the system's eigenstates coalesce, and the Hamiltonian is said to be defective: the dimension of the Hilbert space is reduced. [42]. For our system, Fig. 26 shows hybrid exceptional points at $\mathbf{k}_{HEP} = (\pm\pi/2, \pm\pi/2)$ when $\gamma_z = 2$. Those are called "hybrid" because they result from the merging of two ordinary exceptional points with opposite vorticities or winding numbers [150–152]. In fact, for $\gamma_z > 2$, each hybrid EP splits in two ordinary EPs localized in the $\Gamma - M$ line. These coupled EPs are linked by a path in which the eigenvalues' real parts are identical, which can be called a *bulk Fermi arc* [43, 55], and is a consequence of $\mathcal{PT}$ symmetry of the Hamiltonian [44].

As the eigenvalues of non-Hermitian systems are complex, a different nomenclature has been proposed to describe the non-Hermitian analogues of "gapped", "fully gapped"
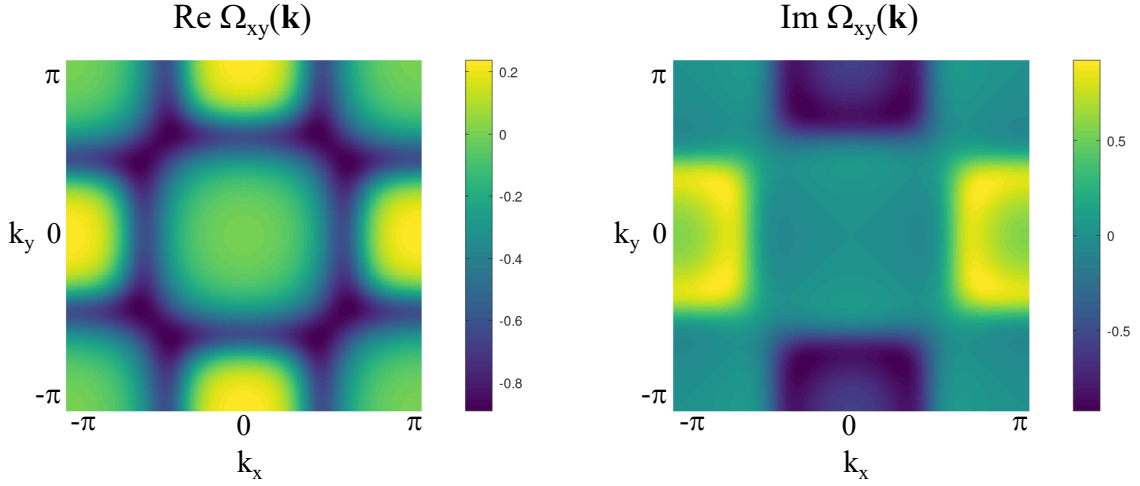
Figure 27 – Complex Berry curvature of the non-Hermitian checkerboard lattice. The theory parameters are $t = 1.0$, $t' = 0.5$, $\phi = \pi/4$, $\gamma_z = 1.5$.

and "gapless" bands, which become, respectively, "separable", "isolated" and "inseparable" bands [150]. In Fig. 26, the bands are isolated for $\gamma_z < 2$ and inseparable for $\gamma_z \geq 2$.

7.4   Hall conductivity

One can generalize the Berry curvature in Eq. 7.7 to non-Hermitian systems, obtaining a non-Hermitian complex Berry curvature [56]:

$$\Omega_{xy}\left(\mathbf{k}\right) = \hat{\mathbf{h}} \cdot \left(\frac{\partial \hat{\mathbf{h}}}{\partial k_x} \times \frac{\partial \hat{\mathbf{h}}}{\partial k_y}\right), \tag{7.15}$$

where $\hat{\mathbf{h}} = \mathbf{h}/h$, $\mathbf{h} = (h_x, h_y, h_z)$. Actually, because of the difference between right and left eigenstates, one can construct four different "Berry curvatures" $\Omega_{xy}^{\alpha\beta}\left(\mathbf{k}\right) = i\varepsilon_{xy} \left\langle \partial_{k_x}\psi^\alpha\left(\mathbf{k}\right)\middle|\partial_{k_y}\psi^\beta\left(\mathbf{k}\right)\right\rangle$, where $\alpha, \beta = L/R$ [150]. We use here $\Omega_{xy}\left(\mathbf{k}\right) \equiv \Omega_{xy}^{LR}\left(\mathbf{k}\right)$, which is well-suited for systems with loss and gain. The non-Hermitian Chern number is defined as in the Hermitian case: $C \equiv \int \frac{d^2k}{4\pi} \Omega_{xy}^{\alpha\beta}\left(\mathbf{k}\right)$. It is a real and quantized number and does not depend on α, β, even though $\Omega_{xy}^{\alpha\beta}\left(\mathbf{k}\right)$ are locally different.

In Hermitian systems, non-trivial Chern numbers are related to robust edge states through the bulk-edge correspondence, characterizing a topological insulator. This bulk-edge correspondence breaks down in non-Hermitian systems. It has been argued that it can be restored defining a non-Bloch Chern number as the integral of the Berry curvature over an extended complex Brillouin zone [58]. Nevertheless, the bulk Hall transport is unaffected by that. The Hall conductivity in Eq. 7.1 can be written as [57]:

$$\sigma_{xy} = -\frac{e^2}{h} \int \frac{d^2k}{2\pi^2} Re \left[\hat{\mathbf{h}} \cdot \left(\partial_{k_x} \hat{\mathbf{h}} \times \partial_{k_y} \hat{\mathbf{h}} \right) \times \right.$$

$$\left. \times \left(\frac{\pi}{2} sgn\left(Re\,h\right) - \frac{ihh_0}{h^2 - h_0^2} - i\,arctanh\left(\frac{h_0}{h}\right) \right) \right]$$

$$= -\frac{e^2}{h} \int \frac{d^2k}{4\pi} Re\left[\Omega_{xy}\left(\mathbf{k}\right) f\left(\mathbf{k}\right) \right]. \tag{7.16}$$
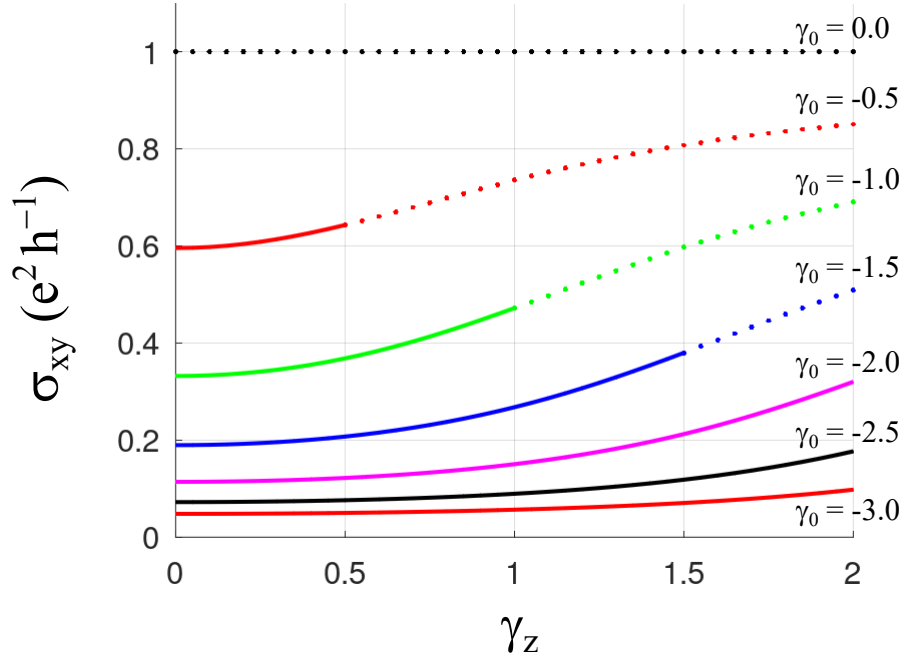
Figure 28 – Hall conductivity of the non-Hermitian checkerboard lattice as a function of γ_z. Different curves represent different values of γ_0. The other parameters are $t = 1.0$, $t' = 0.5$ and $\phi = \pi/4$. The dotted sections of the plots are not physical in the coupled baths model ($\gamma_z > |\gamma_0|$). The data does not go further than $\gamma_z = 2.0$ because this is the value of gap closing, where the Berry curvature diverges.

The conductivity now bears a factor $f\left(\mathbf{k}\right)$ in the integrand, and the integral cannot be identified with the Chern number. Therefore, there is no topological interpretation of the Hall response, and the Hall conductivity for a non-Hermitian topological Chern insulator is in general non-quantized. That can also be seen as a consequence of a discontinuity in the Matsubara Green function around $i\omega = 0$ [57]. Taking the Hermitian limit $\mathbf{h} \to \mathbf{d}$, it is easy to show that the expression above reduces to Eq. 7.8, restoring the integer quantum Hall effect.

In the insulating regime (isolated bands), the non-Hermitian Chern number was numerically calculated and is equal to $C = \pm 1$, identically to the Hermitian version of the system. The values of ϕ for which the gap closes are not only $n\pi/2$ (as in the Hermitian

case), but an interval around those values. In that interval, the gap closes in exceptional points, the Berry curvature diverges and the Chern number is not defined. As long as one stays in the insulating phase, the Chern topology is identical to the Hermitian system. The real and imaginary parts of the Berry curvature are plotted in Fig. 27. Note that $Im\,\Omega_{xy}(\mathbf{k})$ has a symmetry such that its integral is null, making the Chern number a real integer.

The Hall conductivity as a function of γ_z is plotted in Fig. 28. The conductivity increases with the raise of γ_z, but decreases with the raise of $|\gamma_0|$. This is in accordance with the interpretation that, for systems coupled to the environment, $|\gamma_0| > \gamma_z$ represents a net loss, i.e., particles with finite lifetimes [142]. A high value of $|\gamma_0|$ means higher loss (or shorter quasiparticle lifetime), decreasing the charge carriers in equilibrium and damping the conductivity. The opposite occurs for a high γ_z, which means longer quasiparticle lifetime (less loss), resulting in a higher conductivity.
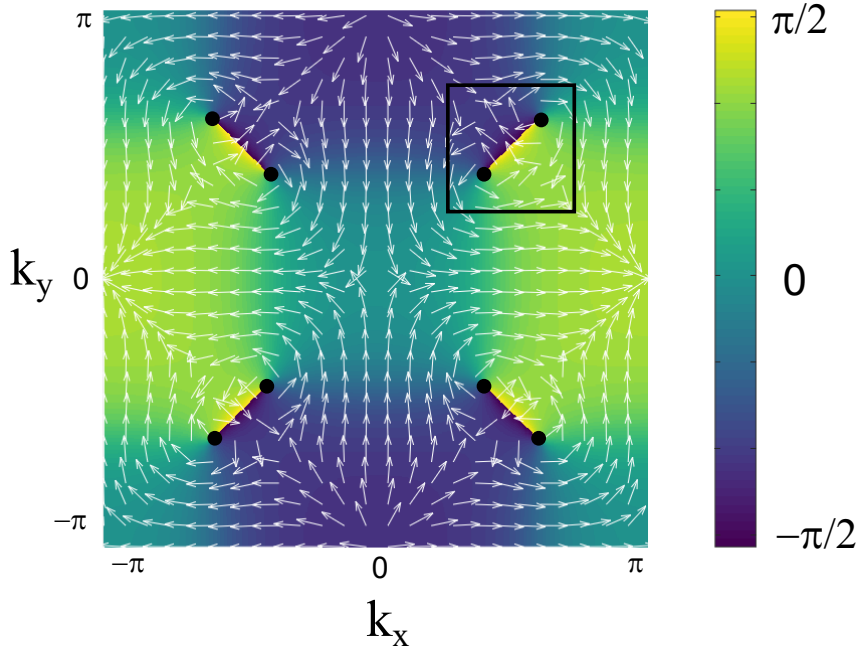
Figure 29 – The function $arg\,[\epsilon_+(\mathbf{k}) - \epsilon_-(\mathbf{k})]$, plotted as a color map. The direction of its gradient is plotted as white arrows, and the exceptional points are the black dots. The parameters are $t = 1.0$, $t' = 0.5$, $\phi = \pi/4$, $\gamma_0 = -2.5$, and $\gamma_z = 2.1$. The region inside the black contour is zoomed in on Fig. 30.

7.5 Exceptional points

As briefly mentioned above, an unique feature of non-Hermitian systems is the presence of exceptional points (EPs). In addition to being points of band degeneracy, in those points the eigenstates coalesce and the dimension of the Hilbert space is reduced.

Exceptional points can be topologically classified by their vorticity. This classification is related to the energy eigenvalues rather than the eigenstates [61, 150], in opposition to Chern or $\mathbb{Z}_2$ topology. The vorticity of a pair of states m and n through a closed loop Γ is defined as [150]:

$$\nu_{mn}(\Gamma) = -\frac{1}{2\pi} \oint_{\Gamma} \nabla_{\mathbf{k}}\, arg\, [\epsilon_m(\mathbf{k}) - \epsilon_n(\mathbf{k})] \cdot d\mathbf{k}. \tag{7.17}$$
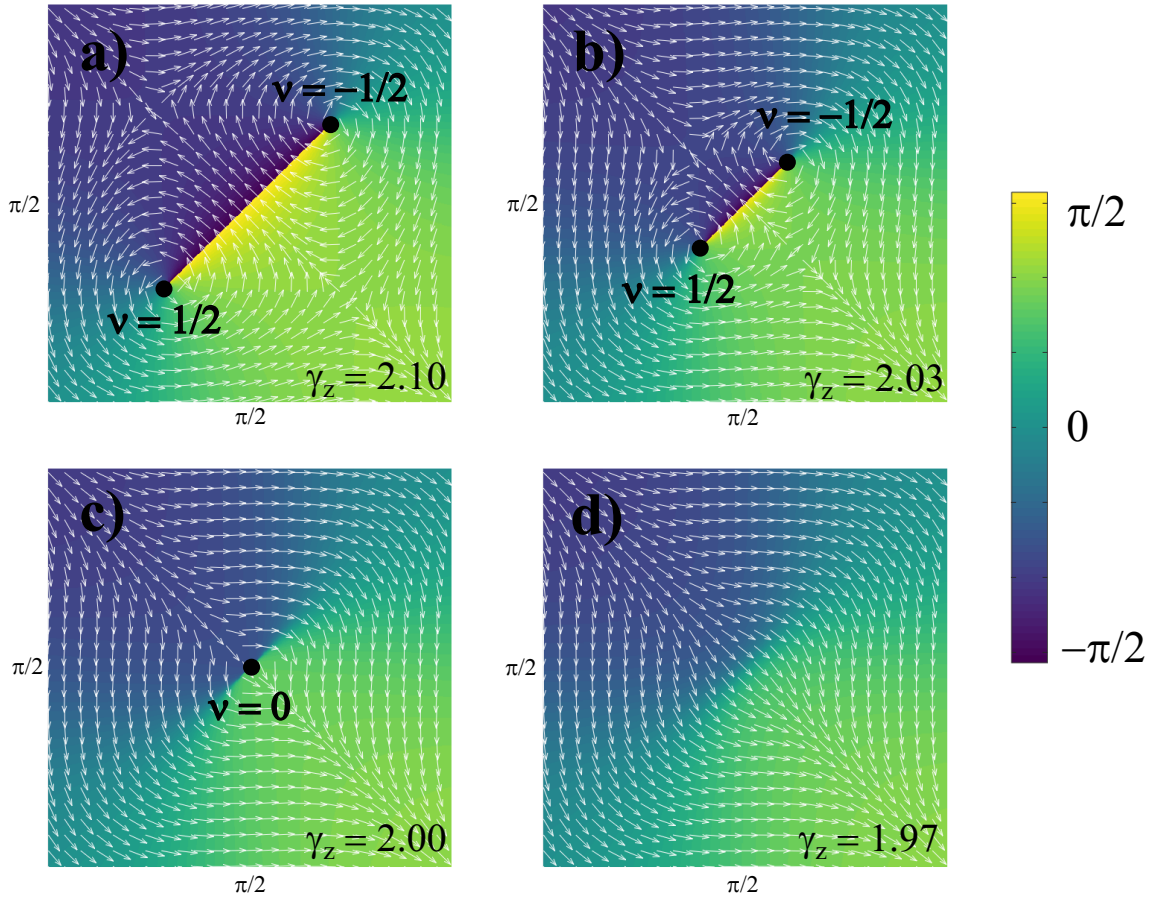
Figure 30 – Detail of the function $arg\,[\epsilon_+(\mathbf{k}) - \epsilon_-(\mathbf{k})]$ showing a pair of exceptional points centered in $(\pi/2, \pi/2)$ with their respective vorticity ν. As γ_z rises, the exceptional points merge into a hybrid exceptional point before vanishing. The parameters are the same as in Fig. 29, but for four values of γ_z: (a) $\gamma_z = 2.1$, (b) $\gamma_z = 2.03$, (c) $\gamma_z = 2.0$ and (d) $\gamma_z = 1.97$.

If the loop encloses exceptional points (where the Hamiltonian is defective), the vorticity can be non-zero, but is restricted to half-integers. This $\mathbb{Z}/2$ index is robust and can be considered a topological classification of the exceptional points.

For the non-Hermitian checkerboard lattice, exceptional points appear for high values of γ_z, when the gap closes and the system is no longer an insulator. In Fig. 29 the

function $arg\left[\epsilon_{+}\left(\mathbf{k}\right)-\epsilon_{-}\left(\mathbf{k}\right)\right]$ is plotted as the color map. That function is the phase of the (complex) energy difference $\epsilon_{+}-\epsilon_{-}$, and reaches from $-\pi/2$ to $\pi/2$. As it can be seen, there are four lines of discontinuity centered in $(\pm\pi/2,\pm\pi/2)$ (the bulk Fermi arcs), where the function jumps from $-\pi/2$ to $\pi/2$. These lines start and end in exceptional points. If the closed loop in Eq. 7.17 is chosen to encircle only one EP, it is easy to see that the integral will be reduced to the difference of phase through the Fermi arc, which is $\pm\pi$, and the vorticity of each EP is $\pm1/2$. In Figs. 29 and 30, the arrows represent the direction of $\nabla_{\mathbf{k}}\,arg\left[\epsilon_{+}\left(\mathbf{k}\right)-\epsilon_{-}\left(\mathbf{k}\right)\right]$, and the opposite vorticity of the EPs can be easily observed.

As the value of γ_z decreases, the paired EPs get closer, and merge for some value of γ_z (Fig. 30). In this point, the Hamiltonian is still defective and the spectrum is still ungapped, as it can be seen in Fig. 26 for $\gamma_z=2.0$. Nevertheless, its vorticity is $\nu=0$, as it is the result of merging two EPs with opposite vorticity. This point exhibits a square-root dispersion of $Re\,\epsilon\left(\mathbf{k}\right)$ along some direction but a linear dispersion along an orthogonal direction, as it can be seen in Fig. 31. That behaviour is in opposition to "regular" EPs, which exhibit square-root dispersion in all directions (except over the bulk Fermi arc where $Re\,\epsilon\left(\mathbf{k}\right)$ is degenerate). Points with that behaviour are called *hybrid exceptional points* [150–152]. Opposite to regular EPs, those points are not stable: any change in the parameters makes them split into two regular EPs or vanish into a gapped $Re\,\epsilon\left(\mathbf{k}\right)$ dispersion (see Fig. 26). In the gapped regime (isolated bands), no EP is present. The Berry curvature and Chern number are well-behaved and it is possible to calculate the Hall conductivity, as it is was done in the previous section.

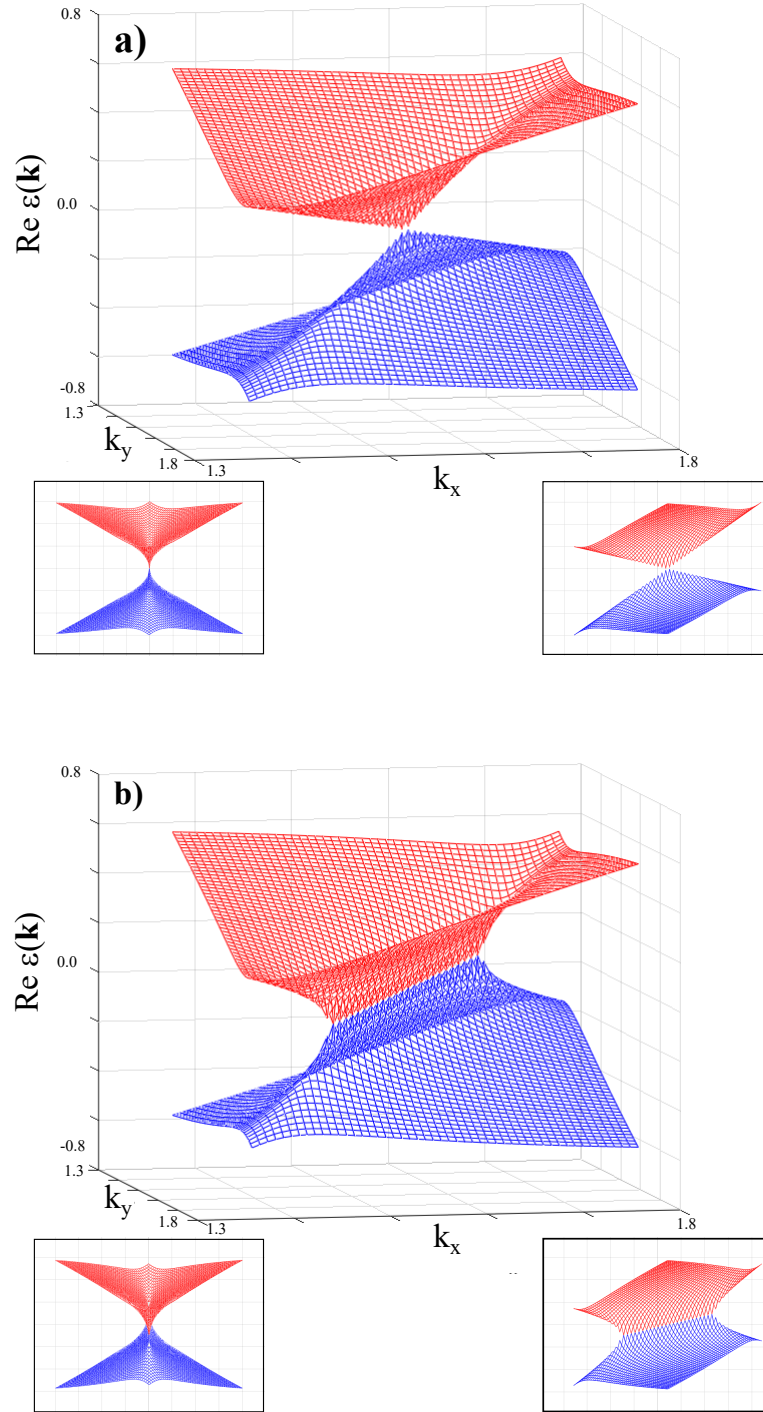Figure 31 – Real part of the bands plotted around the exceptional points centered in $(\pi/2, \pi/2)$. (a) The hybrid exceptional point ($\gamma_z = 2.00$, see Fig. 30c). The insets show the side views of the sheets from the respective corner. One can see a linear dispersion in one direction but a square-root dispersion in the perpendicular direction. (b) A pair of regular exceptional points ($\gamma_z = 2.01$).

8 Conclusion

This thesis reports studies conducted on two-dimensional lattices, focusing on Berry curvature-related effects. The systems studied are quite different from one another. Most of them are magnonic lattices, with different ground state orderings (ferro-, antiferro-, and ferrimagnetic) and various lattice geometries. The systems are approximated as linear spin wave systems, with only harmonic contributions to the Hamiltonian. Additionally, one chapter addresses an electronic tight-binding model with a non-Hermitian Hamiltonian. Despite this diversity, all systems have two-band dispersion and exhibit transverse transport of (quasi-)particles, and some display non-trivial topology. This chapter summarizes the results of each study, drawing connections and comparisons between them to elucidate the role of theoretical parameters in the transverse transport of particles.

A magnonic lattice with ferromagnetic ordering was studied in Chapter 3. The geometry is that of a "modified Lieb lattice", with one lattice site missing. The energy spectrum shows a pair of gapped bands. The variation of the exchange anisotropy parameter λ reveals two topological Chern phases: a trivial phase ($C = 0$ for both bands) when $\lambda > 1$, and a non-trivial phase ($C = \pm 1$) when $\lambda < 1$ (the system is a topological magnon insulator). When $\lambda = 1$ the band gap vanishes, as expected for topological phase transitions. The existence of the Berry curvature is dependent on the Dzyaloshinskii-Moriya interaction (DMI), as it is common for magnonic lattices. High DMI parameter enhances the transverse transport, and this behavior is ubiquitous for all magnonic systems studied here. The transverse transport coefficients behave as expected for different temperatures, resembling other ferromagnetic magnonic systems.

In Chapter 4 and 5, antiferromagnetic magnons were studied in the Union Jack and brick-wall lattices with Néel order, respectively. The formalism for AFM magnons is fundamentally different from FM ones, and involves the construction of a bosonic Bogoliubov-de Gennes Hamiltonian with particle-hole symmetry. Usually, an AFM magnon lattice has two degenerate bands, which is a consequence of an effective time-reversal symmetry (ETRS). This symmetry is broken in the Union Jack lattice by the alternate NNN exchange interaction, and the bands split. A detailed study of the bands' dependency on the parameters was made. The DMI generates a non-null Berry curvature, which enables transverse transport. The dependence of the transport coefficients on the temperature is monotonic. In that Union Jack lattice, the anharmonic contributions were included with a self-consistent mean-field approach, and the transport coefficients were enhanced by magnon-magnon interactions. At some definite temperature, the Néel order becomes unstable, signalling a transition to a disordered phase.

Concerning the AFM brick-wall lattice, the effective time-reversal symmetry is broken by a difference in the single-ion anisotropy on each lattice site. In this geometry, differently from the Union Jack lattice, the thermal Hall conductivity is not monotonic with the temperature, but peakes for some temperature and approaches zero in the high-temperature limit. In the case of degenerate bands, the spin Hall conductivity and thermal Hall conductivity are zero, but the spin Nernst coefficient is not, realizing a pure spin Nernst effect. In that case, the ETRS could be identified as a combination of time-reversal, half-lattice translation and rotation of π around the off-plane axis. Another fundamental difference from the Union Jack lattice is the role of the DMI in the transverse transport. In that lattice, the DMI generates the Berry curvature. But in the brick-wall lattice, the Berry curvature is non-null even in the absence of DMI, being generated by the complex structure factor of the exchange interaction. That is a feature of the brick-wall geometry. Nevertheless, the DMI is still necessary for non-null transverse transport. For both Union Jack and brick-wall lattices, the Chern number is zero.

In Chapter 6, a two-band magnonic system is proposed for a predicted Cu_2F_5 layered crystal. The ordering is ferrimagnetic, as the Cu atoms have different spins (1/2 and 1). The formalism is the same as the AFM lattices, with the difference that the magnons can have a different g-factor. The geometry is the same as the modified Lieb lattice studied in Chapter 3. The main feature of this lattice is that, for some combinations of lattice parameters, the spin Hall and thermal Hall conductivities change sign with a change in the temperature. That opens the possibility of controlling the direction of magnon flux with the temperature, which can have applications in magnon spintronics.

The last system discussed in this thesis differs radically from the previous ones, as it is not a magnonic system, but an electronic tight-binding model on a checkerboard lattice, which is a topological insulator. A Berry curvature arises due to a complex phase in the hopping parameter. A distinguishing characteristic of the studied system is that its Hamiltonian is non-Hermitian, a feature of open quantum systems. The complex energy bands are separable for some parameter choices. In this regime, the system exhibits a non-trivial Chern number; however, the Hall conductivity is not quantized, as expected in non-Hermitian systems, where the bulk-edge correspondence is broken. The dependence of the Hall conductivity on the non-Hermitian parameters was investigated. For other parameter choices (high γ_z), the bands touch at exceptional points, where the eigenstates coalesce and the Hamiltonian becomes defective. The vorticity of these points was analyzed, revealing that pairs of exceptional points with opposite vorticity ($\nu = \pm 1/2$) can merge into hybrid exceptional points with zero vorticity. The topological classification of exceptional points based on their vorticity, which depends only on the eigenvalues rather than the eigenstates, is a hallmark of non-Hermitian Hamiltonians.

All systems studied have a feature in common: they are two-band systems, whose

Hamiltonian can be written as a Pauli vector (linear combination of the Pauli matrices and the identity matrix). As all systems are formally equivalent, the same diagonalization method can be applied to all of them, with a slight modification for AFM and FiM systems which demand a generalized Bogoliubov transformation. In all systems, an imaginary term in the Hamiltonian, proportional to σ_y, is necessary for a non-null Berry curvature. For magnons, this imaginary term is originated either by the lattice geometry (in the brick-wall lattice) or the DMI (in the other magnon lattices). In the fermionic checkerboard lattice, the imaginary term comes from the phase of the hopping parameter. This applies to the Hermitian and non-Hermitian versions of the lattice, and the Chern topology is not altered by the non-Hermiticity. All the investigations reported in this thesis shed light on the transverse transport and topology-related effects in two-dimensional, two-band systems. Those findings point to potential applications in spintronics, in the case of magnons, as well as in electronic transport in open systems, exemplified by the non-Hermitian checkerboard lattice.

Bibliography

[1]   Klitzing, K. von, G. Dorda e M. Pepper: *New method for high-accuracy determination of the fine-structure constant based on quantized Hall resistance.* Phys. Rev. Lett., 45:494–497, Aug 1980. `https://link.aps.org/doi/10.1103/PhysRevLett.45.494`.

[2]   Thouless, D. J., M. Kohmoto, M. P. Nightingale e M. den Nijs: *Quantized Hall conductance in a two-dimensional periodic potential.* Phys. Rev. Lett., 49:405–408, Aug 1982. `https://link.aps.org/doi/10.1103/PhysRevLett.49.405`.

[3]   Kohmoto, Mahito: *Topological invariant and the quantization of the Hall conductance.* Ann. Phys., 160(2):343–354, 1985, ISSN 0003-4916. `https://www.sciencedirect.com/science/article/pii/0003491685901484`.

[4]   Hatsugai, Yasuhiro: *Chern number and edge states in the integer quantum Hall effect.* Phys. Rev. Lett., 71:3697–3700, Nov 1993. `https://link.aps.org/doi/10.1103/PhysRevLett.71.3697`.

[5]   Nagaosa, Naoto: *Anomalous Hall effect - A new perspective.* J. Phys. Soc. Jpn., 75(4):042001, 2006.

[6]   Haldane, F. D. M.: *Model for a quantum Hall effect without Landau levels: Condensed-matter eealization of the "parity anomaly".* Phys. Rev. Lett., 61(18):2015–2018, outubro 1988. `https://doi.org/10.1103/physrevlett.61.2015`.

[7]   Hirsch, J. E.: *Spin Hall effect.* Phys. Rev. Lett., 83:1834–1837, Aug 1999. `https://link.aps.org/doi/10.1103/PhysRevLett.83.1834`.

[8]   Murakami, Shuichi, Naoto Nagaosa e Shou Cheng Zhang: *Dissipationless quantum spin current at room temperature.* Science, 301(5638):1348–1351, 2003.

[9]   Sinova, Jairo, Dimitrie Culcer, Q. Niu, N. A. Sinitsyn, T. Jungwirth e A. H. MacDonald: *Universal intrinsic spin Hall effect.* Phys. Rev. Lett., 92:126603, Mar 2004. `https://link.aps.org/doi/10.1103/PhysRevLett.92.126603`.

[10]   Kane, C. L. e E. J. Mele: *Quantum spin Hall effect in graphene.* Phys. Rev. Lett., 95:226801, Nov 2005. `https://link.aps.org/doi/10.1103/PhysRevLett.95.226801`.

[11]   Kane, C. L. e E. J. Mele: $\mathbb{Z}_2$ *topological order and the quantum spin Hall effect.* Phys. Rev. Lett., 95(14), setembro 2005. `https://doi.org/10.1103/physrevlett.95.146802`.

[12]   Bernevig, B. Andrei e Shou Cheng Zhang: *Quantum spin Hall effect.* Phys. Rev. Lett., 96:106802, Mar 2006. `https://link.aps.org/doi/10.1103/PhysRevLett.96.106802`.

[13]   Hasan, M. Z. e C. L. Kane: *Colloquium: topological insulators.* Rev. Mod. Phys., 82(4):3045–3067, novembro 2010, ISSN 1539-0756. `http://dx.doi.org/10.1103/RevModPhys.82.3045`.

[14]   Fruchart, Michel e David Carpentier: *An introduction to topological insulators.* C. R. Phys., 14(9-10):779–815, outubro 2013, ISSN 1878-1535. `http://dx.doi.org/10.1016/j.crhy.2013.09.013`.

[15]   Xiao, Di, Ming Che Chang e Qian Niu: *Berry phase effects on electronic properties.* Rev. Mod. Phys., 82(3):1959–2007, julho 2010. `https://doi.org/10.1103/revmodphys.82.1959`.

[16]   Pires, Antonio Sergio Teixeira: *A brief introduction to topology and differential geometry in condensed matter physics.* IOP Concise Physics. Morgan & Claypool, San Rafael, CA, março 2019.

[17]   Chumak, A. V., V. I. Vasyuchka, A. A. Serga e B. Hillebrands: *Magnon spintronics.* Nat. Phys., 11(6):453–461, junho 2015. `https://doi.org/10.1038/nphys3347`.

[18]   Ghader, Doried: *Insights on magnon topology and valley-polarization in 2D bilayer quantum magnets.* New J. Phys., 23(5):053022, may 2021. `https://doi.org/10.1088/1367-2630/abfa62`.

[19]   Nakata, Kouki, Jelena Klinovaja e Daniel Loss: *Magnonic quantum Hall effect and Wiedemann-Franz law.* Phys. Rev. B, 95:125429, Mar 2017. `https://link.aps.org/doi/10.1103/PhysRevB.95.125429`.

[20]   Nakata, Kouki, Se Kwon Kim, Jelena Klinovaja e Daniel Loss: *Magnonic topological insulators in antiferromagnets.* Phys. Rev. B, 96:224414, Dec 2017. `https://link.aps.org/doi/10.1103/PhysRevB.96.224414`.

[21]   Aharonov, Y. e D. Bohm: *Significance of electromagnetic potentials in the quantum theory.* Phys. Rev., 115:485–491, Aug 1959. `https://link.aps.org/doi/10.1103/PhysRev.115.485`.

[22]   Aharonov, Y. e A. Casher: *Topological quantum effects for neutral particles.* Phys. Rev. Lett., 53:319–321, Jul 1984. `https://link.aps.org/doi/10.1103/PhysRevLett.53.319`.

[23] Meier, Florian e Daniel Loss: *Magnetization transport and quantized spin conductance.* Phys. Rev. Lett., 90(16), abril 2003, ISSN 1079-7114. `http://dx.doi.org/10.1103/PhysRevLett.90.167204`.

[24] Katsura, Hosho, Naoto Nagaosa e Patrick A. Lee: *Theory of the thermal Hall effect in quantum magnets.* Phys. Rev. Lett., 104:066403, Feb 2010. `https://link.aps.org/doi/10.1103/PhysRevLett.104.066403`.

[25] Onose, Y., T. Ideue, H. Katsura, Y. Shiomi, N. Nagaosa e Y. Tokura: *Observation of the magnon Hall effect.* Science, 329(5989):297–299, 2010.

[26] Matsumoto, Ryo e Shuichi Murakami: *Theoretical Prediction of a Rotating Magnon Wave Packet in Ferromagnets.* Phys. Rev. Lett., 106(19):197202, 2011. `https://doi.org/10.1103/physrevlett.106.197202`.

[27] Matsumoto, Ryo e Shuichi Murakami: *Rotational motion of magnons and the thermal Hall effect.* Phys. Rev. B, 84(18), novembro 2011, ISSN 1550-235X. `http://dx.doi.org/10.1103/physrevb.84.184406`.

[28] Matsumoto, Ryo, Ryuichi Shindou e Shuichi Murakami: *Thermal Hall effect of magnons in magnets with dipolar interaction.* Phys. Rev. B, 89:054420, 2014. `https://link.aps.org/doi/10.1103/PhysRevB.89.054420`.

[29] Xiao, Di, Yugui Yao, Zhong Fang e Qian Niu: *Berry-phase effect in anomalous thermoelectric transport.* Phys. Rev. Lett., 97:026603, Jul 2006. `https://link.aps.org/doi/10.1103/PhysRevLett.97.026603`.

[30] Hoogdalem, Kevin A. van, Yaroslav Tserkovnyak e Daniel Loss: *Magnetic texture-induced thermal Hall effects.* Phys. Rev. B, 87:024402, Jan 2013. `https://link.aps.org/doi/10.1103/PhysRevB.87.024402`.

[31] Lee, Hyunyong, Jung Hoon Han e Patrick A. Lee: *Thermal Hall effect of spins in a paramagnet.* Phys. Rev. B, 91:125413, Mar 2015. `https://link.aps.org/doi/10.1103/PhysRevB.91.125413`.

[32] Han, Jung Hoon e Hyunyong Lee: *Spin chirality and Hall-like transport phenomena of spin excitations.* J. Phys. Soc. Jpn., 86(1):011007, 2017. `https://doi.org/10.7566/jpsj.86.011007`.

[33] Park, Sungjoon, Naoto Nagaosa e Bohm Jung Yang: *Thermal Hall effect, spin Nernst effect, and spin density induced by a thermal gradient in collinear ferrimagnets from magnon-phonon interaction.* Nano Lett., 20(4):2741–2746, fevereiro 2020. `https://doi.org/10.1021/acs.nanolett.0c00363`.

[34] Kajiwara, Y., K. Harii, S. Takahashi, J. Ohe, K. Uchida, M. Mizuguchi, H. Ume-zawa, H. Kawai, K. Ando, K. Takanashi, S. Maekawa e E. Saitoh: *Transmission of electrical signals by spin-wave interconversion in a magnetic insulator.* Nature, 464(7286):262–266, março 2010, ISSN 1476-4687. `http://dx.doi.org/10.1038/nature08876`.

[35] Althammer, Matthias: *All-electrical magnon transport experiments in magnetically ordered insulators.* Phys. Status Solidi RRL, 15(8), junho 2021, ISSN 1862-6270. `http://dx.doi.org/10.1002/pssr.202100130`.

[36] Ideue, T., Y. Onose, H. Katsura, Y. Shiomi, S. Ishiwata, N. Nagaosa e Y. Tokura: *Effect of lattice geometry on magnon Hall effect in ferromagnetic insulators.* Phys. Rev. B, 85:134411, Apr 2012. `https://link.aps.org/doi/10.1103/PhysRevB.85.134411`.

[37] Hirschberger, Max, Robin Chisnell, Young S. Lee e N. P. Ong: *Thermal Hall effect of spin excitations in a kagome magnet.* Phys. Rev. Lett., 115:106603, Sep 2015. `https://link.aps.org/doi/10.1103/PhysRevLett.115.106603`.

[38] Hirschberger, Max, Jason W. Krizan, R. J. Cava e N. P. Ong: *Large thermal Hall conductivity of neutral spin excitations in a frustrated quantum magnet.* Science, 348(6230):106–109, abril 2015. `https://doi.org/10.1126/science.1257340`.

[39] Chisnell, R., J. S. Helton, D. E. Freedman, D. K. Singh, F. Demmel, C. Stock, D. G. Nocera e Y. S. Lee: *Magnetic transitions in the topological magnon insulator Cu(1, 3-bdc).* Phys. Rev. B, 93(21), junho 2016, ISSN 2469-9969. `http://dx.doi.org/10.1103/PhysRevB.93.214403`.

[40] Shiomi, Y., R. Takashima e E. Saitoh: *Experimental evidence consistent with a magnon Nernst effect in the antiferromagnetic insulator $MnPSe_3$.* Physical Review B, 96(13), outubro 2017, ISSN 2469-9969. `http://dx.doi.org/10.1103/PhysRevB.96.134425`.

[41] Zhang, Hantao e Ran Cheng: *A perspective on magnon spin Nernst effect in antiferromagnets.* Appl. Phys. Lett., 120(9):090502, 2022. `https://doi.org/10.1063/5.0084359`.

[42] Ashida, Yuto, Zongping Gong e Masahito Ueda: *Non-Hermitian physics.* Adv. Phys., 69(3):249–435, julho 2020, ISSN 1460-6976. `http://dx.doi.org/10.1080/00018732.2021.1876991`.

[43] Tlusty, Tsvi: *Exceptional topology in ordinary soft matter.* Phys. Rev. E, 104(2), agosto 2021, ISSN 2470-0053. `http://dx.doi.org/10.1103/PhysRevE.104.025002`.

[44] Hurst, Hilary M. e Benedetta Flebus: *Non-Hermitian physics in magnetic systems.* J. Appl. Phys., 132(22), dezembro 2022, ISSN 1089-7550. `http://dx.doi.org/10.1063/5.0124841`.

[45] Banerjee, Ayan, Ronika Sarkar, Soumi Dey e Awadhesh Narayan: *Non-Hermitian topological phases: principles and prospects.* J. Phys.: Condens. Matter, 35(33):333001, maio 2023, ISSN 1361-648X. `http://dx.doi.org/10.1088/1361-648X/acd1cb`.

[46] Yu, Tao, Ji Zou, Bowen Zeng, J.W. Rao e Ke Xia: *Non-Hermitian topological magnonics.* Phys. Rep., 1062:1–86, abril 2024, ISSN 0370-1573. `http://dx.doi.org/10.1016/j.physrep.2024.01.006`.

[47] Lee, Ching Hua e Ronny Thomale: *Anatomy of skin modes and topology in non-Hermitian systems.* Phys. Rev. B, 99(20), maio 2019, ISSN 2469-9969. `http://dx.doi.org/10.1103/PhysRevB.99.201103`.

[48] Zhong, Janet, Kai Wang, Yubin Park, Viktar Asadchy, Charles C. Wojcik, Avik Dutt e Shanhui Fan: *Nontrivial point-gap topology and non-Hermitian skin effect in photonic crystals.* Phys. Rev. B, 104(12), setembro 2021, ISSN 2469-9969. `http://dx.doi.org/10.1103/PhysRevB.104.125416`.

[49] Zhang, Xiujuan, Yuan Tian, Jian Hua Jiang, Ming Hui Lu e Yan Feng Chen: *Observation of higher-order non-Hermitian skin effect.* Nat. Commun., 12(1), setembro 2021, ISSN 2041-1723. `http://dx.doi.org/10.1038/s41467-021-25716-y`.

[50] Dembowski, C., H. D. Gräf, H. L. Harney, A. Heine, W. D. Heiss, H. Rehfeld e A. Richter: *Experimental observation of the topological structure of exceptional points.* Phys. Rev. Lett., 86(5):787–790, janeiro 2001, ISSN 1079-7114. `http://dx.doi.org/10.1103/PhysRevLett.86.787`.

[51] Dembowski, C., B. Dietz, H. D. Gräf, H. L. Harney, A. Heine, W. D. Heiss e A. Richter: *Observation of a chiral state in a microwave cavity.* Phys. Rev. Lett., 90(3), janeiro 2003, ISSN 1079-7114. `http://dx.doi.org/10.1103/PhysRevLett.90.034101`.

[52] Heiss, W D: *The physics of exceptional points.* J. Phys. A, 45(44):444016, outubro 2012, ISSN 1751-8121. `http://dx.doi.org/10.1088/1751-8113/45/44/444016`.

[53] Zhen, Bo, Chia Wei Hsu, Yuichi Igarashi, Ling Lu, Ido Kaminer, Adi Pick, Song Liang Chua, John D. Joannopoulos e Marin Soljačić: *Spawning rings of exceptional points out of Dirac cones.* Nature, 525(7569):354–358, setembro 2015, ISSN 1476-4687. `http://dx.doi.org/10.1038/nature14889`.

[54] Zhang, Dengke, Xiao Qing Luo, Yi Pu Wang, Tie Fu Li e J. Q. You: *Observation of the exceptional point in cavity magnon-polaritons.* Nat. Commun., 8(1), novembro 2017, ISSN 2041-1723. `http://dx.doi.org/10.1038/s41467-017-01634-w`.

[55] Zhou, Hengyun, Chao Peng, Yoseob Yoon, Chia Wei Hsu, Keith A. Nelson, Liang Fu, John D. Joannopoulos, Marin Soljačić e Bo Zhen: *Observation of bulk Fermi arc and polarization half charge from paired exceptional points.* Science, 359(6379):1009–1012, março 2018, ISSN 1095-9203. `http://dx.doi.org/10.1126/science.aap9859`.

[56] Chen, Yu e Hui Zhai: *Hall conductance of a non-Hermitian Chern insulator.* Phys. Rev. B, 98(24), dezembro 2018, ISSN 2469-9969. `http://dx.doi.org/10.1103/PhysRevB.98.245130`.

[57] Hirsbrunner, Mark R., Timothy M. Philip e Matthew J. Gilbert: *Topology and observables of the non-Hermitian Chern insulator.* Phys. Rev. B, 100(8), agosto 2019, ISSN 2469-9969. `http://dx.doi.org/10.1103/PhysRevB.100.081104`.

[58] Yao, Shunyu, Fei Song e Zhong Wang: *Non-Hermitian Chern bands.* Phy. Rev. Lett., 121(13), setembro 2018, ISSN 1079-7114. `http://dx.doi.org/10.1103/PhysRevLett.121.136802`.

[59] Yao, Shunyu e Zhong Wang: *Edge states and topological invariants of non-Hermitian systems.* Phys. Rev. Lett., 121(8), agosto 2018, ISSN 1079-7114. `http://dx.doi.org/10.1103/PhysRevLett.121.086803`.

[60] Yang, Xiaosen, Yang Cao e Yunjia Zhai: *Non-Hermitian Weyl semimetals: non-Hermitian skin effect and non-Bloch bulk–boundary correspondence.* Chinese Phys. B, 31(1):010308, janeiro 2022, ISSN 1674-1056. `http://dx.doi.org/10.1088/1674-1056/ac3738`.

[61] Dey, Soumi, Ayan Banerjee, Debashree Chowdhury e Awadhesh Narayan: *Hall conductance of a non-Hermitian Weyl semimetal.* New J. Phys., 26(2):023057, fevereiro 2024, ISSN 1367-2630. `http://dx.doi.org/10.1088/1367-2630/ad2b0e`.

[62] Ryu, Shinsei, Andreas P Schnyder, Akira Furusaki e Andreas W W Ludwig: *Topological insulators and superconductors: tenfold way and dimensional hierarchy.* New J. Phys., 12(6):065010, junho 2010, ISSN 1367-2630. `http://dx.doi.org/10.1088/1367-2630/12/6/065010`.

[63] Qi, Xiao Liang e Shou Cheng Zhang: *Topological insulators and superconductors.* Rev. Mod. Phys., 83(4):1057–1110, outubro 2011, ISSN 1539-0756. `http://dx.doi.org/10.1103/RevModPhys.83.1057`.

[64] Süsstrunk, Roman e Sebastian D. Huber: *Observation of phononic helical edge states in a mechanical topological insulator.* Science, 349(6243):47–50, julho 2015, ISSN 1095-9203. `http://dx.doi.org/10.1126/science.aab0239`.

[65] Goldman, N., J. C. Budich e P. Zoller: *Topological quantum matter with ultracold gases in optical lattices*. Nature Phys., 12(7):639–645, junho 2016, ISSN 1745-2481. `http://dx.doi.org/10.1038/nphys3803`.

[66] Ozawa, Tomoki, Hannah M. Price, Alberto Amo, Nathan Goldman, Mohammad Hafezi, Ling Lu, Mikael C. Rechtsman, David Schuster, Jonathan Simon, Oded Zilberberg e Iacopo Carusotto: *Topological photonics*. Rev. Mod. Phys., 91(1), março 2019, ISSN 1539-0756. `http://dx.doi.org/10.1103/RevModPhys.91.015006`.

[67] Malki, M. e G. S. Uhrig: *Topological magnetic excitations*. EPL, 132(2):20003, outubro 2020, ISSN 1286-4854. `http://dx.doi.org/10.1209/0295-5075/132/20003`.

[68] Luttinger, J. M.: *Theory of thermal transport coefficients*. Phys. Rev., 135:A1505–A1514, Sep 1964. `https://link.aps.org/doi/10.1103/PhysRev.135.A1505`.

[69] Smrcka, L e P Streda: *Transport coefficients in strong magnetic fields*. J. Phys. C: Solid State Phys., 10(12):2153–2161, junho 1977, ISSN 0022-3719. `http://dx.doi.org/10.1088/0022-3719/10/12/021`.

[70] Oji, Herbert e P. Streda: *Theory of electronic thermal transport: magnetoquantum corrections to the thermal transport coefficients*. Phys. Rev. B, 31(11):7291–7295, junho 1985, ISSN 0163-1829. `http://dx.doi.org/10.1103/PhysRevB.31.7291`.

[71] Bergman, Doron L. e Vadim Oganesyan: *Theory of dissipationless Nernst effects*. Phys. Rev. Lett., 104(6), fevereiro 2010, ISSN 1079-7114. `http://dx.doi.org/10.1103/PhysRevLett.104.066601`.

[72] Kondo, Hiroki e Yutaka Akagi: *Nonlinear magnon spin Nernst effect in antiferromagnets and strain-tunable pure spin current*. Phys. Rev. Research, 4:013186, Mar 2022. `https://link.aps.org/doi/10.1103/PhysRevResearch.4.013186`.

[73] Nakata, Kouki e Se Kwon Kim: *Topological Hall effects of magnons in ferrimagnets*. J. Phys. Soc. Jpn., 90(8):081004, agosto 2021, ISSN 1347-4073. `http://dx.doi.org/10.7566/JPSJ.90.081004`.

[74] Oliveira, P. G. de e A. S. T. Pires: *Transversal transport of magnons in a modified Lieb lattice*. Physica B, 654:414721, abril 2023. `https://doi.org/10.1016/j.physb.2023.414721`.

[75] Owerre, S A: *A first theoretical realization of honeycomb topological magnon insulator*. J. Phys.: Condens. Matter, 28(38):386001, jul 2016. `https://doi.org/10.1088/0953-8984/28/38/386001`.

[76] Owerre, S. A.: *Topological honeycomb magnon Hall effect: a calculation of thermal Hall conductivity of magnetic spin excitations*. J. Appl. Phys., 120(4):043903, 2016.

[77] Kim, Se Kwon, Héctor Ochoa, Ricardo Zarzuela e Yaroslav Tserkovnyak: *Realization of the Haldane-Kane-Mele model in a system of localized spins.* Phys. Rev. Lett., 117(22):227201, 2016. `https://doi.org/10.1103/physrevlett.117.227201`.

[78] Mook, Alexander, Jurgen Henk e Ingrid Mertig: *Magnon Hall effect and topology in kagome lattices: A theoretical investigation.* Phys. Rev. B, 89:134409, Apr 2014. `https://link.aps.org/doi/10.1103/PhysRevB.89.134409`.

[79] Kovalev, Alexey A. e Vladimir Zyuzin: *Spin torque and Nernst effects in Dzyaloshinskii-Moriya ferromagnets.* Phys. Rev. B, 93:161106, 2016. `https://link.aps.org/doi/10.1103/PhysRevB.93.161106`.

[80] Laurell, Pontus e Gregory A. Fiete: *Magnon thermal Hall effect in kagome antiferromagnets with Dzyaloshinskii-Moriya interactions.* Phys. Rev. B, 98:094419, Sep 2018. `https://link.aps.org/doi/10.1103/PhysRevB.98.094419`.

[81] Malki, M. e G. S. Uhrig: *Topological magnon bands for magnonics.* Phys. Rev. B, 99:174412, May 2019. `https://link.aps.org/doi/10.1103/PhysRevB.99.174412`.

[82] Bhowmick, Dhiman e Pinaki Sengupta: *Topological magnon bands in the flux state of Shastry-Sutherland lattice model.* Phys. Rev. B, 101(21), junho 2020. `https://doi.org/10.1103/physrevb.101.214403`.

[83] Kawano, Masataka e Chisa Hotta: *Thermal Hall effect and topological edge states in a square-lattice antiferromagnet.* Phys. Rev. B, 99:054422, feb 2019. `https://link.aps.org/doi/10.1103/PhysRevB.99.054422`.

[84] Canals, Benjamin: *From the square lattice to the checkerboard lattice: spin-wave and large-n limit analysis.* Phys. Rev. B, 65(18), abril 2002, ISSN 1095-3795. `http://dx.doi.org/10.1103/PhysRevB.65.184408`.

[85] Bernier, Jean Sebastien, Chung Hou Chung, Yong Kim e Subir Sachdev: *Planar pyrochlore antiferromagnet: A large-N analysis.* Phys. Rev. B, 69:214427, outubro 2003.

[86] Pires, A.S.T.: *Magnon spin Nernst effect on the antiferromagnetic checkerboard lattice.* Phys. Lett. A, 383(32):125887, novembro 2019, ISSN 0375-9601. `http://dx.doi.org/10.1016/j.physleta.2019.125887`.

[87] Pires, A. S. T.: *Topological magnons on the checkerboard lattice.* Physica B, 602:412490, 2021. `https://www.sciencedirect.com/science/article/pii/S0921452620304907`.

[88] Pires, A. S. T.: *Topological magnons in the antiferromagnetic checkerboard lattice.* Physica E, 118:113899, abril 2020. `https://doi.org/10.1016/j.physe.2019.113899`.

[89] Zhang, Zhiqin, Wenhui Feng, Yingbo Yao e Bing Tang: *Photoinduced Floquet topological magnons in a ferromagnetic checkerboard lattice.* Phys. Lett. A, 414:127630, outubro 2021, ISSN 0375-9601. `http://dx.doi.org/10.1016/j.physleta.2021.127630`.

[90] Cao, Xiaodong, Kai Chen e Dahai He: *Magnon Hall effect on the Lieb lattice.* J. Phys.: Condens. Matter, 27(16):166003, 2015. `https://doi.org/10.1088/0953-8984/27/16/166003`.

[91] Kambe, Shiro e Osamu Ishii: *Correlation between T_c, in-plane CuOCu bond length, and buckling of the CuO_2 plane in cuprate superconductors.* Physica C, 341-348:555–556, novembro 2000. `https://doi.org/10.1016/s0921-4534(00)00589-x`.

[92] Jiang, Wei, Shunhong Zhang, Zhengfei Wang, Feng Liu e Tony Low: *Topological band engineering of Lieb lattice in phthalocyanine-based metal–organic frameworks.* Nano Lett., 20(3):1959–1966, fevereiro 2020, ISSN 1530-6992. `http://dx.doi.org/10.1021/acs.nanolett.9b05242`.

[93] Herring, Conyers e Charles Kittel: *On the theory of spin waves in ferromagnetic media.* Phys. Rev., 81(5):869–880, março 1951. `https://doi.org/10.1103/physrev.81.869`.

[94] Bruno, Patrick: *Spin-wave theory of two-dimensional ferromagnets in the presence of dipolar interactions and magnetocrystalline anisotropy.* Phys. Rev. B, 43(7):6015–6021, março 1991. `https://doi.org/10.1103/physrevb.43.6015`.

[95] Holstein, T. e H. Primakoff: *Field dependence of the intrinsic domain magnetization of a ferromagnet.* Phys. Rev., 58:1098–1113, Dec 1940. `https://link.aps.org/doi/10.1103/PhysRev.58.1098`.

[96] Mermin, N. D. e H. Wagner: *Absence of ferromagnetism or antiferromagnetism in one- or two-dimensional isotropic Heisenberg models.* Phys. Rev. Lett., 17:1133–1136, Nov 1966. `https://link.aps.org/doi/10.1103/PhysRevLett.17.1133`.

[97] Owerre, S. A.: *A first theoretical realization of honeycomb topological magnon insulator.* J. Phys.: Condens. Matter, 28(38):386001, 2016. `https://doi.org/10.1088/0953-8984/28/38/386001`.

[98] Baltz, V., A. Manchon, M. Tsoi, T. Moriyama, T. Ono e Y. Tserkovnyak: *Antiferromagnetic spintronics.* Rev. Mod. Phys., 90:015005, Feb 2018. `https://link.aps.org/doi/10.1103/RevModPhys.90.015005`.

[99] Jungwirth, T., J. Sinova, A. Manchon, X. Marti, J. Wunderlich e C. Felser: *The multiple directions of antiferromagnetic spintronics.* Nat. Phys., 14(3):200–203, março 2018. https://doi.org/10.1038/s41567-018-0063-6.

[100] Bonbien, V, Fengjun Zhuo, A Salimath, O Ly, A Abbout e A Manchon: *Topological aspects of antiferromagnets.* J. Phys. D: Appl. Phys., 55(10):103002, novembro 2021. https://doi.org/10.1088/1361-6463/ac28fa.

[101] Zhang, Yinhan, Satoshi Okamoto e Di Xiao: *Spin-Nernst effect in the paramagnetic regime of an antiferromagnetic insulator.* Phys. Rev. B, 98(3), julho 2018. https://doi.org/10.1103/physrevb.98.035424.

[102] Kim, Kyung Su, Ki Hoon Lee, Suk Bum Chung e Je Geun Park: *Magnon topology and thermal Hall effect in trimerized triangular lattice antiferromagnet.* Phys. Rev. B, 100(6), agosto 2019. https://doi.org/10.1103/physrevb.100.064412.

[103] Li, Bo, Shane Sandhoefner e Alexey A. Kovalev: *Intrinsic spin Nernst effect of magnons in a noncollinear antiferromagnet.* Phys. Rev. Res., 2:013079, Jan 2020. https://link.aps.org/doi/10.1103/PhysRevResearch.2.013079.

[104] Romhányi, Judit, Karlo Penc e R. Ganesh: *Hall effect of triplons in a dimerized quantum magnet.* Nat. Commun., 6(1), abril 2015. https://doi.org/10.1038/ncomms7805.

[105] McClarty, P. A., F. Krüger, T. Guidi, S. F. Parker, K. Refson, A. W. Parker, D. Prabhakaran e R. Coldea: *Topological triplon modes and bound states in a Shastry-Sutherland magnet.* Nat. Phys., 13(8):736–741, maio 2017. https://doi.org/10.1038/nphys4117.

[106] Bhowmick, Dhiman e Pinaki Sengupta: *Weyl triplons in $SrCu_2((BO_3)_2)$.* Phys. Rev. B, 104(8), agosto 2021. https://doi.org/10.1103/physrevb.104.085121.

[107] Oliveira, P. G. de e A. S. T. Pires: *Magnon Hall effect in antiferromagnetic lattices.* J. Magn. Magn. Mater., 583:171043, outubro 2023. https://doi.org/10.1016/j.jmmm.2023.171043.

[108] Rezende, Sergio M., Antonio Azevedo e Roberto L. Rodríguez-Suárez: *Introduction to antiferromagnetic magnons.* J. Appl. Phys., 126(15):151101, 2019.

[109] Colpa, J.H.P.: *Diagonalization of the quadratic boson Hamiltonian.* Physica A, 93(3-4):327–353, setembro 1978. https://doi.org/10.1016/0378-4371(78)90160-7.

[110] Kondo, Hiroki, Yutaka Akagi e Hosho Katsura: *Non-Hermiticity and topological invariants of magnon Bogoliubov–de Gennes systems.* Prog. Theor. Exp. Phys.,

2020(12):12A104, outubro 2020, ISSN 2050-3911. `https://doi.org/10.1093/ptep/ptaa151`.

[111] Mostafazadeh, Ali: *Pseudounitary operators and pseudounitary quantum dynamics.* J. Math. Phys., 45(3):932–946, março 2004, ISSN 1089-7658. `http://dx.doi.org/10.1063/1.1646448`.

[112] Mostafazadeh, Ali: *Pseudo-Hermiticity versus PT symmetry: The necessary condition for the reality of the spectrum of a non-Hermitian Hamiltonian.* J. Math. Phys., 43(1):205–214, janeiro 2002, ISSN 1089-7658. `http://dx.doi.org/10.1063/1.1418246`.

[113] Lieu, Simon: *Topological symmetry classes for non-Hermitian models and connections to the bosonic Bogoliubov–de Gennes equation.* Phys. Rev. B, 98(11), setembro 2018, ISSN 2469-9969. `http://dx.doi.org/10.1103/PhysRevB.98.115135`.

[114] Samajdar, Rhine, Shubhayu Chatterjee, Subir Sachdev e Mathias S. Scheurer: *Thermal Hall effect in square-lattice spin liquids: A Schwinger boson mean-field study.* Phys. Rev. B, 99(16):165126, abril 2019. `https://doi.org/10.1103/physrevb.99.165126`.

[115] Cheng, Ran, Satoshi Okamoto e Di Xiao: *Spin Nernst effect of magnons in collinear antiferromagnets.* Phys. Rev. Lett., 117(21):217202, 2016. `https://doi.org/10.1103/physrevlett.117.217202`.

[116] Kondo, Hiroki e Yutaka Akagi: *Nonlinear magnon spin Nernst effect in antiferromagnets and strain-tunable pure spin current.* Phys. Rev. Res., 4:013186, Mar 2022. `https://link.aps.org/doi/10.1103/PhysRevResearch.4.013186`.

[117] Zyuzin, Vladimir A. e Alexey A. Kovalev: *Magnon spin Nernst effect in antiferromagnets.* Phys. Rev. Lett., 117:217203, Nov 2016. `https://link.aps.org/doi/10.1103/PhysRevLett.117.217203`.

[118] Zhang, Hantao e Ran Cheng: *A perspective on magnon spin Nernst effect in antiferromagnets.* Appl. Phys. Lett., 120(9):090502, fevereiro 2022. `https://doi.org/10.1063/5.0084359`.

[119] Liu, Yuntian, Jiayu Li e Qihang Liu: *Chern-insulator phase in antiferromagnets.* Nano Lett., 23(18):8650–8656, setembro 2023, ISSN 153-6992. `http://dx.doi.org/10.1021/acs.nanolett.3c02489`.

[120] Rybin, Nikita, Dmitry Y. Novoselov, Dmitry M. Korotin, Vladimir I. Anisimov e Artem R. Oganov: *Novel copper fluoride analogs of cuprates.* Phys. Chem. Chem. Phys., 23(30):15989–15993, 2021. `https://doi.org/10.1039/d1cp00657f`.

[121] Korotin, Dmitry M., Dmitry Y. Novoselov, Vladimir I. Anisimov e Artem R. Oganov: *Mixed spin $S = 1$ and $S = 1/2$ layered lattice in Cu_2F_5*. Phys. Rev. B, 104:064410, Aug 2021. `https://link.aps.org/doi/10.1103/PhysRevB.104.064410`.

[122] Korotin, Dmitry M., Dmitry Y. Novoselov e Vladimir I. Anisimov: *Evolution from two- to one-dimensional magnetic interactions in Cu_2F_{5-x} through electron doping by fluoride nonstoichiometry*. Phys. Rev. B, 107:094430, Mar 2023. `https://link.aps.org/doi/10.1103/PhysRevB.107.094430`.

[123] Oliveira, P.G. de e A.S.T. Pires: *Magnon bands and transverse transport in a proposed two-dimensional Cu_2F_5 ferrimagnet*. J. Magn. Magn. Mater., 606:172358, setembro 2024, ISSN 0304-8853. `http://dx.doi.org/10.1016/j.jmmm.2024.172358`.

[124] Oliveira, P. G. de e A. S. T. Pires: *Hall transport in the topological non-Hermitian checkerboard lattice*, 2024. `https://arxiv.org/abs/2407.20296`.

[125] Fujimoto, Satoshi: *Geometrical-frustration-induced (semi)metal-to-insulator transition*. Phys. Rev. Lett., 89:226402, Nov 2002. `https://link.aps.org/doi/10.1103/PhysRevLett.89.226402`.

[126] Bernier, Jean Sébastien, Chung Hou Chung, Yong Baek Kim e Subir Sachdev: *Planar pyrochlore antiferromagnet: A large-N analysis*. Phys. Rev. B, 69(21), junho 2004, ISSN 1550-235X. `http://dx.doi.org/10.1103/PhysRevB.69.214427`.

[127] Pollmann, Frank, Joseph J. Betouras, Kirill Shtengel e Peter Fulde: *Correlated frmions on a checkerboard Lattice*. Phys. Rev. Lett., 97(17), outubro 2006, ISSN 1079-7114. `http://dx.doi.org/10.1103/PhysRevLett.97.170407`.

[128] Yoshioka, Takuya, Akihisa Koga e Norio Kawakami: *Frustration effects in an anisotropic checkerboard lattice Hubbard model*. Phys. Rev. B, 78:165113, Oct 2008. `https://link.aps.org/doi/10.1103/PhysRevB.78.165113`.

[129] Santos, E G, J R Iglesias, C Lacroix e M A Gusmão: *A two-band model for superconductivity in the checkerboard lattice*. J. Phys.: Condens. Matter, 22(21):215701, apr 2010. `https://dx.doi.org/10.1088/0953-8984/22/21/215701`.

[130] Sun, Kai, Hong Yao, Eduardo Fradkin e Steven A. Kivelson: *Topological insulators and nematic phases from spontaneous symmetry breaking in 2D Fermi systems with a quadratic band crossing*. Phys. Rev. Lett., 103:046811, Jul 2009. `https://link.aps.org/doi/10.1103/PhysRevLett.103.046811`.

[131] Sun, Kai, Zhengcheng Gu, Hosho Katsura e S. Das Sarma: *Nearly flatbands with nontrivial topology*. Phys. Rev. Lett., 106(23), junho 2011, ISSN 1079-7114. `http://dx.doi.org/10.1103/PhysRevLett.106.236803`.

[132] Katsura, Hosho, Isao Maruyama, Akinori Tanaka e Hal Tasaki: *Ferromagnetism in the Hubbard model with topological/non-topological flat bands.* Europhys. Lett., 91(5):57007, setembro 2010, ISSN 1286-4854. `http://dx.doi.org/10.1209/0295-5075/91/57007`.

[133] Liu, Hang, Gurjyot Sethi, Sheng Meng e Feng Liu: *Orbital design of flat bands in non-line-graph lattices via line-graph wave functions.* Phys. Rev. B, 105(8), fevereiro 2022, ISSN 2469-9969. `http://dx.doi.org/10.1103/PhysRevB.105.085128`.

[134] Liu, Xiao Ping, Yuan Zhou, Yi Fei Wang e Chang De Gong: *Characterizations of topological superconductors: Chern numbers, edge states and Majorana zero modes.* New J. Phys., 19(9):093018, setembro 2017, ISSN 1367-2630. `http://dx.doi.org/10.1088/1367-2630/aa8022`.

[135] Pires, A.S.T.: *Topological magnons on the checkerboard lattice.* Physica B, 602:412490, fevereiro 2021, ISSN 0921-4526. `http://dx.doi.org/10.1016/j.physb.2020.412490`.

[136] Ma, Da Shuai, Yuanfeng Xu, Christie S. Chiu, Nicolas Regnault, Andrew A. Houck, Zhida Song e B. Andrei Bernevig: *Spin-orbit-induced topological flat bands in line and split graphs of bipartite lattices.* Phys. Rev. Lett., 125:266403, Dec 2020. `https://link.aps.org/doi/10.1103/PhysRevLett.125.266403`.

[137] Kabbour, Houria, Etienne Janod, Benoît Corraze, Michel Danot, Changhoon Lee, Myung Hwan Whangbo e Laurent Cario: *Structure and magnetic properties of oxychalcogenides $A_2F_2Fe_2OQ_2$ (A = Sr, Ba; Q = S, Se) with Fe_2O qquare planar layers representing an antiferromagnetic checkerboard spin lattice.* J. Am. Chem. Soc., 130(26):8261–8270, junho 2008, ISSN 1520-5126. `http://dx.doi.org/10.1021/ja711139g`.

[138] Hu, Xuegao, Run Wu Zhang, Da Shuai Ma, Zhihao Cai, Daiyu Geng, Zhenyu Sun, Qiaoxiao Zhao, Jisong Gao, Peng Cheng, Lan Chen, Kehui Wu, Yugui Yao e Baojie Feng: *Realization of a two-dimensional checkerboard lattice in monolayer Cu_2N.* Nano Lett., 23(12):5610–5616, junho 2023, ISSN 1530-6992. `http://dx.doi.org/10.1021/acs.nanolett.3c01111`.

[139] Sufyan, Ali, Muhammad Sajjad e J. Andreas Larsson: *Evaluating the potential of planar checkerboard lattice Cu_2N monolayer as anode material for lithium and sodium-ion batteries using first-principles methods.* Appl. Surf. Sci., 654:159474, maio 2024, ISSN 0169-4332. `http://dx.doi.org/10.1016/j.apsusc.2024.159474`.

[140] Midtgaard, Jonatan Melkaer, Zhigang Wu e Yu Chen: *Constraints on the energy spectrum of non-Hermitian models in open environments.* Eur. Phys. J. B, 92(11), novembro 2019, ISSN 1434-6036. `http://dx.doi.org/10.1140/epjb/e2019-100393-5`.

[141] Brody, Dorje C: *Biorthogonal quantum mechanics*. J. Phys. A: Math. Theor., 47(3):035305, dezembro 2013, ISSN 1751-8121. `http://dx.doi.org/10.1088/1751-8113/47/3/035305`.

[142] Groenendijk, Solofo, Thomas L. Schmidt e Tobias Meng: *Universal Hall conductance scaling in non-Hermitian Chern insulators*. Phys. Rev. Res., 3(2), abril 2021, ISSN 2643-1564. `http://dx.doi.org/10.1103/PhysRevResearch.3.023001`.

[143] Ishikawa, K. e T. Matsuyama: *Magnetic field induced multi-component QED_3 and quantum Hall effect*. Z. Phys. C - Particles and Fields, 33(1):41–45, março 1986, ISSN 1434-6052. `http://dx.doi.org/10.1007/BF01410451`.

[144] Ishikawa, Kenzo e Toyoki Matsuyama: *A microscopic theory of the quantum Hall effect*. Nucl. Phys. B, 280:523–548, 1987, ISSN 0550-3213. `http://dx.doi.org/10.1016/0550-3213(87)90160-X`.

[145] Philip, Timothy M., Mark R. Hirsbrunner e Matthew J. Gilbert: *Loss of Hall conductivity quantization in a non-Hermitian quantum anomalous Hall insulator*. Phys. Rev. B, 98(15), outubro 2018, ISSN 2469-9969. `http://dx.doi.org/10.1103/PhysRevB.98.155430`.

[146] Pan, Lei, Xin Chen, Yu Chen e Hui Zhai: *Non-Hermitian linear response theory*. Nat. Phys., 16(7):767–771, maio 2020, ISSN 1745-2481. `http://dx.doi.org/10.1038/s41567-020-0889-6`.

[147] Geier, Kevin T. e Philipp Hauke: *From Non-Hermitian linear response to dynamical correlations and fluctuation-dissipation relations in quantum many-body systems*. PRX Quantum, 3(3), julho 2022, ISSN 2691-3399. `http://dx.doi.org/10.1103/PRXQuantum.3.030308`.

[148] Sticlet, Doru, Balázs Dóra e Cătălin Paşcu Moca: *Kubo formula for non-Hermitian systems and tachyon optical conductivity*. Phys. Rev. Lett., 128(1), janeiro 2022, ISSN 1079-7114. `http://dx.doi.org/10.1103/PhysRevLett.128.016802`.

[149] Meden, V, L Grunwald e D M Kennes: *PT-symmetric, non-Hermitian quantum many-body physics — a methodological perspective*. Rep. Prog. Phys., 86(12):124501, novembro 2023, ISSN 1361-6633. `http://dx.doi.org/10.1088/1361-6633/ad05f3`.

[150] Shen, Huitao, Bo Zhen e Liang Fu: *Topological band theory for non-Hermitian Hamiltonians*. Phys. Rev. Lett., 120(14), abril 2018, ISSN 1079-7114. `http://dx.doi.org/10.1103/PhysRevLett.120.146402`.

[151] Zhang, Xu Lin e C. T. Chan: *Hybrid exceptional point and its dynamical encircling in a two-state system*. Phys. Rev. A, 98(3), setembro 2018, ISSN 2469-9934. `http://dx.doi.org/10.1103/PhysRevA.98.033810`.

[152] Jin, L., H. C. Wu, Bo Bo Wei e Z. Song: *Hybrid exceptional point created from type-III Dirac point.* Phys. Rev. B, 101(4), janeiro 2020, ISSN 2469-9969. `http://dx.doi.org/10.1103/PhysRevB.101.045130`.

[153] Shindou, Ryuichi, Ryo Matsumoto, Shuichi Murakami e Junichiro Ohe: *Topological chiral magnonic edge mode in a magnonic crystal.* Phys. Rev. B, 87(17):174427, maio 2013. `https://doi.org/10.1103/physrevb.87.174427`.

Appendix

APPENDIX A – Modified Spin Wave (MSW) approach

Here we explicitly show the inclusion of anharmonic contributions to the Union Jack lattice in the MSW picture, complementing Section 4.3. We start with the Holstein-Primakoff transformation written up to four operator terms:

$$S_i^+ = \sqrt{2S}\left(a_i - \frac{a_i^\dagger a_i a_i}{4S}\right), \quad S_i^- = \sqrt{2S}\left(a_i^\dagger - \frac{a_i^\dagger a_i^\dagger a_i}{4S}\right), \quad S_i^z = S - a_i^\dagger a_i \tag{A.1}$$

on a sublattice A and

$$S_j^+ = \sqrt{2S}\left(b_j^\dagger - \frac{b_j^\dagger b_j^\dagger b_j}{4S}\right), \quad S_j^- = \sqrt{2S}\left(b_j - \frac{b_j^\dagger b_j b_j}{4S}\right), \quad S_j^z = -S + b_j^\dagger b_j \tag{A.2}$$

on sublattice B. Taking (A.1) and (A.2) into Hamiltonian (4.1) we find, neglecting all constant terms:

$$H = H_1 + H_2 + H_{DM} + H_{SIA}, \tag{A.3}$$

where

$$H_1 = J_1 S \sum_{\langle i,j \rangle} \left(a_i^\dagger a_i + b_j^\dagger b_j + a_i b_j + a_i^\dagger b_j^\dagger\right) +$$
$$- \frac{J_1}{4} \sum_{\langle i,j \rangle} \left(a_i b_j^\dagger b_j b_j + a_i^\dagger a_i a_i b_j + a_i^\dagger b_j^\dagger b_j^\dagger b_j + a_i^\dagger a_i^\dagger a_i b_j^\dagger + 4 a_i^\dagger a_i b_j^\dagger b_j\right) \tag{A.4}$$

$$H_2 = S \sum_{\langle\langle i,j \rangle\rangle} J_{2,ij}\left[a_i a_j^\dagger + a_i^\dagger a_j - \lambda\left(a_i^\dagger a_i + a_j^\dagger a_j\right)\right] +$$
$$- \frac{1}{4} \sum_{\langle\langle i,j \rangle\rangle} J_{2,ij}\left(a_i a_j^\dagger a_j^\dagger a_j + a_i^\dagger a_i a_i a_j^\dagger + a_i^\dagger a_j^\dagger a_j a_j + a_i^\dagger a_i^\dagger a_i a_j - 4\lambda a_i^\dagger a_i a_j^\dagger a_j\right) \tag{A.5}$$

$$H_{DM} = iDS \sum_{\langle i,j \rangle} \nu_{ij}\left(a_i b_j - a_i^\dagger b_j^\dagger\right) +$$
$$+ i\frac{D}{4} \sum_{\langle i,j \rangle} \nu_{ij}\left(-a_i b_j^\dagger b_j b_j - a_i^\dagger a_i a_i b_j + a_i^\dagger b_j^\dagger b_j^\dagger b_j + a_i^\dagger a_i^\dagger a_i b_j^\dagger\right) \tag{A.6}$$

$$
\begin{aligned}
H_{SIA} &= 2AS \left(\sum_{i \in A} a_i^\dagger a_i + \sum_{j \in B} b_j^\dagger b_j \right) - A \left(\sum_{i \in A} a_i^\dagger a_i a_i^\dagger a_i + \sum_{j \in B} b_j^\dagger b_j b_j^\dagger b_j \right) \\
&= A \left(2S - 1 \right) \left(\sum_{i \in A} a_i^\dagger a_i + \sum_{j \in B} b_j^\dagger b_j \right) - A \left(\sum_{i \in A} a_i^\dagger a_i^\dagger a_i a_i + \sum_{j \in B} b_j^\dagger b_j^\dagger b_j b_j \right). \quad \text{(A.7)}
\end{aligned}
$$

In the SIA term, we have used $a_i^\dagger a_i a_i^\dagger a_i = a_i^\dagger a_i + a_i^\dagger a_i^\dagger a_i a_i$ (and similarly for the b_j operators) to normal order the quartic terms.

Considering only the quadratic terms on the expressions above, we obtain the linear spin wave theory (LSW) exposed in the main text. We include the quartic terms to consider the interactions between magnons and perform a mean-field decoupling to obtain an effective quadratic Hamiltonian (modified spin theory, MSW). We use the well-known relation between quantum operators (ignoring the zeroth-order terms $\langle AB \rangle \langle CD \rangle$ which only add a global constant energy to the spectrum):

$$
\begin{aligned}
ABCD &= \langle AB \rangle \, CD + AB \, \langle CD \rangle + \langle AC \rangle \, BD \\
&\quad + AC \, \langle BD \rangle + \langle AD \rangle \, BC + AD \, \langle BC \rangle. \quad \text{(A.8)}
\end{aligned}
$$

The only non-null mean-field terms are $\left\langle a_i^\dagger a_j \right\rangle$, $\left\langle b_i^\dagger b_j \right\rangle$, $\langle a_i b_j \rangle$, $\langle b_i a_j \rangle$ and their complex conjugates (see discussion in the end of this Appendix). For instante, the first quartic term in H_1 decouples as:

$$
a_i b_j^\dagger b_j b_j = 2 \left\langle b_j^\dagger b_j \right\rangle a_i b_j + 2 \langle a_i b_j \rangle b_j^\dagger b_j \quad \text{(A.9)}
$$

The mean-field terms are renamed as

$$
\begin{aligned}
g_1 &= \left\langle a_i^\dagger a_i \right\rangle, \quad g_2 = \left\langle b_j^\dagger b_j \right\rangle, \quad g_3 = \langle a_i b_j \rangle, \\
g_4 &= \left\langle a_i^\dagger b_j^\dagger \right\rangle, \quad g_5 = \left\langle a_i^\dagger a_j \right\rangle, \quad g_6 = \left\langle a_i a_j^\dagger \right\rangle. \quad \text{(A.10)}
\end{aligned}
$$

Noting that g_3 and g_4 can be complex, we define G_1 and G_2:

$$
\begin{aligned}
g_3 &= G_1 + iG_2, \quad g_4 = G_1 - iG_2, \\
\Rightarrow g_3 + g_4 &= 2G_1, \quad g_3 - g_4 = 2iG_2. \quad \text{(A.11)}
\end{aligned}
$$

With these definitions, it is possible to write:

$$H_1 + H_{DM} = \sum_{\langle i,j \rangle} \left\{ [J_1 (S - g_2 - G_1) + \nu_{ij} DG_2] \, a_i^\dagger a_i + \right.$$

$$+ [J_1 (S - g_1 - G_1) + \nu_{ij} DG_2] \, b_j^\dagger b_j$$

$$+ J_1 \left(S - \frac{g_1 + g_2}{2} - G_1 \right) \left(a_i b_j + a_i^\dagger b_j^\dagger \right)$$

$$\left. + i \left[J_1 G_2 + \nu_{ij} D \left(S - \frac{g_1 + g_2}{2} \right) \right] \left(a_i b_j - a_i^\dagger b_j^\dagger \right) \right\} \tag{A.12}$$

$$H_2 = \sum_{\langle\langle i,j \rangle\rangle} J_{2,ij} \left[\left(-\frac{g_5 + g_6}{2} - \lambda (S - g_1) \right) \left(a_i^\dagger a_i + a_j^\dagger a_j \right) \right. \tag{A.13}$$

$$\left. + (S - g_1) \left(a_i^\dagger a_j + a_i a_j^\dagger \right) + \lambda \left(g_6 a_i^\dagger a_j + g_5 a_i a_j^\dagger \right) \right]$$

$$H_{SIA} = A \left[(2S - 1) - 4g_1 \right] \sum_{i \in A} a_i^\dagger a_i + A \left[(2S - 1) - 4g_2 \right] \sum_{j \in B} b_j^\dagger b_j. \tag{A.14}$$

Let Γ_i be new parameters defined as:

$$\Gamma_1 = S - \left(\frac{g_1 + g_2}{2} + G_1 \right)$$

$$\Gamma_2 = (S - G_1 - g_2)$$

$$\Gamma_3 = (S - G_1 - g_1)$$

$$\Gamma_4 = S - \frac{g_1 + g_2}{2}$$

$$\Gamma_5 = -\frac{g_5 + g_6}{2} - \lambda (S - g_1)$$

$$\Gamma_6 = (2S - 1) - 4g_1$$

$$\Gamma_7 = (2S - 1) - 4g_2. \tag{A.15}$$

It is possible to rewrite the Hamiltonian in terms of eight temperature dependent parameters: Γ_i and G_2 (not all linearly independent). Fourier transforming and symmetrizing the operators, we get:

$$H_1 + H_{DM} = 2 \sum_k \left[(J_1 \Gamma_2 + m_k DG_2) \left(a_k^\dagger a_k + a_k a_k^\dagger \right) \right.$$

$$+ (J_1 \Gamma_3 + m_k DG_2) \left(b_k^\dagger b_k + b_k b_k^\dagger \right)$$

$$+ \gamma_k J_1 \Gamma_1 \left(a_k b_{-k} + b_{-k} a_k + a_k^\dagger b_{-k}^\dagger + b_{-k}^\dagger a_k^\dagger \right)$$

$$\left. + i \left(\gamma_k J_1 G_2 + m_k D\Gamma_4 \right) \left(a_k b_{-k} + b_{-k} a_k - a_k^\dagger b_{-k}^\dagger - b_{-k}^\dagger a_k^\dagger \right) \right] \tag{A.16}$$

$$H_2 = J_2 \sum_k \left\{ \Gamma_5 \left[(\alpha + 1) - 2\lambda \eta_k \right] + 2\eta_k \left(1 - \lambda^2 \right) (\Gamma_3 + \Gamma_4 - \Gamma_1) \right\} \times$$

$$\times \left(a_k^\dagger a_k + a_k a_k^\dagger \right) \tag{A.17}$$

$$H_{SIA} = \frac{A}{2} \sum_k \left[\Gamma_6 \left(a_k^\dagger a_k + a_k a_k^\dagger \right) + \Gamma_7 \left(b_k^\dagger b_k + b_k b_k^\dagger \right) \right]. \tag{A.18}$$

The renormalized Hamiltonian matrix is

$$H_k = \begin{pmatrix} M_k & 0 \\ 0 & M^*_{-k} \end{pmatrix}, \quad M_k = \begin{pmatrix} r_1 & f^* \\ f & r_2 \end{pmatrix},$$

(A.19)

with temperature dependent parameters:

$$
\begin{aligned}
r_1^{(MSW)} &= 2\left(J_1\Gamma_2 + m_k D G_2\right) + J_2\left\{\Gamma_5\left[(\alpha+1) - 2\lambda\eta_k\right]\right. \\
&\quad \left. + 2\eta_k\left(1-\lambda^2\right)\left(\Gamma_3 + \Gamma_4 - \Gamma_1\right)\right\} + \frac{A}{2}\Gamma_6 \\
r_2^{(MSW)} &= 2\left(J_1\Gamma_3 + m_k D G_2\right) + \frac{A}{2}\Gamma_7 \\
h_x^{(MSW)} &= 2\gamma_k J_1 \Gamma_1 \\
h_y^{(MSW)} &= 2\left(\gamma_k J_1 G_2 + m_k D \Gamma_4\right)
\end{aligned}
$$

(A.20)

To obtain temperature dependent expressions for the mean-field parameters Γ_i (or equivalently, g_i), we Fourier transform the thermal averages $\langle a_i^\dagger a_j \rangle$, $\langle b_i^\dagger b_j \rangle$, $\langle a_i b_j \rangle$ and $\langle b_i a_j \rangle$, and make a change of basis using

$$\psi_k = T_k \varphi_k$$

(A.21)

with $\psi_k^\dagger = \begin{pmatrix} a_k^\dagger & b_{-k} & a_{-k} & b_k^\dagger \end{pmatrix}$ being the original basis, and $\varphi_k^\dagger = \begin{pmatrix} \alpha_k^\dagger & \beta_{-k} & \alpha_{-k} & \beta_k^\dagger \end{pmatrix}$ being a new basis. The matrix T_k is given by Eq. (4.22). As mentioned before, in a particle-hole Hamiltonian, the Hilbert space is duplicated, so we can find an irreducible 2×2 representation for the transformation above:

$$\begin{pmatrix} a_k \\ b_{-k}^\dagger \end{pmatrix} = \begin{pmatrix} u^* & -v \\ -v^* & u \end{pmatrix} \begin{pmatrix} \alpha_k \\ \beta_{-k}^\dagger \end{pmatrix}.$$

(A.22)

The thermal averages, after a change of basis, can be written in terms of the parameters u and v and the occupation number of the bands $n_k^{\alpha,\beta}$. For instance:

$$
\begin{aligned}
\langle a_i^\dagger a_i \rangle &= \frac{2}{N}\sum_k \langle a_k^\dagger a_k \rangle = \frac{2}{N}\sum_k \left[|u|^2 n_k^\alpha + |v|^2\left(1+n_k^\beta\right)\right] \\
\langle b_i^\dagger b_i \rangle &= \frac{2}{N}\sum_k \langle b_k^\dagger b_k \rangle = \frac{2}{N}\sum_k \left[|v|^2\left(1+n_k^\alpha\right) + |u|^2 n_k^\beta\right],
\end{aligned}
$$

(A.23)

where N is the total number of sites. Here,

$$n_k^\alpha = \left\langle \alpha_k^\dagger \alpha_k \right\rangle = \left[\exp\left(E_k^\beta / k_B T \right) - 1 \right]^{-1}$$
$$n_k^\beta = \left\langle \beta_k^\dagger \beta_k \right\rangle = \left[\exp\left(E_k^\alpha / k_B T \right) - 1 \right]^{-1} \tag{A.24}$$

are the Bose-Einstein distributions. The terms $\left\langle \alpha_k^\dagger \alpha_k \right\rangle$ and $\left\langle \beta_k^\dagger \beta_k \right\rangle$ are the only thermal averages in the new basis that are not zero. To illustrate that, let's consider a term of the form

$$\left\langle \alpha_k \beta_{-k} \right\rangle = \frac{1}{Z} \sum_n e^{-\beta E_k^n} \left\langle n \right| \alpha_k \beta_{-k} \left| n \right\rangle . \tag{A.25}$$

The matrix element $\left\langle n \right| \alpha_k \beta_{-k} \left| n \right\rangle$ is an overlap of the state $\beta_{-k} \left| n \right\rangle$ and $\alpha_k^\dagger \left| n \right\rangle$. Both states are eigenstates of H_k, but as they do not have identical sets of occupation numbers of α and β bosons, their overlap is zero. Hence $\left\langle \alpha_k \beta_{-k} \right\rangle$ and its complex conjugate are zero. This occurs for every other thermal average, except $\left\langle \alpha_k^\dagger \alpha_k \right\rangle$ and $\left\langle \beta_k^\dagger \beta_k \right\rangle$.

Performing the procedure detailed above, we obtain temperature dependent expressions for the g_i and G_i parameters:

$$g_1 = \frac{2}{N} \sum_k \left[|u|^2 \, n_k^\alpha + |v|^2 \left(1 + n_k^\beta \right) \right]$$

$$g_2 = \frac{2}{N} \sum_k \left[|u|^2 \, n_k^\beta + |v|^2 \left(1 + n_k^\alpha \right) \right]$$

$$g_5 = \frac{2}{N} \sum_k \eta_k \left[|u|^2 \, n_k^\alpha + |v|^2 \left(1 + n_k^\beta \right) \right]$$

$$g_6 = \frac{2}{N} \sum_k \eta_k \left[|u|^2 \left(1 + n_k^\alpha \right) + |v|^2 \, n_k^\beta \right]$$

$$G_1 = -\frac{2}{N} \sum_k \gamma_k \, xv \left(1 + n_k^\alpha + n_k^\beta \right)$$

$$G_2 = \frac{2}{N} \sum_k \gamma_k \, yv \left(1 + n_k^\alpha + n_k^\beta \right), \tag{A.26}$$

where we defined $u \equiv x + iy$. The sublattice (staggered) magnetization is given by

$$m = S - \left\langle a_i^\dagger a_i \right\rangle = S - \frac{2}{N} \sum_k \left[|u|^2 \, n_k^\alpha + |v|^2 \left(1 + n_k^\beta \right) \right]. \tag{A.27}$$

The temperature dependence comes from the Bose-Einstein factors. In the continuum limit, the summation becomes an integral over the Brillouin zone:

$$\frac{2}{N} \sum_\mathbf{k} [\clubsuit] \rightarrow \int_{BZ} \frac{d^2 k}{(2\pi)^2} \, [\clubsuit] . \tag{A.28}$$

For each temperature, we can obtain the Γ_i factors self-consistently from the Eqs. (A.26) and Eqs. (A.15). These terms renormalize the Hamiltonian.

In summary, the effective Hamiltonian becomes temperature dependent when we include quartic terms through a mean-field decoupling. For each temperature, coefficients Γ_i that renormalize the Hamiltonian parameters can be obtained self-consistently through (A.15) and (A.26). All the equations in Chapter 4 remain the same, but with the renormalized parameters r_1, r_2 and f, following Eqs. (A.20).

APPENDIX B – Berry curvature of a bosonic Bogoliubov-de Gennes Hamiltonian

In this appendix we derive an expression for a bosonic Bogoliubov-de Gennes Hamiltonian, which can be applied to any two-band AFM or FiM magnonic system. The Berry curvature is obtained from another quantity, the *Berry connection* A_j^n, as [16]:

$$\Omega_{xy}^n(\mathbf{k}) \equiv \frac{\partial A_y^n}{\partial k_x} - \frac{\partial A_x^n}{\partial k_y}, \tag{B.1}$$

where n labels the bands. The j-th component of Berry connection of a bosonic BdG Hamiltonian is given by [153]

$$A_j^n \equiv i \left[\eta T_k^\dagger \eta \frac{\partial T_k}{\partial k_j} \right]_{nn}, \tag{B.2}$$

where η is the "metric" matrix and T_k is the transformation matrix defined in Eq. 4.22. Note that the Hilbert space is doubled, so $n = 1, 2, 3, 4$, Using Eq. B.2 in Eq. B.1, we get:

$$\Omega_{xy}^n (\mathbf{k}) = i \sum_{\mu\nu} \varepsilon_{\mu\nu} \left[\eta \frac{\partial T_k^\dagger}{\partial k_\mu} \eta \frac{\partial T_k}{\partial k_\nu} \right]_{nn}. \tag{B.3}$$

The matrices η and T_k are block diagonal:

$$\eta = \begin{pmatrix} 1 & 0 & 0 & 0 \\ 0 & -1 & 0 & 0 \\ 0 & 0 & -1 & 0 \\ 0 & 0 & 0 & 1 \end{pmatrix} = \begin{pmatrix} \sigma_z & 0 \\ 0 & -\sigma_z \end{pmatrix} \tag{B.4}$$

$$T_k = \begin{pmatrix} u_k^* & -v_k & 0 & 0 \\ -v_k^* & u_k & 0 & 0 \\ 0 & 0 & u_{-k} & -v_{-k}^* \\ 0 & 0 & -v_{-k} & u_{-k}^* \end{pmatrix} = \begin{pmatrix} T_\alpha & 0 \\ 0 & T_\beta \end{pmatrix}, \tag{B.5}$$

so we can perform a block multiplication:

$$\eta \frac{\partial T_k^\dagger}{\partial k_\mu} \eta \frac{\partial T_k}{\partial k_\nu} = \begin{pmatrix} \sigma_z \frac{\partial T_\alpha^\dagger}{\partial k_\mu} \sigma_z \frac{\partial T_\alpha}{\partial k_\nu} & 0 \\ 0 & \sigma_z \frac{\partial T_\beta^\dagger}{\partial k_\mu} \sigma_z \frac{\partial T_\beta}{\partial k_\nu} \end{pmatrix}. \tag{B.6}$$

The expression for the Berry curvature can be reduced to a 2×2 representation

$$\Omega_{xy}^n(\mathbf{k}) = i \sum_{\mu\nu} \varepsilon_{\mu\nu} \left(\sigma_z \frac{\partial T_{\alpha,\beta}^\dagger}{\partial k_\mu} \sigma_z \frac{\partial T_{\alpha,\beta}}{\partial k_\nu} \right)_{nn}, \tag{B.7}$$

where we can choose the α or β sector. We focus on the particle states, remembering that for the α-sector, it corresponds to the first column of T_α ($n = 1$), and for the β-sector, to the second column of T_β ($n = 2$).

Focusing on the α-sector first, we have:

$$\Omega_{xy}^\alpha(\mathbf{k}) = i \sum_{\mu\nu} \varepsilon_{\mu\nu} \left(\sigma_z \frac{\partial T_\alpha^\dagger}{\partial k_\mu} \sigma_z \frac{\partial T_\alpha}{\partial k_\nu} \right)_{11}. \tag{B.8}$$

Using $T_\alpha = \begin{pmatrix} u_k^* & -v_k \\ -v_k^* & u_k \end{pmatrix}$ (see Section 4), we have (suppressing the index k for a clearer notation):

$$\sigma_z \frac{\partial T_\alpha^\dagger}{\partial k_x} \sigma_z \frac{\partial T_\alpha}{\partial k_y} = \begin{pmatrix} \frac{\partial u}{\partial k_x} & -\frac{\partial v}{\partial k_x} \\ \frac{\partial v^*}{\partial k_x} & -\frac{\partial u^*}{\partial k_x} \end{pmatrix} \begin{pmatrix} \frac{\partial u^*}{\partial k_y} & -\frac{\partial v}{\partial k_y} \\ \frac{\partial v^*}{\partial k_y} & -\frac{\partial u}{\partial k_y} \end{pmatrix}$$

$$\Rightarrow \left[\sigma_z \frac{\partial T_\alpha^\dagger}{\partial k_x} \sigma_z \frac{\partial T_\alpha}{\partial k_y} \right]_{11} = \frac{\partial u}{\partial k_x} \frac{\partial u^*}{\partial k_y} - \frac{\partial v}{\partial k_x} \frac{\partial v^*}{\partial k_y}, \tag{B.9}$$

and we can write

$$\sum_{\mu\nu} \varepsilon_{\mu\nu} \left(\sigma_z \frac{\partial T_\alpha^\dagger}{\partial k_\mu} \sigma_z \frac{\partial T_\alpha}{\partial k_\nu} \right)_{11} = \left(\frac{\partial u}{\partial k_x} \frac{\partial u^*}{\partial k_y} - \frac{\partial v}{\partial k_x} \frac{\partial v^*}{\partial k_y} \right) - \left(\frac{\partial u}{\partial k_y} \frac{\partial u^*}{\partial k_x} - \frac{\partial v}{\partial k_y} \frac{\partial v^*}{\partial k_x} \right)$$

$$= \left(\frac{\partial u}{\partial k_x} \frac{\partial u^*}{\partial k_y} - \frac{\partial v}{\partial k_x} \frac{\partial v^*}{\partial k_y} \right) - C.C.. \tag{B.10}$$

The expression for the Berry curvature of the state α state reduces to

$$\Omega_{xy}^\alpha(\mathbf{k}) = i \left[\left(\frac{\partial u}{\partial k_x} \frac{\partial u^*}{\partial k_y} - \frac{\partial v}{\partial k_x} \frac{\partial v^*}{\partial k_y} \right) - C.C. \right]$$

$$= -2 \operatorname{Im} \left(\frac{\partial u}{\partial k_x} \frac{\partial u^*}{\partial k_y} - \frac{\partial v}{\partial k_x} \frac{\partial v^*}{\partial k_y} \right). \tag{B.11}$$

Here it is convenient to define parameters θ_k and ϕ_k as:

$$tan\,\phi_k = \frac{h_y}{h_x} \qquad\qquad cosh\,\theta_k = \frac{r}{w}. \tag{B.12}$$

With that it is possible to show that $u = e^{i\phi} \cosh\left(\frac{\theta}{2}\right)$ and $v = \left(\frac{r-w}{2w}\right)^{1/2}$. The derivatives in Eq. B.11 become (Im $\frac{\partial v}{\partial k_x} \frac{\partial v^*}{\partial k_y} = 0$ because v is real):

$$
\begin{aligned}
\frac{\partial u}{\partial k_x} &= e^{i\phi}\left[i\cosh\frac{\theta}{2}\left(\frac{\partial\phi}{\partial k_x}\right) + \frac{1}{2}\sinh\frac{\theta}{2}\left(\frac{\partial\theta}{\partial k_x}\right)\right] \\
\frac{\partial u^*}{\partial k_y} &= e^{-i\phi}\left[-i\cosh\frac{\theta}{2}\left(\frac{\partial\phi}{\partial k_y}\right) + \frac{1}{2}\sinh\frac{\theta}{2}\left(\frac{\partial\theta}{\partial k_y}\right)\right],
\end{aligned}
\tag{B.13}
$$

and using $\sinh\left(\frac{\theta}{2}\right)\cosh\left(\frac{\theta}{2}\right) = \frac{1}{2}\sinh\theta$ we finally get

$$
\Omega^\alpha_{xy}(\mathbf{k}) = -\frac{1}{2}\sinh\theta_k\left(\frac{\partial\phi_k}{\partial k_x}\frac{\partial\theta_k}{\partial k_y} - \frac{\partial\phi_k}{\partial k_y}\frac{\partial\theta_k}{\partial k_x}\right).
\tag{B.14}
$$

For the β-sector, the initial expression is

$$
\Omega^\beta_{xy}(\mathbf{k}) = i\sum_{\mu\nu}\varepsilon_{\mu\nu}\left(\sigma_z\frac{\partial T^\dagger_\beta}{\partial k_\mu}\sigma_z\frac{\partial T_\beta}{\partial k_\nu}\right)_{22}.
\tag{B.15}
$$

Noting that $T_\beta(\mathbf{k}) = T^*_\alpha(-\mathbf{k})$, it is easy to show that

$$
\Omega^\beta_{xy}(\mathbf{k}) = -\frac{1}{2}\sinh\theta_{-k}\left(\frac{\partial\phi_{-k}}{\partial k_x}\frac{\partial\theta_{-k}}{\partial k_y} - \frac{\partial\phi_{-k}}{\partial k_y}\frac{\partial\theta_{-k}}{\partial k_x}\right).
\tag{B.16}
$$

The general relation between the Berry curvatures of the two bands is $\Omega^\beta_{xy}(\mathbf{k}) = \Omega^\alpha_{xy}(-\mathbf{k})$. When these are even functions ($\Omega^\alpha_{xy}(\mathbf{k}) = \Omega^\alpha_{xy}(-\mathbf{k})$), both Berry curvatures have the same sign: $\Omega^\beta_{xy}(\mathbf{k}) = \Omega^\alpha_{xy}(\mathbf{k})$. But when they are odd functions ($\Omega^\alpha_{xy}(\mathbf{k}) = -\Omega^\alpha_{xy}(-\mathbf{k})$) the Berry curvatures have opposite signs: $\Omega^\beta_{xy}(\mathbf{k}) = -\Omega^\alpha_{xy}(\mathbf{k})$.

It is possible to show that the hole states, which correspond to the second and third columns of T_k, have opposite Berry curvature in the same band index as a consequence of particle-hole symmetry [16]:

$$
\Omega^{n(hole)}_{xy}(\mathbf{k}) = -\Omega^{n(particle)}_{xy}(\mathbf{k})
\tag{B.17}
$$

Evaluating Eq. B.14 with the definitions of θ_k and ϕ_k, it is possible to show that:

$$
\begin{aligned}
\Omega^\alpha_{xy}(\mathbf{k}) = -\frac{1}{2}\frac{1}{w^3|f|}&\left\{\left(h_x\frac{\partial h_y}{\partial k_x} - h_y\frac{\partial h_x}{\partial k_x}\right)\left[\frac{r}{|f|}\left(h_x\frac{\partial h_x}{\partial k_y} + h_y\frac{\partial h_y}{\partial k_y}\right) - |f|\frac{\partial r}{\partial k_y}\right]\right. \\
&\left. - \left(h_x\frac{\partial h_y}{\partial k_y} - h_y\frac{\partial h_x}{\partial k_y}\right)\left[\frac{r}{|f|}\left(h_x\frac{\partial h_x}{\partial k_x} + h_y\frac{\partial h_y}{\partial k_x}\right) - |f|\frac{\partial r}{\partial k_x}\right]\right\}
\end{aligned}
\tag{B.18}
$$

and from this we can plot the Berry curvature of any system, knowing the Hamiltonian parameters h_x, h_y and r. We stress that the imaginary part of the Hamiltonian comes from h_y. From the expression above, we see it is crucial that $h_y \neq 0$ for a non-null Berry curvature. In other words: an imaginary term in the Hamiltonian is necessary for the system to have a non-null Berry curvature.